POLITECNICO DI MILANO

Scuola di Ingegneria Industriale e dell’Informazione

Corso di Laurea Magistrale in Ingegneria Meccanica

SQUEEZE FILM DAMPER MODELING AND APPLICATION

Supervisor:	Prof. Paolo PENNACCHI
Co-supervisor:	Prof. Steven CHATTERTON

Edoardo GHELLER

Matr. 918567

Anno Accademico 2019 – 2020

ACKNOWLEDGEMENTS

Per prima cosa vorrei ringraziare il Prof. Chatterton e il Prof. Pennacchi per avermi ispirato e guidato nel corso dell'ultimo anno per la realizzazione di questa tesi. Spero vivamente di poter continuare a collaborare e crescere con loro. Un pensiero va in generale a tutti i professori che ho avuto la fortuna di incontrare nei cinque anni trascorsi al Politecnico, anni impegnativi e difficili ma indimenticabili.

Nell'ultimo anno non posso che ringraziare tutti gli amici che mi sono stati vicini e con cui mi sono spesso confrontato. A partire dal gruppo di Caselle e quindi Vincent, Giulio e Mariangela, Foz, Toffa, Manuel, Albe e la Silvia e Taffa. Le radici sono importanti e con degli amici come loro lo sono ancora di più.

Un grazie di cuore va agli amici del Nievo, un gruppo sgangherato ma che, nonostante le diverse direzioni che le nostre vite hanno preso, rimane unito e si rafforza anno in anno, grigliata dopo grigliata. Ceck, Leo, Silvi, Toni e Rove, Vale: vi voglio bene.

Grazie al Poli che mi ha fatto conoscere delle persone stupende e ha fatto nascere amicizie solide che resistono anche fuori dalle aule universitarie. Adriana e Claudio, conosciuti tra i banchi il primo giorno di lezione ai quali, anche se sono diventati un'energetica e un semi-gestionale, voglio ancora bene. Un pensiero a Franci, Laura e Pippo, i tre amici designers che non mi hanno mai discriminato in quanto ingegnere.

Tra le persone conosciute a lezione ce n'è una molto speciale, quella persona che non tutti hanno la fortuna di conoscere durante la loro vita. Grazie Sofia per esserci e fare di me una persona migliore giorno dopo giorno.

Un pensiero affettuoso lo rivolgo a Cappe, primo compagno di banco al liceo che è diventato poi un amico insostituibile.

Infine, un grazie di cuore va alla mia famiglia, in primis mia mamma Daniela, mio papà Mirco e mia sorella Carolina che hanno sempre creduto in me e mi sostengono giorno dopo giorno. È merito loro se oggi sono la persona che sono. Un pensiero va anche a mio zio Massimo e alla zia Stefania. Non posso dimenticare i nonni acquisiti: lo zio Danilo e la zia Maria, e gli zii e cugine acquisiti: Chiara, Massimo, Matilde e Camilla.

Vorrei dedicare la tesi ad Aldo, Maria, Pietro e Rosina: i nonni che non ci sono più e a tutti i bei ricordi che ho della mia infanzia trascorsa con loro; a nonna Teresa, la persona più buona che io conosca. Da ognuno di loro ho imparato qualcosa e avranno sempre un posto speciale nel mio cuore.

TABLE OF CONTENTS

INDEX OF FIGURES

INDEX OF TABLES

ACRONYMS

BC	Boundary Condition
CC	Counter Clockwise
C	Clockwise
CCO	Circular Centered Orbits
CFD	Computational Fluid Dynamics
CV	Control Volume
LCP	Linear Complementarity Problem
SFD	Squeeze Film Damper
O-R	O-Ring
P-R	Piston Ring
RP	Rayleigh-Plesset

INTRODUCTION

In rotordynamics, the most critical issue to deal with are the level of vibrations and instability. To deal with these matters, squeeze film damper (SFD) are widely used in the industry. These components can help to reduce the vibrations resonance peaks, to reduce the level of vibration at the operating frequency of the machine and also to correct conditions of instability.

In the following pages, a detailed report of the state of the art available on these components is presented. Starting from the first analytical model developed in the previous century up to the most recent models based on the finite volume discretization, the different numerical approaches used to describe the dynamic behavior of SFDs are reported. The phenomena that characterize the behavior of these damping elements are introduced, thanks to the many experimental campaigns carried on in the past decades. Among these there are the geometry, the feeding and the sealing system, the effect of air ingestion and cavitation.

After the state of the art examination, a model based on the Reynolds equation is developed and validated. The goal of this work is to develop a simple and reliable model, that can be used for a first stage analysis, to understand the general behavior of the dampers. The different critical characteristic elements of the SFD are dealt with. The effect of temporal inertia is added to the equation, the possibility to simulate the behavior of the feeding and sealing system is presented, the presence of air ingestion and cavitation is considered.

The model is then applied to different geometrical configurations and their effect on the force coefficient is evaluated. In particular the focus is concentrated on the effect of the damper’s clearance, the damper’s length, the presence of a central groove and the presence of feeding and sealing system. Then also different operating conditions are investigated like the presence of static eccentricity and the effect of air ingestion.

Finally, the behavior of a centrifugal compressor equipped with a SFD is simulated. Thanks to the finite element model of the machine, the damper’s effect on the reduction of the vibration level and its ability to reduce the machine’s instability is investigated. Different geometries are studied in order to see the effect of different force coefficients obtained with dampers with smaller clearance and dampers equipped with a sealing device. In this section it is also possible to appreciate the difficulty to choose the correct damper for the machine and that it is not guaranteed that if a configuration is useless for one purpose it will be the same for the other. In fact, in order to obtain the best effect from the SFD, this component should be customized for every machine.

1. STATE OF THE ART

Vibrations are an intrinsic problem in all the fields of mechanical engineering and rotordynamics is one of them. Rotating machines are subjected to remarkable loads and, with the development of machines that operate above some critical speeds, the control of vibrations is fundamental to guarantee long time operation. The typical problems in this field are excessive steady state synchronous vibration levels and subsynchronous rotor instabilities. The first one usually arises from excessive unbalance or due to operation close to a critical speed. The second one may depend on the presence of instability sources, connected to cross-coupling effects present in bearing systems and seals, among the others. In some cases, the increase of the vibration, when crossing a critical speed during a runup or a rundown, can be harmful for the operation of the machine and the addition of some damping to the system is required.

To this aim, *squeeze film dampers* (SFDs) are, up to now, one of the most effective components used because they offer the advantage of dissipation of vibration energy and the isolation between the rotating machine and the supporting structure, which, on the contrary, is very limited for both rolling element bearing and oil film bearings. In addition to this, SFDs can improve of the dynamic stability characteristics of rotor-bearing systems.

SFDs development and implementation started in the 60s of the previous century and the first patent publication, describing the operation of a squeeze film damper, was filed in London in 1966 by Rolls Royce [1]. SFD's field of application, that spaces from complex aeronautical engines to compact turbochargers used in the automotive field, shows the incredible flexibility of this component that is present in many different forms. Research on this field continues also nowadays [2], this demonstrates how much these components are interesting for the industry and how complex is the physics governing the process.

The most common design for these components is the one coupled with rolling element bearings shown in Fig. 1-1.

The shaft vibration is transferred to the external ring of the bearing that *"squeezes"* the oil film, placed between the two surfaces (A and B of Fig. 1-1), generating high dynamic pressures. The final result is the formation of dynamic forces that act against the lateral displacement of the rotor of the shaft. The anti-rotation mechanism is applied to avoid any spinning motion of the bearing, so that only translational displacements are possible, i.e. the shaft can only translate or orbit without rotating about its axis of symmetry. This configuration is characterized by strong non-linearities due to the "bottoming out": the shaft remains in contact with the hub of the damper at the beginning of the operation; when the level of vibration is increased, the detachment of the two components happens resulting in a discontinuous change of the properties of the system.

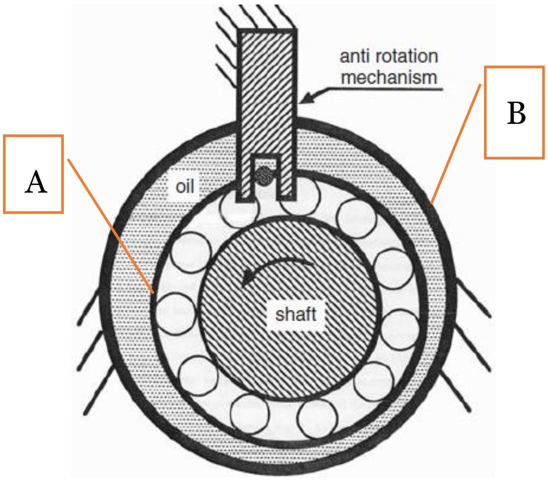

Fig. 1-1 Simple squeeze film damper without centering mechanism, from [3]

To reduce the non-linearity and the risk of collision between the static element B and the whirling one A in case of large shaft displacements, different supports are used, such as O-rings and squirrel cages. The selection of the proper stiffness of the support is fundamental for the correct operation of the SFD: if the support is too stiff, no relative motion between the shaft and the cage will be possible i.e. no squeezing of the oil film; if the stiffness is too low, the damper can behave like a non-supported one [1], [3].

A further design of SFDs, shown in Fig. 1-2, is the so-called integral squeeze film damper [4]: the damper is placed in parallel to an oil-film journal bearing. Grooves are machined, thanks to wire EDM (Electrical discharge machining) technology, below the journal pads. The motion around the pivot during the operation, squeezes the oil in and out the groove, increasing the damping capacity of the oil-film bearing. [1] [3].

Damping is the design parameter for all SFDs and optimal value for the given application must be obtained. As a matter of fact, the utilization of a device, whose damping capability is not aligned with the one requested by the system, is useless if not dangerous. If the level of damping is too high, the damper will dynamically behave as a rigid connection, if the level of damping is too small, nothing will change in the dynamic response of the machine.

There are many studies in the literature that provide guidelines to determine the correct damping needed by a machine; in general, it depends on the dynamic characteristics of the machine itself, the typical operating conditions and the kind of excitations: [5], [6].

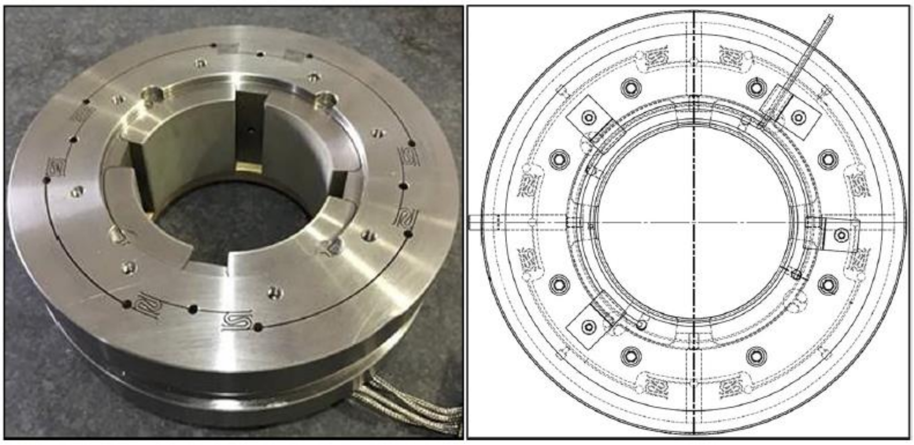

Fig. 1-2 Integral squeeze film damper in parallel to a journal bearing, from [4]

The first model used to evaluate the force exerted by SFDs was developed using the 1D Reynolds equations for short, plain journal bearings (1). This approximation, *Short bearing Approximation*, is considered valid for dampers with $\frac{L}{D} < 0.25$ and without seals, [7]. The force is then modelled by means of linearized stiffness and damping coefficients, likewise oil-film bearings. The hypotheses behind this equation are the usual ones, i.e. negligible fluid inertia and volume forces, constant fluid viscosity and negligible flow of the lubricant in radial direction.

$$\frac{\partial}{\partial z}\left(\frac{h^3}{6\mu}\frac{\partial P}{\partial z}\right) = \left(\omega_b + \omega_j\right)\frac{\partial h}{\partial \theta} + 2\frac{\partial h}{\partial t} \qquad (1)$$

Once equation (1) is integrated, the pressure distribution in the oil-film is obtained and, with a further spatial integration, the resulting forces are calculated. The motion of the shaft is modelled, for convenience, as i) circular synchronous precessions, centered or with a static eccentricity, or ii) small amplitude motions about a static displaced center, see Fig. 1-3. The first model is usually applied when the response to unbalance is investigated, the second one is used for critical speed and stability analyses, [8].

Also the *Long Bearing Approximation* can be done, it is valid for $\frac{L}{D} \rightarrow \infty$ or in general when seals limiting the oil leakage are applied at the end of the damper. The resulting pressure distribution is constant along the axial dimension, [7]. For finite length bearings the results obtained with the two different approximations are blended so to obtain an intermediate result.

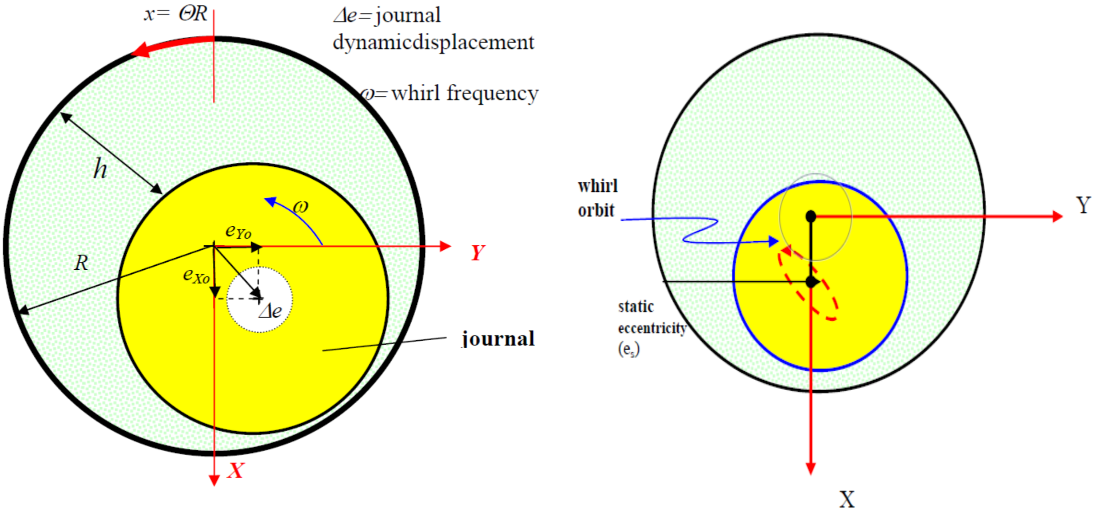

Fig. 1-3 Typical SFD motion representation: circular centered orbits (CCO) on the left, small amplitude motion around static off-centered position, taken from [7].

If the motion of the shaft is considered with respect to the fixed walls, it is easy to understand that, when the clearance between the components is reduced in time, i.e. *positive squeeze*, the oil film is pressurized. On the contrary, where the height of the film is increased, i.e. *negative squeeze*, the pressure of the oil film is reduced. Since fluids are not able to sustain tensile stresses, the film is ruptured. When analyzing the complete pressure profile it is easy to notice the presence of a zone where the pressure P is lower than the ambient value. Different cavitation models and algorithms to deal with the issue have been developed. The first cavitation model that was introduced is the so called π-film model, also known as Gumbel condition, in the region where the pressure is below the ambient value it is considered null. According to this hypothesis, the ruptured film extends over half the angular length of the bearing. One of the most used algorithm is the so-called *Elrod's cavitation algorithm*, see [9]. The pressure is iteratively calculated and, when it is negative, a switch function is activated and the Poiseuille flow is suppressed in that region. An evolution of this approach consists in the adoption of the *Linear Complementarity Problem* (LCP). The Reynolds equation is rewritten replacing the pressure and density with two new variables that are complementary in the whole domain, the product between the two is always zero. In [10], a method was developed for incompressible fluids where the two variables are the pressure and the ratio between the actual density of the fluid and the density of the oil. In [11], an advanced model is proposed by the same authors where the fluid compressibility is taken in consideration, different functions that link the fluid pressure with the density are proposed. The authors also introduce the effect of piezo-viscosity and shear thinning on the viscosity of the fluid. Even if with different starting hypothesis and formulations, Almqvist et al., proposed in [12] a model which is identical to the one derived in [10]. These different cavitation algorithms will be described more in detail in the following pages and one will be adopted in the calculations.

In [5], the authors obtained the force coefficients in Table 1-1 where: cl is the radial clearance, ε is the eccentricity ratio, ω is the whirling frequency and L, R are the dimensions of the damper.

CIRCULAR SYNCHRONOUS PRECESSION		
UNCAVITATED	$K_o = 0$	$C_o = \dfrac{\mu R L^3 \pi}{2cl^3(1-\varepsilon^2)^{3/2}}$
CAVITATED	$K_o = \dfrac{2\mu R L^3 \varepsilon \omega}{cl^3(1-\varepsilon^2)^2}$	$C_o = \dfrac{\mu R L^3 \pi}{cl^3(1-\varepsilon^2)^{3/2}}$
PURE RADIAL SQUEEZE MOTION		
UNCAVITATED	$K_o = 0$	$C_o = \dfrac{\mu R L^3(\pi - \cos^{-1}\varepsilon)(2\varepsilon^2+1)}{cl^3(1-\varepsilon^2)^{5/2}}$
CAVITATED	$K_o = 0$	$C_o = \dfrac{\mu R L^3(2\varepsilon^2+1)}{cl^3(1-\varepsilon^2)^{5/2}}$

Table 1-1 Force coefficients for short SFD

On the contrary, Zeidan et al. in [1] considered the linearized forces resulting on infinitesimal motions about the static equilibrium position and observed that SFDs are not able to provide stiffness to the system: if the journal is not spinning the oil is not subjected to the shear effect, which is on the contrary typical of oil-film bearings, responsible for the generation of a stiffness term, owing to the hydrodynamic effect. Therefore, only inertia and damping forces are considered. For small amplitude displacements about an off-centered position, the forces were considered on a fixed reference system:

$$-\begin{bmatrix} F_x \\ F_y \end{bmatrix} = \begin{bmatrix} C_{xx} & C_{xy} \\ C_{yx} & C_{yy} \end{bmatrix} \begin{bmatrix} \dot{x} \\ \dot{y} \end{bmatrix} + \begin{bmatrix} M_{xx} & M_{xy} \\ M_{yx} & M_{yy} \end{bmatrix} \begin{bmatrix} \ddot{x} \\ \ddot{y} \end{bmatrix} \tag{2}$$

For centered circular orbits, a reference system rigidly connected with the whirling shaft, rotating in the fixed reference system, was considered and the relative forces are:

$$-\begin{bmatrix} F_r \\ F_t \end{bmatrix} = \begin{bmatrix} 0 & C_{rt} \\ 0 & C_{tt} \end{bmatrix} \begin{bmatrix} V_r \\ V_t \end{bmatrix} + \begin{bmatrix} M_{rr} & 0 \\ M_{tr} & 0 \end{bmatrix} \begin{bmatrix} a_r \\ a_t \end{bmatrix} \tag{3}$$

Since the whirling frequency is assumed to be constant, then $a_t = 0$, $V_t = \omega e$ and $a_r = -\omega^2 e$ (e is the orbit radius). All the force coefficients are then reported in the fixed reference system, for both cavitated and not cavitated film. What is interesting is that, in case of full film, i.e. no cavitation, the cross-coupling terms for the circular orbit are null.

According to both [1] and [5], the force coefficients are highly nonlinear and they depend mainly on the geometry of the bearing (length, radius and radial clearance), the kinematics of the journal (whirling frequency, static eccentricity and amplitude of motion) and the oil characteristics (viscosity and density).

The use of the basic 1D Reynolds equation, to build up a model to design SFDs, has the advantage of simplicity but, unfortunately, the predictions are reliable only for very simple geometries and for a limited range of operating conditions. The main reason is due to the fact that many simplistic hypotheses stand behind the formulation of the 1D Reynolds equation.

Many experimental test campaigns were made in the past to assess the quality of the predictions obtained starting from the Reynolds equation. One of the most complete was made by San Andres and his research group that recorded measurements over the last three decades [13]. Thanks to this paper, it is possible to understand the effect of different features of geometry and of operating conditions on the behavior of the SFD, showing that 1D Reynolds equation-based predictions are quite far from the reality. To perform this research, a special test-rig, made by a short shaft, moving inside a cylindrical cartridge has been developed, see Fig. 1-4. It consists in a rigid journal and a bearing cartridge, supported by steel rods, whose number can be changed, giving to the system an isotropic structural stiffness. An hydraulic static loader is used to statically displace the cartridge to an off-centered position. Two orthogonally placed electromagnetic shakers, placed on the two cartesian axes, with in the middle the hydraulic static loader, deliver periodic loads to the bearing cartridge with the possibility of changing the frequency of the excitation. The journal is hollow and some holes are machined to deliver the oil to the damper. The recorded measurements are: the dynamic pressure in different axial and circumferential positions, temperature of the oil film, forces acting on the shaft and its displacement. Different configurations, in terms of dimensions, feeding mechanism, sealing mechanism and kinematics were tested. The group investigated scrupulously the effects on the dynamic performance of different aspects such as: different types of cavitation, presence of inertia, different feeding mechanisms, open-ends vs sealed-ends configuration, different kinematics of the journal. Part of what reported in [13] was already mentioned in [1] and described in a synthetic form by San Andres in [8].

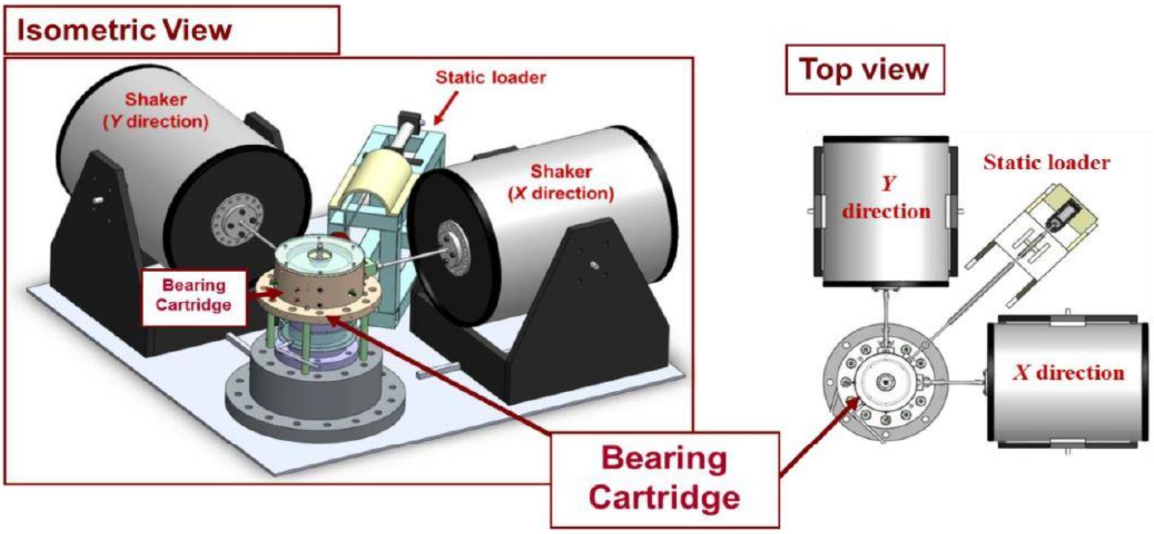

Fig. 1-4 Schematic of the test-rig used by San Andres and his research group, from [14]

The research group started by the investigation of the effect, on the dynamic behavior of the damper, of the basic geometrical quantities of the bearing, i.e. length and radial clearance. The results showed a trend quite predictable considering the results present in the literature, [1] and [5]. The damping is increased reducing the clearance and increasing the length of the damper.

Fluid inertia is neglected in the 1D Reynolds equation when thin oil film is considered. Usually the Reynolds number (Re) is lower than one in oil-film bearings but for SFDs this value depends largely on the single application. In general, for larger clearance and amplitudes of motion, the added mass produced by the oil dynamic pressurization found experimentally have a value comparable to the mass of the entire damper. It is reasonable to assume that $Re = 5 \div 50$ in a generic SFD. A deeper analysis is present in [15]. Due to the high velocities reached by rotating machines nowadays, the inertia - less hypothesis represents an idealized behavior far from the reality. In [16], the authors, assume that for moderate values of the Reynolds number ($Re \leq 10$) the fluid inertia does not affect the shape of purely viscous velocity profiles. This assumption allows to write the surface shear stress as function of mean flow components. Finally, the wall shear stress is explicitly written as function of the Reynolds number. The final value of the pressure is the sum of the inertia-less contribution, obtained solving the classical Reynolds equation, and an inertia contribution, considered as a first-order perturbation. Since the analysis is carried on a finite length bearing, the axial leakage is taken in consideration with a function that governs the variation of pressure in the axial direction. Even if the analysis is carried out for $Re \leq 10$, the authors extend its validity to higher values considering other experimental results. A similar approach is found in [17] where the author confront their results with the inertia-less Reynolds equation and a closed-form analytical model proposed by Vance. The difference between the three models increases as the Squeeze Reynolds number ($Re = \frac{\rho \omega c l^2}{\mu}$) increases. Hamzehlouia et al. in [18] compared the new model developed with the Reynolds equation and a model with only temporal inertia showing how the pressure profile changes with different Reynolds numbers. The presence of inertia determines an increase of the pressure peaks and a phase shift of the pressure circumferential evolution. It is interesting to notice that the difference between the two inertia models in the pressure profile is less evident in the radial force coefficient, direct expression of the inertial forces. This coefficient, negative and close to zero for the inertia-less case, is greater than zero and increases with the Reynolds number. Interestingly also the tangential force coefficient, direct expression of the damping force, is affected by the presence of inertia at higher Reynolds number. The same authors in [19] propose a different approach. The inertial effect is directly added to the Reynolds equation so that the pressure profile can be directly calculated without using the first-order perturbation technique. The general Reynolds equation is:

$$\begin{gathered}\frac{\partial}{R\,\partial\theta}\left(\frac{\rho h^3}{12\mu}\frac{\partial P}{R\partial\theta}\right)+\frac{\partial}{\partial z}\left(\frac{\rho h^3}{12\mu}\frac{\partial P}{\partial z}\right)\\ =\frac{\partial}{\partial t}(\rho h)+\frac{Reh^2}{12\omega cl^2}\frac{\partial^2\rho h}{\partial t^2}+\frac{\partial}{R\,\partial\theta}\left(\frac{Reh^2}{12\omega cl^2}\right)\frac{\partial}{\partial t}\left(\frac{\rho h^3}{12\mu}\frac{\partial P_0}{R\partial\theta}\right)\end{gathered} \tag{4}$$

The last two terms on the right represent the temporal inertia and the convective inertia. The last one contains the inertia-less pressure obtained with the Reynolds equation. If CCOs are considered, the pressure profile is not significantly affected by the fluid inertia, as stated in [17], so the previous equation can be rearranged as:

$$\begin{gathered}\left(1+\frac{\partial}{R\,\partial\theta}\left(\frac{Reh^2}{12\omega cl^2}\right)\right)\frac{\partial}{R\,\partial\theta}\left(\frac{\rho h^3}{12\mu}\frac{\partial P}{R\partial\theta}\right)+\frac{\partial}{\partial z}\left(\frac{\rho h^3}{12\mu}\frac{\partial P}{\partial z}\right)\\ =\frac{\partial}{\partial t}(\rho h)+\frac{Reh^2}{12\omega cl^2}\frac{\partial^2\rho h}{\partial t^2}\end{gathered} \tag{5}$$

In case of moderate and large Reynolds numbers the third order term in equation (4) can be neglected, as shown in [20], so the equation can be simplified. In [18], Hamzehlouia, shows that the difference between equation (5) and the reduced one, where the convective inertia terms are neglected, is relevant only for higher values of the Reynolds number and for an increase of the eccentricity ratio ε.

The feeding mechanisms used in SFDs are mainly central feeding grooves and feeding orifices. Feeding grooves were considered as a perfect separation between the two lands of the damper, where a constant pressure field was established. In the reality, inertial effects are magnified in the cavity and important levels of dynamic pressure are registered, see [13]. This feeding mechanism has the advantage of delivering a constant and homogeneous flow of lubricant to the lands. On the other hand, the big advantage of using feeding orifices is the possibility to build shorter bearings, remarkable for applications with tight space restrictions. Unluckily, they do not guarantee a homogeneous feeding and, the prediction of the flow close to them, is more complicated. Complex patterns of flow are established, and orifices usually act both as a sink or reservoir of lubricant. It is interesting to notice that that the operation of the damper is not strongly affected by the obstruction of one or more of the feeding orifices.

In [21], the authors propose to model the whole feeding system by applying the energy approach, commonly used in hydraulics. A constant leakage coefficient was considered to model the end seals of the tested damper. The feeding orifices are included in the cells of the grid used to discretize the geometry and the flow across the orifice is added to the equations used to discretize the problem. The author then modeled the whole feeding system, taking into consideration all the pressure losses on the grid and the mass continuity. Finally, the equation used for closure is the energy balance of the oil pump. The effect of the number of feeding orifices and the power given to the pump was investigated with some simulations. Far from resonance, the damper vibration amplitudes are amplified when a higher number of holes is used. On the other hand, increasing the number of holes, the orbits of vibration switch from elliptical to circular. It is interesting to notice that for an even number of orifices, the odd higher harmonics appear to be the most relevant in the damper response and vice versa. The increase of the number of feeding orifices also improves the rotor stability, the opposite happens for the force transmissibility which instead is higher. When the power supplied to the pump is increased, the hydrostatic effect is increased and so the force transmissibility at low frequencies. The author also reports the value of the pump exit pressure over time. Interestingly this value is far from being constant, as many authors instead considered in different models, and this fluctuation is amplified at the injection holes.

As it was mentioned before, typically SFDs are tested and modelled for circular orbits, centered or not, and small amplitudes movement about the static equilibrium position. It is easy to understand that these conditions are a simplification of the real orbital motion of the shaft which is usually elliptical. Thanks to the experimental results shown in [13] it is possible to state that both damping, and inertia coefficients are quite independent from the shape of the orbit. In particular, similar results are found for elliptical orbits and circular ones if the radius considered corresponds to the longest principal axis of the ellipse. In the study it was considered also the effect of the amplitude of whirl motion on the dynamic response. The results obtained shows that the force coefficients are more sensible to the static eccentricity rather than to the orbit dimensions. This conclusion only stands if cavitation is not present. In general, larger amplitude will increase the air entrainment and the oil depressurization, increasing the severity of the cavitation. If we concentrate on the definition of linearized force coefficients, i.e. change in bearing reaction forces due to infinitesimally small amplitude motions about the equilibrium position, it is possible to notice a disagreement in case of large amplitude motions. In [22], a novel method for the identification of the force coefficients is introduced. This new approach is more consistent when large amplitudes of motion are realized.

Open-ends SFDs are very common in the literature and many experimental campaigns are based on this configuration because it is easier to investigate different aspects separately. Usually for industrial application sealed-ends configuration are preferred because they present many advantages: lower quantity of lubricant can be used, seals represent an effective way to reduce air ingestion, the presence of the seals modifies the pressure profile inside the land resulting in higher damping, this gives the possibility to use shorter components. The most common sealing devices that are used are O-rings and piston rings. Unfortunately, some problematics arise when these devices are implemented: the behavior of polymeric material in time must be considered and the effect of dry friction must be added in the evaluation of the dynamic performances of the damper, [23]. The most critical aspect of sealed-ends SFDs is that perfect sealing cannot be achieved and, a certain level of leakage is needed, in order to take out the energy dissipated by the oil, preventing its excessive heating, that otherwise results in a decrease of the damping capability and establishment of harmful conditions for the polymeric components. For the reasons stated above, it is complicated to successfully predict the behavior of sealed-ends SFDs and it can be fully determined just including an experimentally evaluated leakage coefficient.

Cavitation is stated as one of the principal reasons why predictions on the force coefficients, made with the simple model used in [1] and [5], do not correlate well with the experimental results. For this reason, relevant effort has been put in the investigation and modeling of cavitation. In [24] the authors experimentally recognized five different cavitation regimes: un-cavitated film, cavitation bubble following the journal, oil-air mixture, vapor cavitation, vapor and gaseous cavitation. The second regime is considered as a transient condition, steady only for reduced whirling frequencies, that evolves in the third one with the shaft acceleration. The most common regimes are the third and fourth that sometimes combine with each other. Diaz and San Andres in [25] concentrated mostly on vapor cavitation and air entrainment, they tested a bearing in open-ends and in fully flooded configuration, changing whirling frequencies and pressure of supply oil, measuring the dynamic pressure generated. The difference of the pressure evolution in time for the two-cavitation mechanism is evident: for the vapor cavitation the pressure profile is nearly identical for every cycle, the bubbles form where the oil film thickness is bigger due to the depressurization of the oil film, in this position the pressure is constant and as soon as the pressure increases above the vapor saturation pressure, all the bubble collapse. For air entrainment, the pressure measurements showed great variability from one cycle to the other, with reduced values for both the maximum and minimum peak. It is interesting to notice the formation of a zone of constant pressure, with a value close to the ambient one, after the minimum peak that continues for half of the period. See Fig. 1-5.

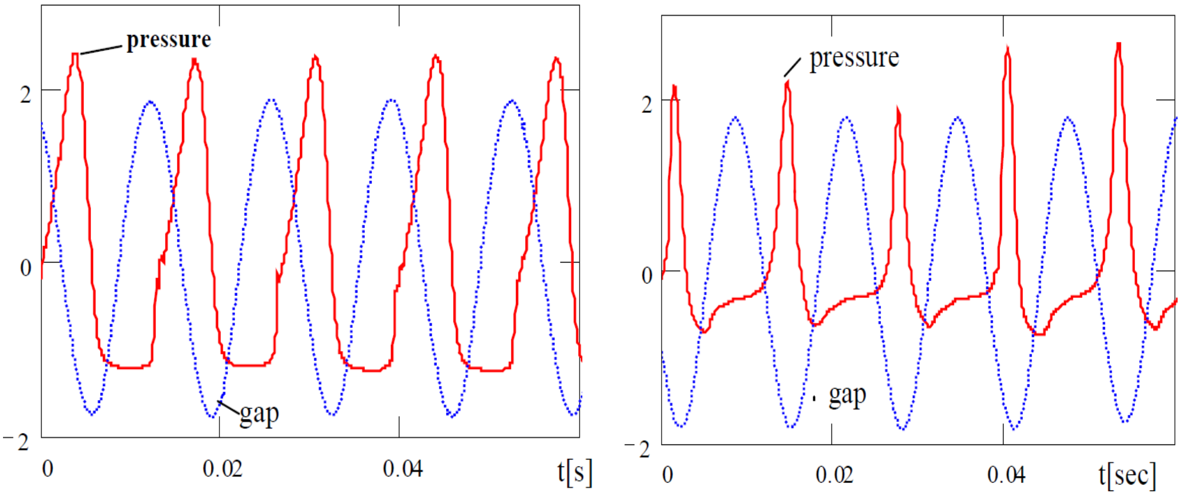

Fig. 1-5 Dynamic film pressure (bar) and local film gap (mm x 10) in a SFD operating with vapor cavitation on the left and air entrainment on the right, from [8]

From the data obtained by the experimental campaign and shown in [25], [26] and [27], air is "sucked" inside the bearing and, after some cycles, the bubbles of air are finely dispersed in the mixture and persist also in the high pressure zone. The presence of a compressible foamy mixture can explain the variability of the pressure's peak values. It was then found that the extension of the constant pressure zone increases with the whirling frequency and decreases when the supply pressure of the oil is higher. For the flooded configuration, relevant only for laboratorial applications, the excessive presence of oil is an obstacle for the air entrainment: only vapor cavitation is observed. Diaz shows a comparison between the peak-to-peak pressure for both configurations compared with an analytically derived value, valid for short length bearings and accounting for vapor cavitation. Is possible to see that the correlation, with the air entrainment case, is lost already at low whirling frequency while, for the flooded configuration, the trend followed by the experimental results follows the predicted one. Increasing the oil supply the experimental results tend to the analytical one, unfortunately, for high whirling frequencies, the oil supply pressure to avoid cavitation is too high. In [26], the experimental campaign was carried out feeding the damper with a mixture of oil and air in order to simulate the operation with air entrainment. The effect on the dynamic pressure of the volume fraction of air inside the mixture was shown: an increase of the air quantity determines a severe reduction of the dynamic performances of the damper. We must keep in mind that the forces acting on the shaft are generated by the dynamic pressure in the oil film: the effect of cavitation on the dynamic pressure is reflected on the damping and inertial forces. In [26] and [27] both radial and tangential forces were calculated through the integration of the dynamic pressure profile obtained experimentally. The radial force showed a limited variation with the increase of the whirling frequency and the feeding pressure, i.e. it is mostly independent on the air volume fraction of the mixture. For what regards the tangential force instead, it is possible to notice that, increasing the feeding pressure, the value of the force increases up to a steady value if the whirling frequency is low, on the contrary, no asymptotic value is reached i.e. the pressurization of the oil is not always able to avoid air entrainment. The air volume fraction has its highest effect on the tangential force. Flooded configurations are very effective against air entrainment, especially with increased oil supply pressure. Unfortunately, their realization for industrial application, especially for aeronautic applications, is impractical due to the large quantities of oil requested and the dimensions of the feeding pump. A practical way to reduce air ingestion is to apply sealing mechanisms at the extremities of the damper.

As it was shown above, the utilization of the 1D Reynolds equation, for the design of an SFD, can produce results largely different from the expected ones mainly due to all the effects not taken into consideration. This simplistic approach can be considered valid only for initial considerations or very simple configurations. For higher quality predictions, it is necessary to add some modifications to the system of equations considered. In the literature many improved models are present. Those take into consideration, among the others, the presence of the grooves and the cavitation effect.

In Delgado and San Andres [20], an improvement of [28], the flow inside the groove was divided in two regions: a through flow region and a recirculation flow region. The depth reached by the through flow is considered as the effective depth for both shallow and deep groves, this value should be calculated using a CFD simulation, but Delgado considered it as an effective groove depth, to be evaluated starting from the experimental results. The resulting Reynolds-like equation is:

$$\frac{\partial}{\partial \mathrm{x}}\left(h_\alpha^3 \frac{\partial P_\alpha}{\partial x}\right)+\frac{\partial}{\partial z_\alpha}\left(h_\alpha^3 \frac{\partial P_\alpha}{\partial z_\alpha}\right)=12\mu \frac{\partial}{\partial \mathrm{t}}(h_\alpha)+6\mu R\Omega \frac{\partial}{\partial \mathrm{x}}(h_\alpha)+(\rho h_\alpha^2)\frac{\partial^2}{\partial \mathrm{t}^2}(h_\alpha) \qquad (6)$$

Where α is the identification of the groove on the damper's axial evolution.

The pressure was considered as the sum of a zeroth order and a first order dynamic field. In the reference the boundary conditions are specified also for the integration of the "*Reynolds*" equation, valid for a single land and one grooved SFD with open-ends. A comparison with experimental results shows that the model is precise for the prediction of damping coefficients when the ratio of the effective depth over the film clearance is higher than 5. For the inertial coefficient, the most affected one by the presence of the groove, due to the high value of dynamic pressure generated [13], the correlation is good when the ratio of the effective depth over the film clearance is between 7 and 15.

The numerous experimental campaigns on the problem of cavitation pointed inadequacy of the cavitation models present in the literature (π-film model). To fully include the cavitation effect in the prediction of the dynamic performance of SFDs it is necessary to include the lubricant compressibility, determined by the presence of the bubbles in the oil. Diaz [29] exposes a detailed procedure, supported by a series of experimental results, to include the air ingestion effect in the 1D Reynolds equation, based on the hypothesis of an homogeneous bubbly mixture. The relative motion between the two phases of the mixture is neglected so the equations can be reduced to the case of single component and, since from experimental observation, the flow in the land can be considered isothermal, the energy transport equation is not included. β is defined as the gas volume fraction and is computed from the solution of the simplified Rayleigh-Plesset equation. With an analysis on the terms of the equation mentioned above, the author is able to simplify it in a quasi-static form so that:

$$\beta=\frac{1}{1+\frac{P(x,t)-P_v}{P_{G\sigma}}\left(\frac{1}{\beta_0}-1\right)} \qquad (7)$$

Where P_v is the vapor pressure, β_0 is the gas volume fraction in a reference position and $P_{G\sigma}$ is the pressure of the air bubble for the critical radius.

Using equation (7), the simplified Rayleigh-Plesset equation and the momentum transport equation, it is possible to fully determine the motion of the mixture. Considering the height of the lubricant film it is possible to adapt the equations to the geometry of the damper:

$$h=cl+e\cos\theta \qquad (8)$$

Where cl is the radial clearance and e is the amplitude of the oscillation. The fluid properties must be adapted to the case of a mixture:

$$\rho=(1-\beta)\rho_L \qquad (9)$$

$$\mu = (1-\beta)\mu_L \tag{10}$$

Where ρ_L and μ_L are density and viscosity of the pure lubricant. The equation for the viscosity is a reformulation of Dukler's relationship where the properties of air, which are some orders of magnitude smaller than the liquid ones, are neglected. At the end, the Reynolds-like equation for a short length SFD, performing circular centered orbits, with a quasi-static, isothermal, homogeneous bubbly mixture is:

$$-\omega\frac{\partial}{\partial\theta}\big(\rho(cl + e\,cos\,\theta)\big) - \frac{1}{L^2}\frac{\partial}{\partial\hat{z}}\left(\frac{\rho(c + e\,cos\,\theta)^3}{12\mu}\frac{\partial P}{\partial\hat{z}}\right) = 0 \tag{11}$$

Where $\hat{z} = \frac{z}{L}$.

To integrate the equation, the correct boundary conditions are needed. They usually are i) periodicity in the circumferential direction, ii) known pressure at an open end, iiia) zero flow for tightly sealed end or at a symmetry plane, iiib) relation between pressure and flow rate for partially sealed end.

The author also shows the comparison between experimental data, obtained with a controlled bubbly mixture feeding, and the model proposed. The correlation for the peak-to-peak pressure value seems valid for air volume fraction values lower than 0.5, for the tangential force the correlation remains good for values up to 0.6, for the radial force the trend obtained experimentally an the one calculated have the same shape but an offset is present, probably due to an hydrostatic component not considered in the model.

Diaz and San Andres report both in [29] and [30] a model to evaluate the air entrainment in open-ends SFDs. The most relevant factors that affect the amount of air ingested in the lands of the damper are: supply and discharge pressures, the lubricant axial flow rate, the whirl frequency, the journal vibration amplitude, and the particular geometry of the damper. The author proposed a simple analysis based on the balance of axial flows where, at the open end, the mass flow, if negative, is mass of air entering the damper, if positive, is the mass of mixture leaving the damper. Evaluating the control volume in a periodic steady state condition, the overall change of mass over a full period is zero. Considering the mass balance equation averaged other the period:

$$\rho_{oil}\overline{q_{oil}} + \rho_{air_0}\overline{q_{air}} - \widehat{\rho_{mix_0}}\overline{q_{mix}} = 0 \tag{12}$$

Where $\overline{q_i}$ are the period averaged volumetric flows, ρ_{air_0} is the density of air at ambient conditions and $\widehat{\rho_{mix_0}}$ is the average of the effective density of the leaving mixture. This last term depends on the average gas volume fraction of the leaving mixture at ambient conditions.

Eventually, the volume of the mixture leaving is the sum of the volume of air and oil entering the control volume. This is the consequence of having same inlet and outlet pressures and temperatures for air. Diaz considered the mixture leaving the damper as representative of the whole mixture present in the damper. This allows to state that the mixture density is a function only of the local pressure and, the average density and can be approximated as the one at the average pressure. To fully evaluate the mean air volume fraction at ambient conditions, we need to calculate the mean volume of air entering the CV (control volume). The hypothesis, behind the calculation of the value mentioned above, is to consider that, when the film volume grows fast enough, the volume not filled by the oil is filled by air. The author introduces a dimensionless parameter, valid for short length bearing executing circular centered orbits, to evaluate the occurrence of air ingestion:

$$\gamma = \frac{Q_{oil}}{Le\omega\pi D} \tag{13}$$

Where Q_{oil} is the volume flow rate of lubricant.

Air is entrapped only when γ is lower than one i.e. the increase of the damper's volume is not filled. The author used this method to calculate the length of the zone of constant pressure, typical for operation with air entrainment, and the correlation with the experimental results, is more than acceptable for an air volume fraction lower than 0.6. Eventually, Diaz, reports a comparison between the experimental data and the model predictions of the operation of an open-ends SFD executing circular centered orbits. Different supply oil flow and whirl frequency are considered. In both cases a good fitting exists for the operations when air entrainment is moderate. With reduced oil supply, the reason of bad correlation may be the coalescence of bubbles resulting in a non-homogeneous flow.

Some years later Mendez et al. [31] adapted Diaz's model to finite length bearings. Some considerations must be done. At first the tangential flow cannot be neglected so, to evaluate the air volume ratio, equation (7) cannot be adopted and the definition of β_0, coming from the flow balance for an SFD executing CCO, must be used. The air flow must be computed numerically from the solution of the modified Reynolds equation. The author considered three different boundary conditions to evaluate the feeding i)uniform flow, ii)uniform velocity, iii)uniform pressure. These conditions were applied to Diaz's model and, from a comparison with experimental results, the uniform pressure one was considered as most appropriate and not the uniform flow which was, instead, chosen by Diaz. From the analytical study Mendez derived that, increasing the axial dimension of the damper, the air entrapped, for the same value of γ, is decreased with respect to the infinitely short conditions. This effect is beneficial especially for low values of γ and becomes milder when it tends to 1. This behavior is reflected in the pressure evolution, consequently on the forces, with the air volume fraction showing that the actual dynamic behavior of finite length dampers, in case of air ingestion, is better than the one predicted with the infinitely short hypothesis.

Tao et al. in [32] Developed a continuum model to simulate the operation of SFDs, describing CCOs, with bubbly lubricant and compares the results obtained with the same experimental data used in [29] by Diaz. The lubricant is considered as an incompressible Newtonian fluid while air is considered as an inviscid perfect gas. The bubble size is considered similar to the radial clearance, the problem is considered isothermal, the velocities of the oil and the air bubbles are considered identical and the effect of lubricant's cavitation, both vapor and gaseous, is neglected. The author starts from the mass conservation equations, for both oil and air, and the balance of linear momentum of the bubbly flow. Neglecting the surface tension is possible to consider the same pressure for the bubbles and the lubricant. The most difficult step in the modelling is the determination of the mixture viscosity, for simplicity a fourth order polynomial expression of the gas volume fraction is used. The equations are then expressed in non-dimensional terms, since the ratio between the clearance and the radius of the damper is usually much smaller than one, the inertia effects are neglected. This also indicates that the lubricant film is isobaric along the thickness if the gas volume fraction is also constant. Once the boundary conditions are given, it is possible to solve the equations if a reference value for the gas volume fraction is given, Tao used the value found in the experiments he then used for the comparison. The author also indicates as an alternative the procedure proposed by Diaz in [29]. The results obtained show a good correlation with the experimentally derived peak-to-peak film pressure up to a reference gas volume fraction equal to 0.6. At higher whirling frequency the discrepancy between the results is increased, probably due to the inadequacy of the expression used to evaluate the flow viscosity. The author also reports the correlation between the tangential and radial forces obtained analytically and experimentally. In the first case the correlation is promising up to reference air volume fraction in the mixture equal to 0.6 but it decreases when the whirling frequency grows. In the second case the discrepancy is important, Tao proposes as possible justification the effect of a hydrostatic effect not accounted in the model.

As mentioned above, Diaz in [29] used a simplified form of the Rayleigh-Plesset (RP) equation to model open-ends SFDs, Gehannin et al. in [33] considered instead the complete form of the equation and proposes a comparison with experimentally derived measures to evaluate the impact of these two different decisions on the accuracy of the model. The lubricant is considered as a mixture of fluid and nuclei, represented by spherical bubbles, formed by vapor and gas. The RP equation, (14), describes the variation of the bubble's radius (R_B) at rest surrounded by an infinite incompressible fluid subjected to external pressure. The first term of the equation is the difference between the pressure inside the bubble and outside (p), the first one is the sum of the partial pressure of the gas in the bubble and the vapor term (p_B). The second term is the damping effect due to viscosity and the third term is the surface tension (S). The two terms on the right side represent the inertia effect.

$$p_B - p - \frac{4\mu_L}{R_B}\frac{dR_B}{dt} - \frac{2S}{R_B} = \rho_L R_B \frac{d^2R_B}{dt^2} + \frac{3}{2}\rho_L\left(\frac{dR_B}{dt}\right)^2 \tag{14}$$

The authors report a model found in the literature where the inertial terms are neglected and a dilatation viscosity (κ), supplementary effect of the surface tension, is added, equation (15). This cited model is applied to journal bearings and, according to the authors, is not suitable to represent a SFD because the mixture of lubricant and bubbles is not rotating around the journal. For this reason, the bubble is subject mainly to the time variation in the local pressure rather than to the pressure variation due to its transport velocity. The RP equation used, with partial time derivatives, is then:

$$\frac{p_B - p}{\rho_L} - \frac{4\nu_L}{R_B}\dot{R_B} - \frac{2S}{R_B\rho_L} - \frac{4\kappa}{R\rho_L}\dot{R_B} = R_B\ddot{R_B} + \frac{3}{2}\dot{R_B}^2 \tag{15}$$

Where ν_L is the lubricant's kinematic viscosity.

The pressure field inside the SFD is obtained solving the unsteady Reynolds equation for a compressible lubricant where the lubricant is considered as a homogeneous mixture of liquid oil and bubbles. The properties of the fluid are obtained with the same equations used by Diaz, equations (9), (10). From the experimental results this new model seems more appropriate than the one proposed by Diaz. Gehannin also showed the influence of each term of the RP equation on the pressure field. It is possible to notice that the inertia terms and the viscous damping have a negligible effect, the surface tension has a slight influence, the bubble pressure and the dilatation viscosity have the biggest effect. The inclusion of the surface dilatation viscosity is needed to predict the negative peak in pressure, unfortunately experimental values of κ are rare.

In [34], the authors, propose a new model for the evaluation of the dynamic response of SFDs based on the bulk flow equations. The aim is to overcome the difficulties encountered by other models, that often lack of generality, in the prediction of the effects of geometrical details, like the presence of grooves and sealing devices, that strongly affect the inertia of the flow. In the model it is also considered the effect of cavitation: vapor, gaseous and air entrainment. The author proposes to neglect the diffusion of air outside of the bubble because the characteristic time scale of the SFD is much smaller than the one of air diffusion: the only options in order to have a gaseous phase in the mixture is due to oil vaporization and air entrainment. The starting equations are:

$$\begin{cases} \frac{\partial}{\partial t}(\rho U h) + \frac{\partial(\rho U^2 h)}{\partial x} + \frac{\partial(\rho U W h)}{\partial z} = -\frac{\partial P}{\partial x}h - \tau_{Sx} - \tau_{Rx} \\ \frac{\partial}{\partial t}(\rho W h) + \frac{\partial(\rho W^2 h)}{\partial z} + \frac{\partial(\rho U W h)}{\partial x} = -\frac{\partial P}{\partial z}h - \tau_{Sz} - \tau_{Rz} \\ \frac{\partial}{\partial t}(\rho h) + \frac{\partial(\rho U h)}{\partial x} + \frac{\partial(\rho W h)}{\partial z} = 0 \end{cases} \tag{16}$$

Where U and W are the average circumferential and axial velocities, $\tau_{Sx,z}$ is the stator circumferential or axial shear stress while $\tau_{Rx,z}$ is the rotor circumferential or axial shear stress.

This system is integrated by using the finite volume method on a collocated grid and the SIMPLE algorithm. It is interesting to notice that the bulk flow equations are based almost on the same assumptions behind the Reynolds equation, the main difference is that the firsts take fully into account the convective inertia terms. When deducing the system of equations only average velocities were considered and one of the available friction laws in literature were used to evaluate the wall shear. To validate these hypotheses, a comparative study with CFD was developed. The results show that the bulk flow model is appropriate in predicting the pressure evolution for Re values below 50: exactly the operating region of SFDs. An adequate correspondence between the data is shown also for the radial and tangential force, even when the clearance is increased.

The simplified hypothesis of constant pressure is abandoned for dealing the feeding groove, the bulk flow equations are applied to the real depth of the groove. To overcome the problem of a discontinuous thin film the author applied an approach already common in the analysis of annular seals. The cell faces of the discretization grid will coincide with the boundary of the groove and the discontinuities of height. The pressure field is continuous inside the groove and in the film, but a discontinuity is present at the interface. This discontinuity derives from the concentrated inertia effects that will be described with the generalized Bernoulli equation.

The authors also investigate the effect of the feeding orifices. It was considered that, according to the operating condition, the lubricant could both enter and exit the orifice. Since the diameter of the orifice is usually larger than the dimension of the cell, the best compromise between accuracy and calculation effort is to consider the cell that contains the orifice in a special manner. The dimension of the cell will be close to the one of the orifice. This approximation will only affect the pressure field in the close neighborhood. The orifice was then modeled as an unsteady source of mass and the bulk flow equations are modified, taking into consideration the flow pattern inside the orifice.

A model for vapor cavitation is included in the analysis. The authors noticed that none of the models present in literature has ever been used in conjunction with the bulk flow equations. The authors used the Rayleigh-Plesset equation, equation (15), as shown also in [35], because it is easy to include it in the bulk flow equations and can predict the bubble implosion. The lubricant is considered to be contaminated by small bubbles, filled with gas and oil’s vapor. The mass of the gas inside the bubble is taken as constant such as the density of the vapor, with this assumption the growth and reduction of the bubble involves only a vapor mass transfer from the liquid to the bubble and vice versa. Taking into consideration the weight of the terms of the RP equation on the dynamic pressure evolution, [33], the author decided to neglect the inertial terms but viscous damping, surface tension and surface dilatation viscosity, although negligible, are kept in the analysis due to their positive effect on the numerical stability. The RP equation is needed to evaluate the radius of the bubble, function of the pressure calculated with the bulk flow equations. The radius is than used to obtain the gas volume fraction, fundamental to evaluate the density of the fluid. The viscosity is kept constant when mass transfer is neglected. The analysis of the calculated pressure profile shows it is possible to notice the similarity with the experimental data analyzed for comparison. It is also possible to predict the peak in pressure at the beginning of the constant zone, caused by the bubble implosion for higher Reynolds numbers.

As stated before, usually SFDs are equipped with end seals that prevent air ingestion and increase the damping effect. Usually, complete sealing is not achieved because it is necessary to evacuate the dissipated power with a leakage flow. This is achieved with a series of axial grooves machined on the circumference of the piston ring. In the literature it is possible to find some models where the leakage flow is considered as uniformly distributed over the circumference of the sealing device and its value is determined by a discharge coefficient. A different approach is taken by the author, the opening slot is considered as a narrow rectangular channel. The mono-dimensional momentum equation is applied.

Eventually, the comparison between the results obtained with this new model, a set of experimentally derived data and a model based on the 1-D Reynolds equation is shown. It is considerable the difference between the two models. The agreement between the experimental data and the bulk flow model is evident for different dimensionless whirling radius, i.e. e/cl. The improvement in the predictions, achieved by this new model, with respect to the model based on the 1D Reynolds equation is remarkable.

In [35], the authors complete their analysis introducing a model to take into consideration the air ingestion and entrapment in the operation of SFDs. The approach followed is different from what can be found in the literature, see [29]. Air entrapment is dealt with by considering the lubricant and the entrained air as separate and immiscible phases. The interface of air bubbles is numerically tracked, using the volume of fluid method. The author introduces a scalar function, (F), obtained from a transport equation, which represents the volume fraction of liquid in a computational cell. This method is already present in the literature and is used to model flows with separated phases, the author adapted it to lubrication problems.

The staring equation is:

$$\frac{\partial F}{\partial t} + \vec{\nabla} \cdot \left(F\vec{V}\right) = F\left(\vec{\nabla} \cdot \vec{V}\right) \tag{17}$$

The source term is zero for incompressible lubricant, but it is kept as a correction term. The equation is then integrated over the film thickness, considering the volume fraction of lubricant F constant across it. The author then describes in detail how to treat the computational cells and the further care to take when a cell accepts flow from two adjacent cells. If F is the lubricant volume fraction of the mixture, $1 - \mathrm{F}$ is the volume fraction of vapor and ingested air. The properties of the mixture depend on i) this last value, ii) the properties of the pure lubricant, iii) the ones of the vapor phase and iiii) the non-condensable gas. To improve the numerical solution, in the close vicinity of the interface between the lubricant and the ingested air, both fluids are considered as immiscible and incompressible so, there, the density is considered constant and equal to the lubricant's one. After a comparison with experimental results, is possible to say that the model presented can be a reliable tool to predict the behavior of SFDs with bubbly lubricant. Lastly the authors report some simplifications that can be done to the model. At first the air viscosity is much lower than the lubricant's and so it is approximated as 1% of the second one to reduce the computational time. It was observed that it is reasonable to consider a strictly circumferential interface and that the circumferential velocity has a minor role in the identification of the axial location of the interface. For open-ends dampers it is possible to completely neglect the circumferential velocity.

None of the cited authors considered the effect of the temperature increase during the continuous operation of the bearing. In [36], it is proposed to include in the Reynolds equation model, also the effect of the temperature increase incorporating the energy equation for the lubricant film and the Laplace heat conduction equations for the solid components. This approach is already largely utilized in the modeling of hydrodynamic bearings.

In the recent years, thanks to the constant growth of the computational resources available, computational fluid dynamics has become one of the most used tool to study turbomachines but also lubrication problems. Many examples of application of CFD in the study of squeeze film dampers are present nowadays. In most of the cases, CFD analysis are used as comparison with other models available especially if experimental data is not available. In [37] the work on Diaz and San Andres on the effect of air ingestion, [30], is compared with results obtained with CFD reporting similar results. In [38] the effect of air ingestion on the dynamic performances of the damper is evaluated. In both cases vapor cavitation is not considered so to assess only the effect of air entrapment. Finally in [39] CFD is used to model the behavior of dampers considering the presence of central grooves, exit seals and feeding mechanism reporting results similar to what shown in previously mentioned models.

2. SFD MODEL

The goal of this work is to create a simplified model, efficient from the computational point of view, to predict the behavior of general squeeze film dampers, taking into consideration the different aspects highlighted in the previous chapter. The most suitable approach, then, is to take the Reynolds equation as the characteristic law describing the physics governing the behavior of the oil film. A model based on the bulk flow equations would result in a more precise tool, with results close to these obtained through CFD analysis, [34]. The higher precision, on the other hand, would result in higher computational cost that, together with the higher complexity of the model, is above the goal of this thesis. It is also important to keep in mind that, in order to correctly simulate with CFD the behavior of the damper, the final part of the feeding circuit must be modeled. Also for this reason, this approach can be adopted as a final stage design investigation to finely tune the damper.

It is possible to find many models based on the Reynolds equation in the scientific literature, for the majority of them the authors develop their own solution method based on the finite differences, [17]. In this work, a similar approach was adopted: the Reynolds equation was discretized with the finite difference technique and solved.

As mentioned in the previous chapter, the approach on the analysis of the dynamic performance of squeeze film dampers is to simulate circular orbits of the shaft, whether centered or not, or small movement around the position of equilibrium. For simplicity, the model proposed is developed for centered circular orbits but it can easily be adopted for non-centered circular orbits or even non circular orbits and oscillations around the equilibrium position if it is possible to identify a function that describes the behavior of the oil film thickness as a function of the time.

If the shaft describes CCOs, the orbits are like in Fig. 2-1.

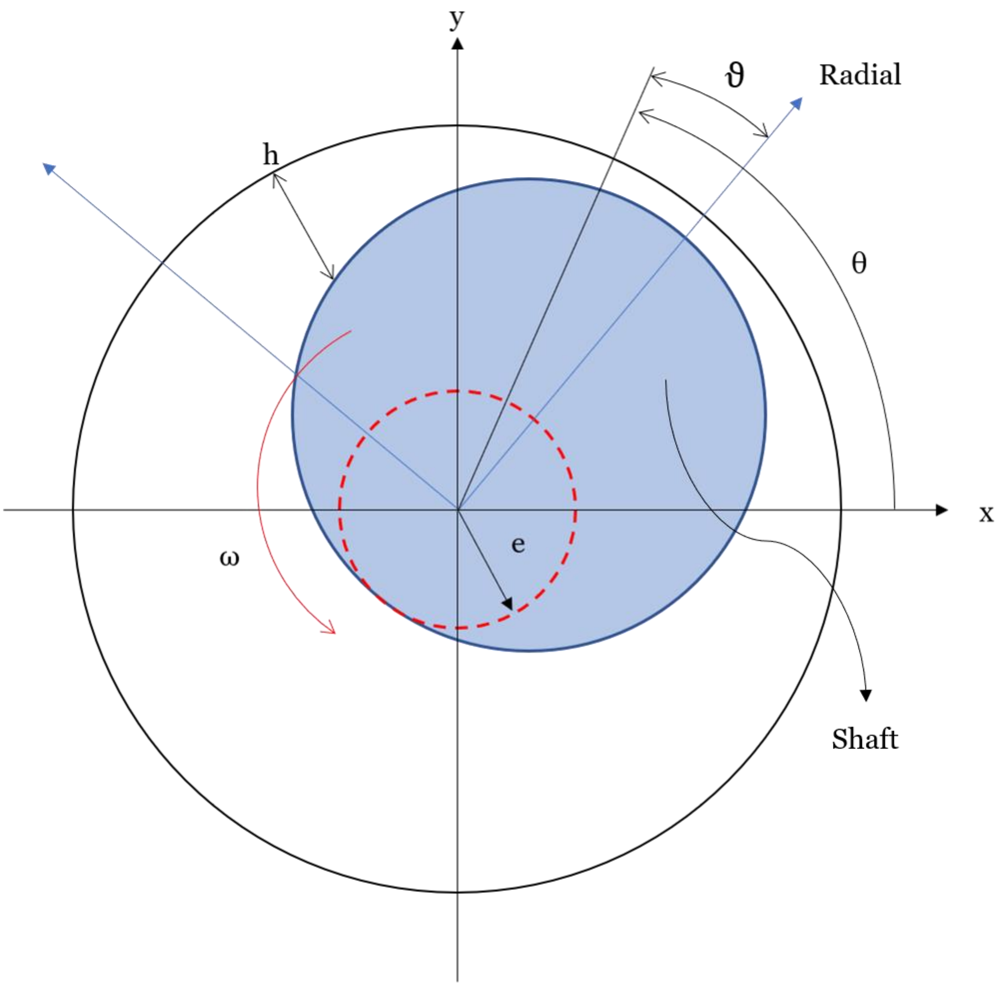

Fig. 2-1 Example of shaft describing circular centered orbits

Note that:

$$\theta = \vartheta + \omega t \tag{18}$$

It is possible to choose both the fixed and the rotating coordinate system, in this model the first one is chosen. It is then possible to write the variation of the oil film thickness in time and space:

$$h(\theta, t) = cl - (e\cos\omega t + e_s \cos\theta_s)\cos\theta - (e\sin\omega t + e_s \sin\theta_s)\sin\theta \tag{19}$$

Where e_s is the value of the static eccentricity and θ_s the phase of the static eccentricity. The big advantage of considering circular orbits, centered or not, is that there is a direct relationship between time and space given by the rotational speed ω. If no local oil supply or discharge ports are present, the pressure equation is stationary in the rotating frame system. For this reason, any derivative in time can be transformed in:

$$\frac{\partial}{\partial t} = -\omega\frac{\partial}{\partial\vartheta} \tag{20}$$

Considering equation (18), at each time instant, it is possible to add:

$$\frac{\partial}{\partial t} = -\omega \frac{\partial}{\partial \vartheta} = -\omega \frac{\partial}{\partial \theta} \tag{21}$$

If the orbiting frequency remains constant in time, thanks to equation (21) it is possible to write every time derivative as a spatial derivative. This transformation allows to reduce the calculation time: the simulation at one time instant is representative of the behavior of the oil for the entire orbit of the shaft.

In order to simplify the discussion, the different models developed are catalogued as follows:

A. Reynolds equation

B. Reynolds equation with inertia effect

C. Reynolds equation with LCP

D. Reynolds equation with Elrod's cavitation algorithm

E. Reynolds equation with iterative solution

F. Reynolds equation with air ingestion

2.1. Reynolds equation

The general equations to describe the dynamic behavior of a viscous Newtonian fluid are the 3-D Navier-Stokes equations:

$$\frac{\partial \rho}{\partial t} + \nabla \cdot \left(\rho \vec{V}\right) = 0 \tag{22}$$

$$\rho \left(\frac{\partial \vec{V}}{\partial t} + \vec{V} \cdot \nabla\left(\vec{V}\right) \right) = -\nabla P + \nabla \cdot \left(\mu \nabla \vec{V}\right) + \nabla\left(-\frac{2\mu}{3} \nabla \cdot \vec{V}\right) + \rho g \tag{23}$$

Where (22) is the continuity equation and (23) are the conservation of momentum within the fluid boundary.

Taking into consideration the squeeze film damper application it is possible to adopt some simplifying hypothesis like:

- Fluid density ρ is considered constant, valid if cavitation is not present.
- Fluid kinematic viscosity is constant, valid if temperature can be considered almost constant.
- Inertia and body forces are neglected.
- Fluid flow is considered laminar.

Considering the geometry of the damper and the fact that the fluid thickness is very small, the curvature of the surfaces can be neglected, the surfaces can be considered as planes. Moreover, the circumferential and axial length of the damper are about three orders of magnitude larger than the film thickness so the velocity gradients along the first two dimensions are negligible. The system of equations becomes:

$$\frac{\partial P}{\partial x} - \mu \cdot \left(\frac{\partial^2 u}{\partial z^2}\right) = 0 \tag{24}$$

$$\frac{\partial P}{\partial y} - \mu \cdot \left(\frac{\partial^2 v}{\partial z^2}\right) = 0 \tag{25}$$

$$\frac{\partial P}{\partial z} = 0 \tag{26}$$

Equations (24) and (25) can be integrated and applying non-slip boundary conditions the expressions for u and v are obtained. Finally substituting them in the continuity equation the Reynolds equation is obtained:

$$\frac{\partial}{\partial x}\left(h^3 \frac{\partial P}{\partial x}\right) + \frac{\partial}{\partial z}\left(h^3 \frac{\partial P}{\partial z}\right) = 12\mu \frac{\partial}{\partial t}(h) \tag{27}$$

This equation is valid for finite length dampers but it can be further simplified in case of short damper or infinitely long damper configuration, [7]. The fluid density is not present because in case of incompressible fluid it cancels out from the equation. Equation (27) is the one adopted for model A.

The local dimensionless pressure evolution in time of a simple SFD is shown in Fig. 2-2. The boundary conditions are no axial gradient at one side and ambient pressure at the other.

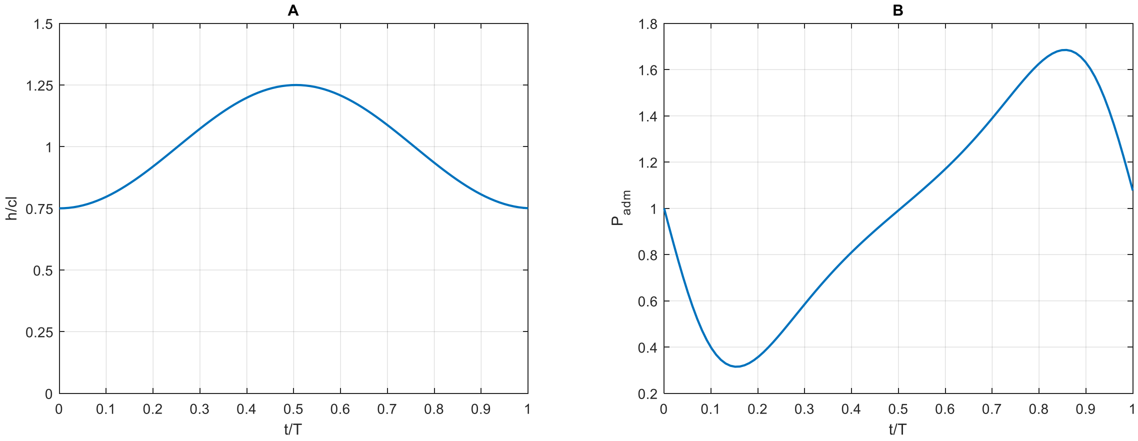

Fig. 2-2 A) Dimensionless oil film thickness over time B) Dimensionless pressure over time for model A

As stated before, the pressure is decreased when the oil thickness increases, meaning that the shaft is moving away from the position in which the pressure is evaluated. On the contrary when the shaft is moving toward the detection point, the oil thickness is decreasing, determining an increase in pressure.

In Fig. 2-3 it is possible to appreciate the three-dimensional representation of the pressure evolution inside the damper. Remember that the shaft is orbiting in a counter-clockwise direction so, a zone of positive pressure is formed ahead of the shaft, acting as an obstacle to the shaft movement. The orbit radius and the external cage are not represented in scale for a clarity purpose.

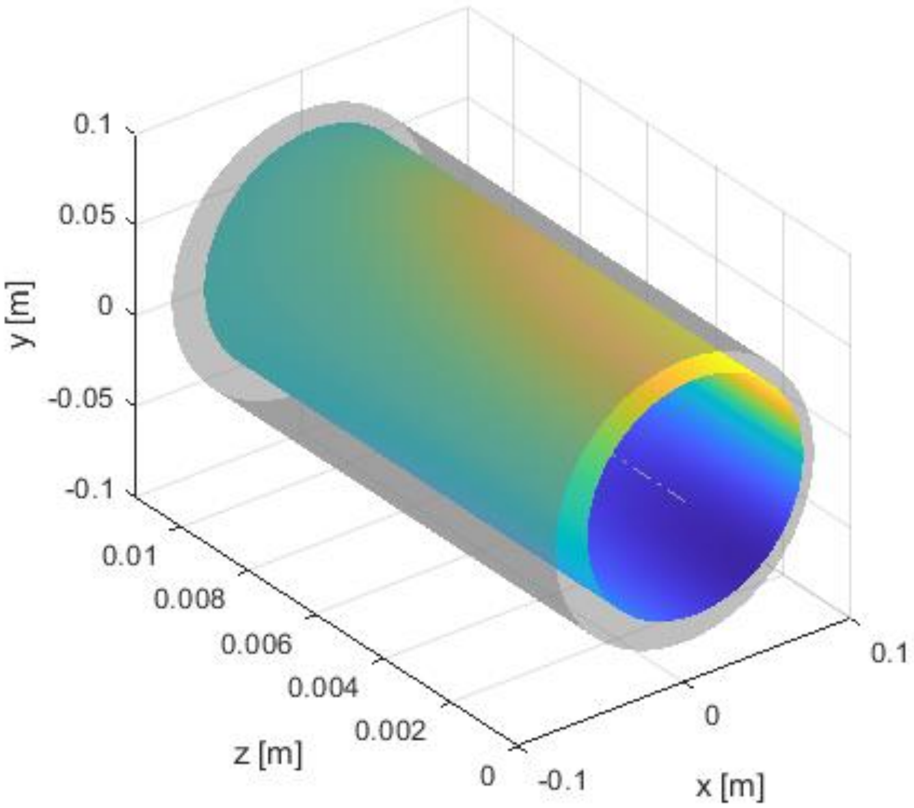

Fig. 2-3 3-D representation of dimensionless pressure for model A

2.2. Inertia

In general, the fluid inertia forces are negligible if the value of the squeeze film Reynolds number is below 1. In case of high vibration frequencies, result of higher rotational speed of the shaft, or dampers with larger clearance, for example in case of inlet and outlet grooves, this value is greater than one and is usually lower than 50, [8]. As reported in [20] and [36], models that include inertia's effect give results closer to ones obtained experimentally for both force coefficients.

If the inertial effect is kept in the fluid equations, the equations of continuity of momentum have some extra terms:

$$\frac{\partial P}{\partial x} - \mu \cdot \left(\frac{\partial^2 u}{\partial z^2}\right) = -\rho\left(\frac{\partial u}{\partial t} + u\frac{\partial u}{\partial x} + v\frac{\partial u}{\partial y} + w\frac{\partial u}{\partial z}\right) \tag{28}$$

$$\frac{\partial P}{\partial y} - \mu \cdot \left(\frac{\partial^2 v}{\partial z^2}\right) = -\rho\left(\frac{\partial v}{\partial t} + u\frac{\partial v}{\partial x} + v\frac{\partial v}{\partial y} + w\frac{\partial v}{\partial z}\right) \tag{29}$$

$$\frac{\partial P}{\partial z} = 0 \tag{30}$$

The effect of inertia is then considered as a first order perturbation of the inertia-less case. In non-dimensional terms:

$$\bar{P} = \overline{P_0} + Re\overline{P_1} \tag{31}$$

The same can be written for the velocities.

Substituting equation (31) and the equivalent for velocities in (28), (29), (30) and the continuity equation two Reynolds like equations are obtained. Integrating the first one $\overline{\mathrm{P}_0}$, the inertia-less term is obtained, integrating the second one $\overline{\mathrm{P}_1}$, the first-order correcting term for inertia is obtained.

As mentioned in the previous chapter, it is legitimate to hypothesize that, for moderate values of Re, fluid inertia does not influence the shape of the purely viscous velocity profiles. Moreover, considering average quantities in the flow equations the wall shear stress differences are approximated, [19].

In this work an approach similar to the one proposed in [19], a single Reynolds-like equation was considered in which the effect of temporal inertia was added. Convective inertia terms are considered negligible, [20]. The equation used in the model is:

$$\frac{\partial}{\mathrm{R}\,\partial\theta}\left(\frac{h^3}{12\mu}\frac{\partial P}{R\partial\theta}\right) + \frac{\partial}{\partial \mathrm{z}}\left(\frac{h^3}{12\mu}\frac{\partial P}{\partial \mathrm{z}}\right) = \frac{\partial}{\partial \mathrm{t}}(h) + \frac{Reh^2}{12\omega c^2}\frac{\partial^2 h}{\partial \mathrm{t}^2} \tag{32}$$

The inclusion of the temporal inertia term will contribute to the modification of the pressure profile obtained in the damper. Equation (32) is the reference one for model B.

In Fig. 2-4 the same damper as in Fig. 2-2 is tested with the new Reynolds equation in order to appreciate the effect of the inertial term. In Fig. 2-5, the comparison between the pressures obtained with and without the inertial term is presented. It is possible to notice that the pressure, considering the inertial term, remains larger than the ambient one for a longer time and remains flatter than the one obtained with the classical Reynolds equation. The maximum value is reduced and slightly shifted, like the minimum value. In this case the Reynolds number is about 3.5. The addition of the temporal inertia term determines the presence of a radial acceleration whose effect is counterbalanced by the formation of an inertial pressure field resulting in a radial force.

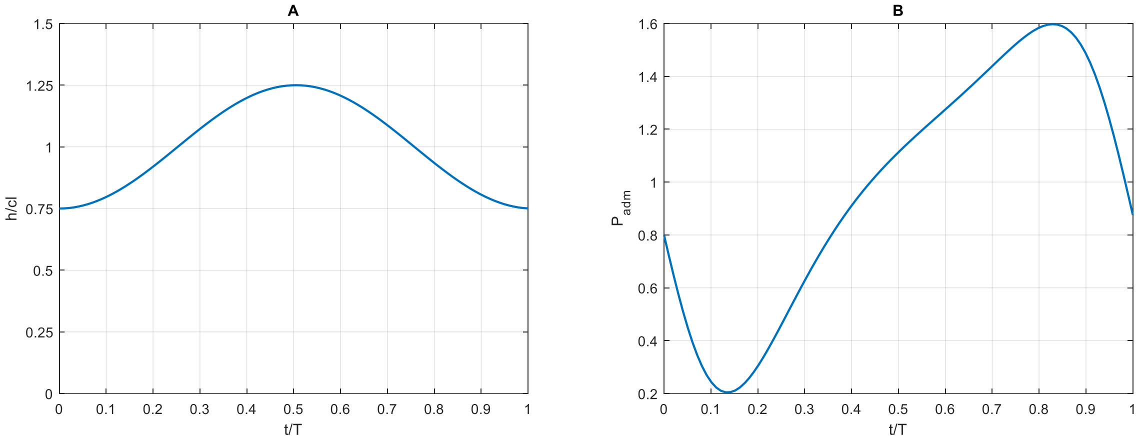

Fig. 2-4 A) non-dimensional oil thickness B) non-dimensional pressure over time: model B

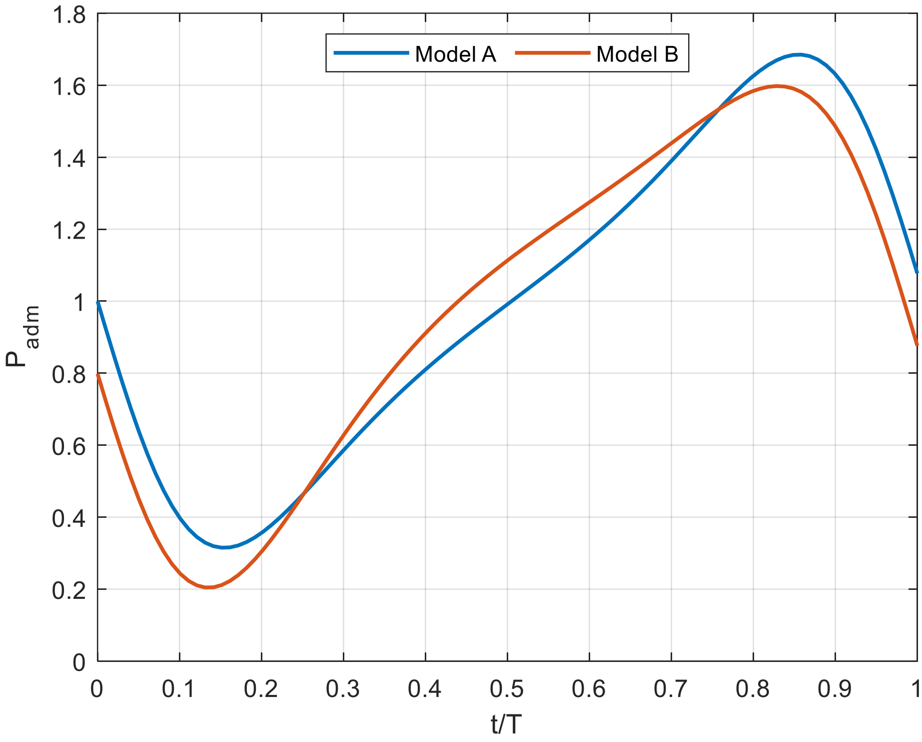

Fig. 2-5 Comparison between non-dimensional pressure of model A and model B

2.3. Air ingestion

The treatment of cavitation is the most critical aspect of the model. As shown in the previous paragraph, SFDs are sensible not only to vapor cavitation and bubble formation in the negative squeeze region, but also to air ingestion and entrapment from the outside.

One of the most adopted method to treat cavitation in bearings is the Elrod algorithm, [9]. In this method the bulk modulus of the liquid, description of the variation between density and pressure, is used linked to a switch function to divide the cavitated zone and the non cavitated one. As reported in [32], this algorithm is not able to predict the effect of air entrapment in the damper.

In order to fully consider the effect of air entrainment, the same approach adopted by Diaz in [32] was chosen. The Reynolds equation must be modified so to consider that now the fluid is compressible and both density and viscosity are affected by the presence of air bubbles.

The complete set of equations adopted in model F is:

$$\frac{\partial}{\mathrm{R}\,\partial\theta}\left(\frac{\rho h^3}{12\mu}\frac{\partial P}{R\partial\theta}\right)+\frac{\partial}{\partial \mathrm{z}}\left(\frac{\rho h^3}{12\mu}\frac{\partial P}{\partial \mathrm{z}}\right)=\frac{\partial}{\partial \mathrm{t}}(\rho h)+\frac{Reh^2}{12\omega c^2}\frac{\partial^2 \rho h}{\partial \mathrm{t}^2} \tag{33}$$

$$\rho = (1-\beta)\rho_L \tag{9}$$

$$\mu = (1-\beta)\mu_L \tag{10}$$

$$\beta = \frac{1}{1+\frac{P(x,t)-P_v}{P_{G\sigma}}(\frac{1}{\beta_0}-1)} \tag{7}$$

Where β_0 is the reference gas volume fraction. It is calculated considering the mass balance of oil and air entering the damper and mixture leaving. So:

$$\beta_0 = \left(1+\frac{2\pi\gamma}{\gamma(2\sin^{-1}(\gamma)-\pi)+2\sqrt{1-\gamma^2}}\right)^{-1} \tag{34}$$

Where γ is as in equation (13) and represent the ration between the oil inflow and the volume change due to the shaft movement. Equation (34) and (14) are developed considering valid the short-length approximation, evaluating the overall mass flow of oil, air and mixture. Generally speaking, the short-length bearing approximation is not always applicable, for example, it is limited to ratios of length over diameter of the damper below 0.2. In [31] it is proposed to numerically evaluate the volumetric inflow of air at the sides of the damper and evaluate the new reference value of volume air fraction. The pressure cycle is then repeated with the updated value of β_0. This procedure is continued until the convergence on β_0, according to a certain convergence criterion, is reached. A procedure similar to this one will be adopted in the present work and the starting value of reference volume fraction of ingested air will be considered zero.

2.4. Negative pressure zone

As mentioned above, many models and algorithms are present in literature to deal with cavitation. In this work, only vapor cavitation is taken into consideration. Different models and algorithm were studied. For model C two different approaches are presented. At first, a model, based on [10], where LCP is used to solve the negative pressure problem is implemented. This approach is called model C.1. For linear complementarity two independent variables are needed and their product must be zero in the whole domain. Equation (33) is valid in both the negative and positive squeeze region. For now air ingestion and entrapment is not considered. The density is considered as constant and equal to the oil density in the active region while, in the cavitated region, a mixture of oil, gas and vapor is present, characterized by a lower density. Density is replaced with:

$$r = 1 - \frac{\rho}{\rho_L} \tag{35}$$

In the active region of the damper, where the pressure is higher than the vapor pressure, $r = 0$ while in the cavitated region, pressure is constant and, omitting the constant value of the vapor pressure, equal to zero and $r \geq 0$. So:

$$rP = 0 \tag{36}$$

If density is replaced with the new variable in the Reynolds equation, omitting the partial derivative on the axial direction for brevity, we obtain:

$$\begin{aligned} \frac{\partial}{R\,\partial\theta}\left(\frac{h^3}{12\mu}\frac{\partial P}{R\partial\theta}\right) - \frac{\partial}{R\,\partial\theta}\left(\frac{rh^3}{12\mu}\frac{\partial P}{R\partial\theta}\right) \\ = -\frac{\partial}{\partial t}(rh) + \frac{\partial}{\partial t}(h) - \frac{Reh^2}{12\omega c^2}\frac{\partial^2 rh}{\partial t^2} + \frac{Reh^2}{12\omega c^2}\frac{\partial^2 h}{\partial t^2} \end{aligned} \tag{37}$$

Only the second term in (37) contains both the complementary variables. Notice that in the cavitated region $r = 0$ and in the active region $P = P_v$ so its derivative is zero. Eventually:

$$\frac{\partial}{R\,\partial\theta}\left(\frac{rh^3}{12\mu}\frac{\partial P}{R\partial\theta}\right) = 0 \tag{38}$$

The same holds for the component on the axial direction. The final equation to be solved is:

$$\begin{aligned} \frac{\partial}{R\,\partial\theta}\left(\frac{h^3}{12\mu}\frac{\partial P}{R\partial\theta}\right) + \frac{\partial}{\partial z}\left(\frac{rh^3}{12\mu}\frac{\partial P}{\partial z}\right) \\ = -\frac{\partial}{\partial t}(rh) + \frac{\partial}{\partial t}(h) - \frac{Reh^2}{12\omega c^2}\frac{\partial^2 rh}{\partial t^2} + \frac{Reh^2}{12\omega c^2}\frac{\partial^2 h}{\partial t^2} \end{aligned} \tag{39}$$

The equation is then discretized with the finite difference technique, a first order backward scheme is used for the terms with r, a second order central difference scheme is used to discretize the other derivatives, a system of linear equations can be written for the internal points of the domain:

$$\bar{\bar{A}} \cdot P = \bar{\bar{B}} \cdot r + f \tag{40}$$

Time derivatives are rewritten as circumferential derivatives thanks to (21). Notice that the boundary conditions enter in the vector f. Eventually:

$$P = \bar{\bar{M}} \cdot r + q \tag{41}$$

Where $\bar{\bar{M}} = \bar{\bar{A}}^{-1} \cdot \bar{\bar{B}}$ and $q = \bar{\bar{A}}^{-1} \cdot f$.

One of the frequently used algorithms to solved linear complementarity problems is the Lenke's pivoting algorithm, in this work a vectorized MATLAB version of a pivoting algorithm is used, [40].

A separate approach is adopted to deal with the change of the Reynolds number caused by the change of density in the domain. Considering the new variable the inertial term should be written as:

$$-\frac{Reh^2}{12\omega c^2}\frac{\partial^2 rh}{\partial \mathrm{t}^2} + \frac{Reh^2}{12\omega c^2}\frac{\partial^2 h}{\partial \mathrm{t}^2} = -(1-r)\frac{Re_L h^2}{12\omega c^2}\frac{\partial^2 rh}{\partial \mathrm{t}^2} + (1-r)\frac{Re_L h^2}{12\omega c^2}\frac{\partial^2 h}{\partial \mathrm{t}^2} \tag{42}$$

Where Re_L is the Reynolds number calculated with the oil density. To avoid the non - linearity introduced by the second term, the equation is solved iteratively updating the Reynolds number as $Re = (1-r)Re_L$ at each iteration until convergence is reached. The same approach is used also in the following model.

The second approach adopted for model C, model C.2 is present in [12] where fluid compressibility is taken into consideration considering:

$$\rho = \rho_c e^{\frac{P-P_v}{B}} \tag{43}$$

Where ρ_c is the density at cavitation and B is the bulk modulus of the fluid. For lubricant oil its value is around $10^9[Pa]$ and is affected by temperature, pressure and the gas content of the oil. The dependency with pressure is effective starting from values ($500\,MPa$) that are two or thee orders of magnitudes higher than what is reached inside the dampers, see [41]. If the bulk modulus is equal to the one of the oil, the lubricant is considered uncompressible, $\rho_c = \rho_L$ and the model in [12] is the same as the one in [10].

In the whole domain:

$$\rho = \rho_c \begin{cases} e^{\frac{P-P_v}{B}} & P > P_v \\ \delta & P = P_v \end{cases} \tag{44}$$

Where δ is a saturation function.

Equation (33) becomes:

$$\rho_c \begin{cases} \dfrac{\partial}{\partial x}\left(\dfrac{e^{\frac{P-P_v}{B}} h^3}{12\mu}\dfrac{\partial P}{\partial x}\right) - \dfrac{\partial}{\partial t}\left(e^{\frac{P-P_v}{B}} h\right) - \dfrac{Reh^2}{12\omega c^2}\dfrac{\partial^2}{\partial t^2}\left(e^{\frac{P-P_v}{B}} h\right) & P > P_v \\ -\dfrac{\partial}{\partial t}(\delta h) - \dfrac{Reh^2}{12\omega c^2}\dfrac{\partial^2}{\partial t^2}(\delta h) & P = P_v \end{cases} \tag{45}$$

The derivative along the axial direction is neglected for brevity.

It is possible to notice the non-linearity in pressure of the first term of the first equation. For this reason, a new variable is introduced:

$$\bar{u} = e^{\frac{P-P_v}{B}} - 1 \tag{46}$$

In order to guarantee the linear complementarity, $\eta = 1 - \delta$ is adopted. In fact:

$$\begin{matrix} P > P_v & \bar{u} > 0 & \eta = 0 \\ P = P_v & \bar{u} = 0 & \eta > 0 \end{matrix} \tag{47}$$

The new equation to be solved, once the new variables are substituted in equation (63), is:

$$\begin{aligned} &\frac{\partial}{\partial x}\left(\frac{Bh^3}{12\mu}\frac{\partial \bar{u}}{\partial x}\right) - \frac{\partial}{\partial t}(\bar{u}h) - \frac{Reh^2}{12\omega c^2}\frac{\partial^2}{\partial t^2}(\bar{u}h) \\ &\qquad = \frac{\partial h}{\partial t} + \frac{Reh^2}{12\omega c^2}\frac{\partial^2 h}{\partial t^2} - \frac{\partial}{\partial t}(\eta h) - \frac{Reh^2}{12\omega c^2}\frac{\partial^2}{\partial t^2}(\eta h) \end{aligned} \tag{48}$$

Also in this case the time derivatives are written as circumferential derivatives thanks to equation (21).

The equation is discretized with the finite difference technique where the terms with η are written with a first order backward scheme and all the others with second order central difference scheme. A system of linear equations similar to the one in equation (40) is obtained and solved in the same way.

As reported in [11], it is possible to improve the model considering the compressibility of the fluid considering the change of the bulk modulus. In this work, due to the low value of pressure obtained, no dependency of the bulk modulus with pressure was considered. The only effect of compressibility considered is the presence of air bubbles in the lubricant due to the air ingestion at the ends. The model proposed in the previous chapter is integrated into the LCP formulation of the Reynolds equation. For what regards the viscosity, in this work will be considered constant with the only exception the presence of air bubbles due to air ingestion.

The last model, model D, to treat cavitation investigated in this work is based on the Elrod's cavitation algorithm and is reported in [18]. Density is considered as in equation (43) and the relative density $\bar{\rho} = \frac{\rho}{\rho_c}$ is defined. In order to separate the active region of the damper from the cavitated one, a switch function g is defined. It assumes the value of zero in the cavitation zone and one in the full-film zone.

The Reynolds equation is transformed in:

$$\frac{\partial}{\partial x}\left(\frac{Bh^3}{12\mu}g\frac{\partial\bar{\rho}}{\partial x}\right)+\frac{\partial}{\partial z}\left(\frac{Bh^3}{12\mu}g\frac{\partial\bar{\rho}}{\partial z}\right)=\frac{\partial\bar{\rho}h}{\partial t}+\frac{Reh^2}{12\omega c^2}\frac{\partial^2\bar{\rho}h}{\partial t^2} \tag{49}$$

The time derivatives are then written as circumferential derivatives using equation (21).

The equation is discretized with the finite difference technique where the terms on the left side of the equation are discretized with a second order central differencing scheme and the terms on the right with a first order backward differencing. The equation is solved iteratively with a Gauss-Seidel method taking one as initial value of the relative pressure and the switch function in the whole domain. Ones convergence for $\bar{\rho}$ is reached, the value of the switch function is updated:

$$\begin{cases} g=0 & \bar{\rho}<1 \\ g=1 & \bar{\rho}\geq 1 \end{cases} \tag{50}$$

The procedure is repeated up to when convergence is reached also for the switch function. At each iteration also the value of the Reynolds number is updated due to the change of the relative density.

A fourth, trivial model, was also developed. Equation (32) is discretized in all the points of the domain, see Fig. 2-6 as reference:

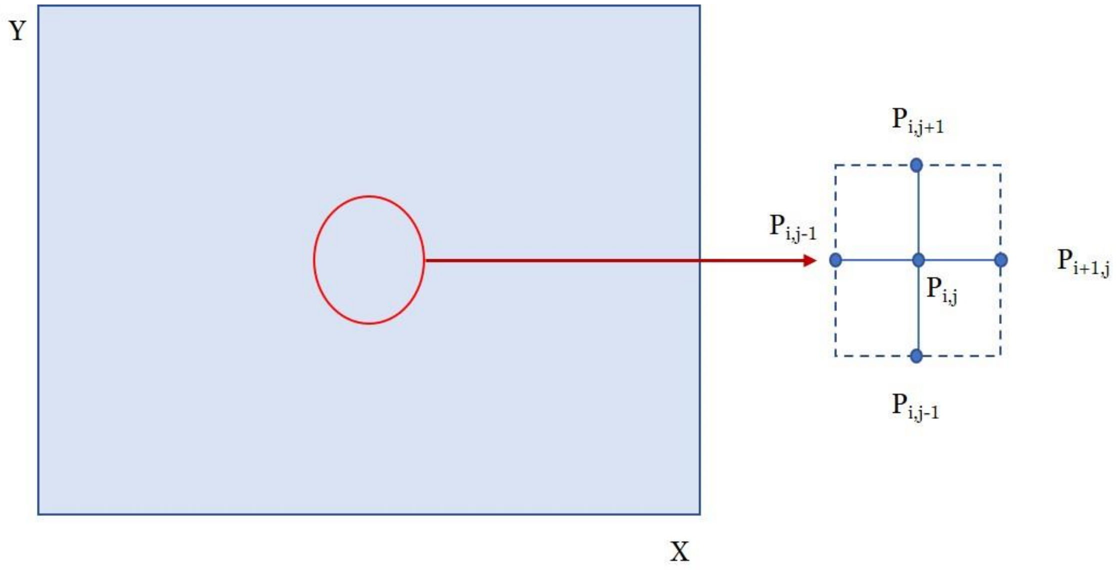

Fig. 2-6 Example of spatial discretization

A first guess solution is taken, usually constant ambient pressure on the whole domain, and, iteratively, the pressure on each point of the grid is calculated as:

$$P_{i,j}a_{i,j} + P_{i+1,j}a_{i+1,j} + P_{i-1,j}a_{i-1,j} + P_{i,j+1}a_{i,j+1} + P_{i,j-1}a_{i,j-1} = f_0 \tag{51}$$

If the new pressure calculated is lower than the cavitation pressure, in that grid point it is set equal to P_v. The procedure is continued up to when a certain tolerance is reached.

2.5. Geometry

The damper has a cylindrical geometry that is flattened out in a 2D plane where the x coordinate will correspond to the circumferential evolution and the z coordinate will correspond to the axial evolution of the damper. The final geometry is:

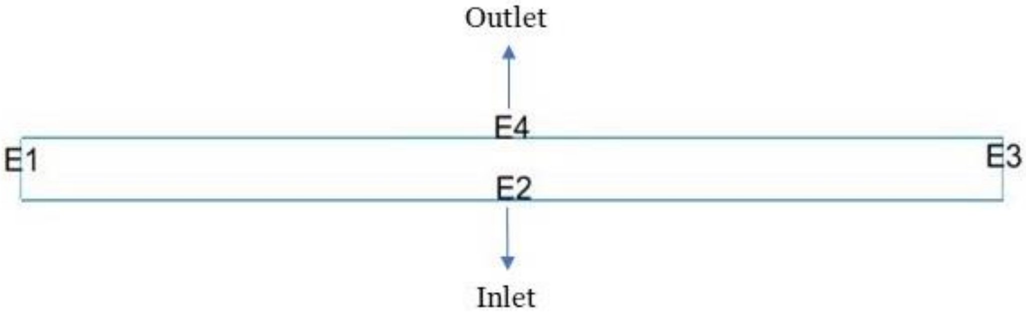

Fig. 2-7 2-D geometry of the damper

The edges are numerated so to assign the correct boundary condition to each one of them. Edge number 2 corresponds to the inlet, edge number 4 corresponds to the outlet and edges 1 and 3 are generated when the cylinder is cut and opened on a 2D plane.

For what regards the axial evolution, the shape of the damper will change whether it is composed by inlet/outlet grooves or just by the main land. Some examples:

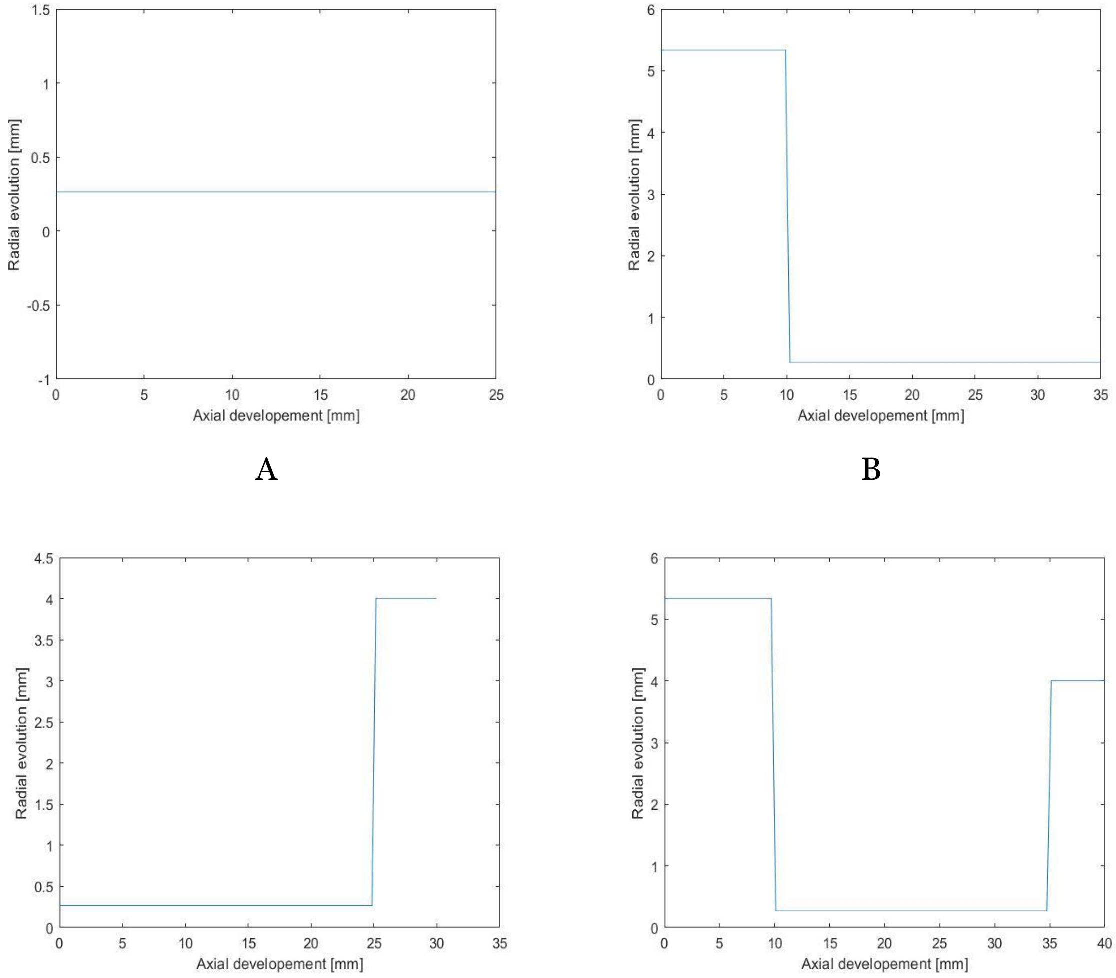

A B

C D

Fig. 2-8 Examples of possible radial geometries for half of the damper: A) only main land, B) inlet groove and land, C) land and outlet groove, D) inlet groove, land and outlet groove

2.6. Boundary conditions

2.6.1. Inlet

For what regards the inlet there are different type of boundary conditions. If the symmetry of the damper is considered and no inlet groove is present, the boundary condition (BC) that represents symmetry, as in [42] and [43], is:

$$\left.\frac{\partial P}{\partial y}\right|_{inlet} = 0 \tag{52}$$

In this case the presence of the feeding system is completely neglected.

If the damper is equipped with an inlet groove, historically the inlet BC was considered to be as in [42] and [43]:

$$P_{inlet} = P_{supply} \tag{53}$$

As mentioned before, the unsuitability of this assumption was proved experimentally. The inlet groove does not act as a perfectly separating sink between two lands of the damper where the pressure remains constant and equal to the supply one. On the contrary relevant levels of dynamic pressure were measured and a more appropriate BC would consist in a flow rate balance between the supply flow rate, the flow that exits the groove to enter the land and the change of the volume of the groove due to the shaft movement, see [44], [45]. Unfortunately, in both references, the hypothesis of short bearing is done so it cannot be applied to this model. As boundary condition if the central groove is present it can be considered a constant axial flow rate around the circumference that can be expressed as:

$$\frac{Q_{inlet}}{\pi D} = -\frac{h^3}{12\mu}\frac{\partial P}{\partial y} \tag{54}$$

However also this case is considered a simplification. The best approach is to fully consider the feeding orifices. In order to take into consideration the effect of feeding orifices, the BC represented by equation (52) must be corrected. As stated in [42] and [46], the inlet flow rate is imposed and if the flow is considered to be laminar, hypothesis more than acceptable considering the typical values of the Reynolds number, especially if the orifices are not applied on a groove. The following BC can be adopted:

$$Q_{inlet} = C_i\left(P_{supply} - P(x_h, z_h)\right)\left[\frac{m^3}{s}\right] \tag{55}$$

Where $P(x_h, y_h)$ is the pressure of the oil at the hole location and C_i is a coefficient that includes the orifice area and flow coefficient. In a 3-D model this flow rate would be directed radially but, since this model is planar, it will be considered to be axial and tangential.

The circular geometry of the hole is simplified as a rectangle, see Fig. 2-9. It is supposed that the pressure is constant on the points on the boundary of the hole and equal to the value at the center. Considering that the flow from the hole is delivered both in axial and tangential direction, the whole geometry of the damper is simulated.

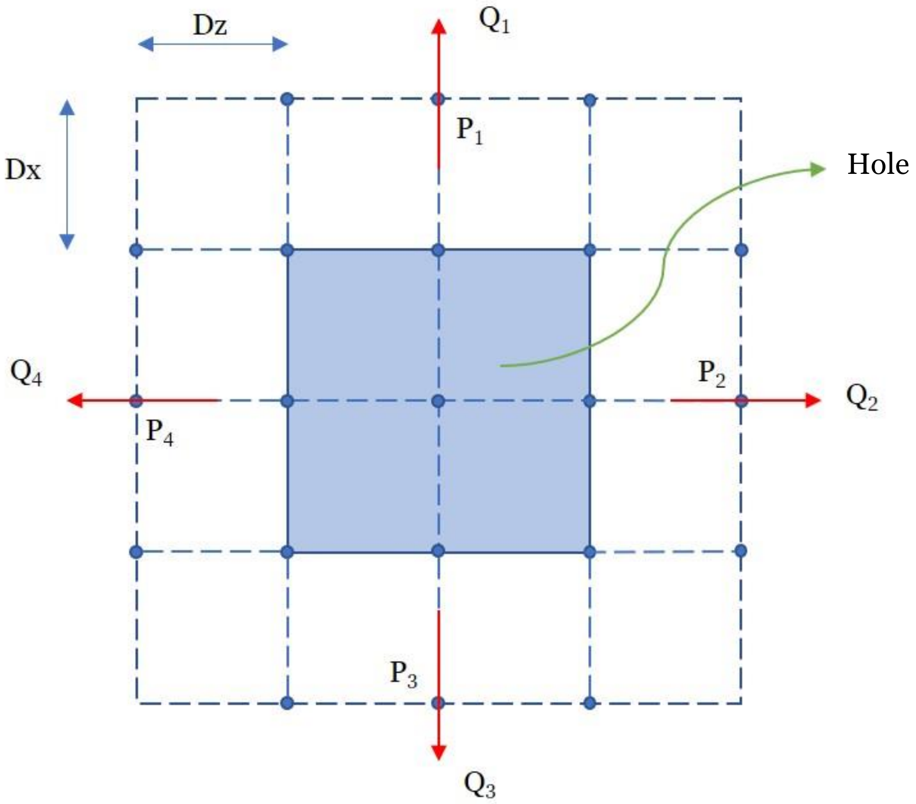

Fig. 2-9 Mesh representation for the feeding hole boundary condition

The total flow entering from the hole is the sum of the four flows delivered from the sides of the rectangle.

$$q_z = -\frac{h^3}{12\mu}\frac{\partial P}{\partial z}\left[\frac{m^2}{s}\right] \tag{56}$$

Remembering that:

$$Q_1 + Q_2 + Q_3 + Q_4 = C_i\left(P_{supply} - P(x_h, y_h)\right) \tag{57}$$

It is possible to write:

$$Q_1 = -\frac{\overline{h_1}^3}{12\mu}\left(\frac{P_1 - P(x_h, y_h)}{Dx}\right)2Dz \tag{58}$$

Where P_1 is the interpolation of the three points above the boundary of the hole and $\overline{h_1}$ is the oil film height at $\frac{Dx}{2}$ from the side of the square.

It is possible then to write similar expressions for the rest of the flow vectors.

In general, when the pressure of the oil inside the damper, in the vicinity of the feeding hole, is higher than the supply pressure, backflow happens: a flow rate of oil exiting the damper's land and entering the supply circuit. As reported in [46], in practical application, non-return valves are applied to the feeding ducts so to avoid backflows and to reduce the effect of pulsating pressure on the supply circuit. For this reason, when the presence of feeding orifices is simulated in this model, equation (57) will be used at the nodes where the orifices are located. If the pressure at the hole location is higher than the supply pressure, no boundary condition will be assigned.

2.6.2. Outlet

Edge 4 correspond to the outlet section of the damper. As reported in [7], many different boundary conditions can be assigned. In general, the damper can be exposed to ambient pressure air, in this case the BC to be assigned is:

$$P(L,t) = P_{air} \tag{59}$$

In this case the SFD is subjected to high air entrainment, that reduces the damping capacity of the device. With open ends configuration the exiting flow rate is higher, condition that will require higher inlet flow rate of oil. For this reason, the damper is usually sealed at the end. The sealing is usually not complete otherwise, due to the oil heating, the damping capacity would decrease. In the scientific literature it is possible to find many types of sealing to reduce the leakage of the damper. Some examples are given in [7]:

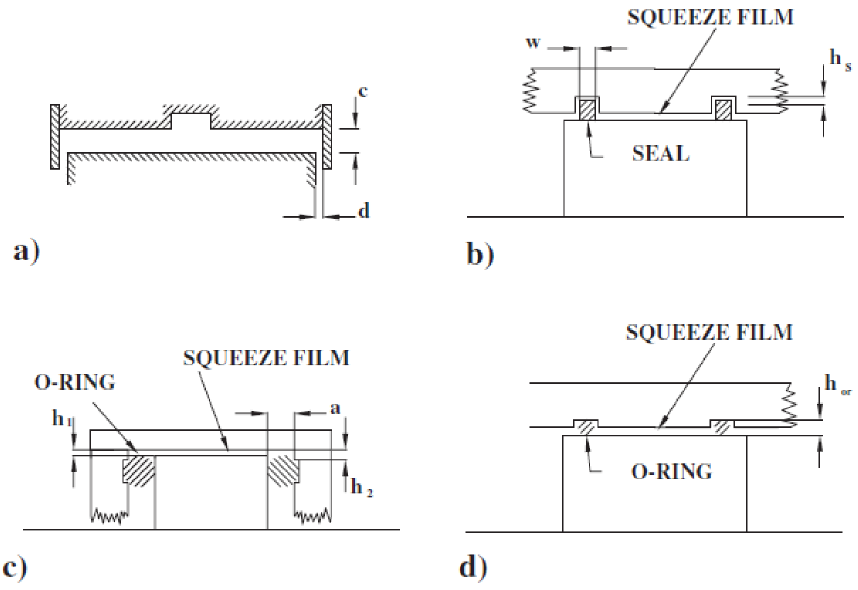

Fig. 2-10 Different types of end seal: a) small clearance seal b) piston ring seal c) O-ring seal on the side d) radial O-ring seal. From [7].

Each one of the previous configurations can be expressed with a specific boundary condition. In this work the piston ring seal and radial O-ring configuration will be taken into consideration since they are the most used in practice.

The piston ring seal represents a limitation on the outlet flow rate and it can be expressed as in [42]:

$$q_{out} = \frac{C_p(P(\theta, L) - P_{out})h_p^3}{12\mu w_p} \left[\frac{m^2}{s}\right] \tag{60}$$

Where C_p is the piston ring loss coefficient, $0 < C_p < 1$, P_{out} is the pressure outside the seal, usually ambient pressure and h_p is the piston ring radial gap and w_p is the axial dimension of the P-R.

Equation (57) is valid also for the seal so the final form of the boundary condition is:

$$\frac{h^3}{12\mu}\frac{\partial P}{\partial y}\bigg|_L + \frac{C_i P(\theta, L)h_p^3}{12\mu w_p} = \frac{C_i P_{out} h_p^3}{12\mu w_p} \tag{61}$$

The piston ring is usually made with rigid material while O-rings are made by elastomeric material. Due to its flexibility, the O-ring will deform in response of the local film pressure. The BC proposed in [42] is:

$$-h_{or}K_{or}\omega\frac{\partial P}{\partial \theta}\bigg|_L - \frac{h^3}{12\mu}\frac{\partial P}{\partial y}\bigg|_L = C_{or}(P(\vartheta, L) - P_{out}) \tag{62}$$

Where h_{or} is the o-ring thickness, K_{or} is the o-ring flexibility and C_{or} is the o-ring leakage coefficient with unit $\left[\frac{m^3}{sPa}\right]$. In this thesis the condition with the piston ring is used because it requires less parameters to be implemented.

2.6.3. Circumferential periodicity

Edge 3 and 1 are generated when the cylinder is cut in half to obtain the planar geometry, they are not a real boundary. In order to maintain the continuity, the pressure and the gradient of pressure along the axial direction must be equal on both sides. The boundary condition used is:

$$P(0, t) = P(2\pi, t) \tag{63}$$

The condition on the gradient will not be given because, as shown in the next chapter, the assignment of equation (63) will be sufficient for circumferential periodicity. It was also noted, during some simulations, that the assignment of a boundary condition on the pressure gradient along the axial direction does not improve, and sometimes even worsen, the results of the simulation itself.

2.7. Mesh

For the finite difference discretization a structured mesh, made by square elements, is used as spatial discretization. For example:

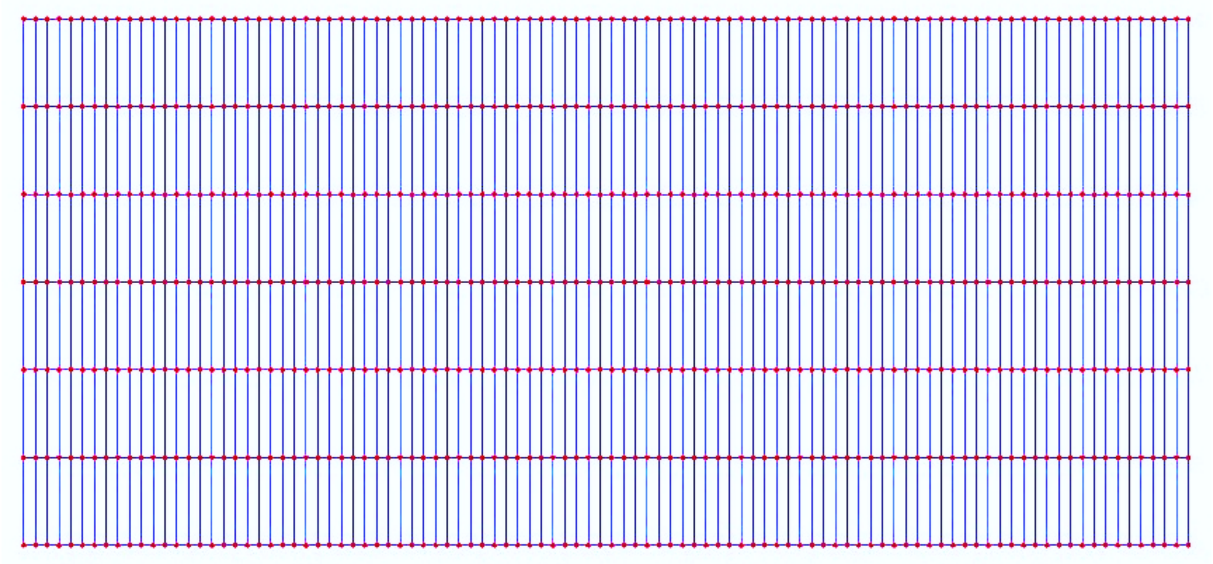

Fig. 2-11 Example of structured mesh

Different levels of mesh refinement are tested in order to assess grid independency and to find the best compromise between accuracy in the final results and computational time. In case of axial discontinuities in the clearance, it is possible to easily refine locally the mesh so to avoid numerical issues.

2.8. Forces and force coefficients

Once the geometry and the mesh are defined and the boundary conditions are assigned, the application integrates the Reynolds equation and the pressure distribution is obtained. In order to obtain the forces acting on the shaft, the pressure profile is integrated along the circumferential and axial direction:

$$\begin{bmatrix} F_x \\ F_y \end{bmatrix} = -\int_0^L \int_0^{2\pi} P(\theta, z, t) \begin{bmatrix} \cos\theta \\ \sin\theta \end{bmatrix} R \, d\theta dy \tag{64}$$

If half of the damper is simulated the actual forces are twice as the one calculated in equation (64). Starting from the forces obtained in the x and y directions and with a simple geometrical transformation it is possible to obtain the tangential and radial forces, applied on the shaft in the point where the oil thickness is the minimum.

Once the forces are known it is then possible to calculate the force coefficients. As reported in many sources, [8] and [13], the damper itself does not generate any kind of stiffness because, without the journal spinning, no pressure is generated at a given static displacement if there is no precession. The damper forces are represented in linearized form:

$$\begin{bmatrix} F_x \\ F_y \end{bmatrix} = -\begin{bmatrix} C_{xx} & C_{xy} \\ C_{yx} & C_{yy} \end{bmatrix} \begin{bmatrix} v_x \\ v_y \end{bmatrix} - \begin{bmatrix} M_{xx} & M_{xy} \\ M_{yx} & M_{yy} \end{bmatrix} \begin{bmatrix} a_x \\ a_y \end{bmatrix} \tag{65}$$

Where $v_x$and v_y are the instantaneous journal velocities and a_x, a_y are the instantaneous journal accelerations.

Damping and added mass coefficients along the x and y directions are typical of small shaft displacement around the static equilibrium position. In case of circular centered orbits, the damper generates a constant reaction film force in a relative frame rotating with frequency ω. The expression that is commonly used is:

$$\begin{bmatrix} F_r \\ F_t \end{bmatrix} = -\begin{bmatrix} 0 & C_{rt} \\ 0 & C_{tt} \end{bmatrix}\begin{bmatrix} v_r \\ v_t \end{bmatrix} - \begin{bmatrix} M_{rr} & 0 \\ M_{tr} & 0 \end{bmatrix}\begin{bmatrix} a_r \\ a_t \end{bmatrix} \tag{66}$$

Where $v_t = e\omega$ and $a_r = -e\omega^2$ while, if the orbit frequency is constant, the other two components are null.

In most rotordynamic applications, linearized force coefficients are considered. They represent changes in bearing reaction forces to infinitesimal amplitude motions about an equilibrium position. For example:

$$K_{XX} = -\left.\frac{\partial F_x}{\partial x}\right|_{(x_0,y_0)} \tag{67}$$

$$C_{XY} = -\left.\frac{\partial F_x}{\partial \dot{y}}\right|_{(x_0,y_0)} \tag{68}$$

$$M_{YX} = -\left.\frac{\partial F_y}{\partial \ddot{x}}\right|_{(x_0,y_0)} \tag{69}$$

As the definition states, these coefficients are applicable only in case of small motions around an equilibrium positions. In SFDs the orbit radius can go to half the clearance, defining an orbit far from being close to the equilibrium position, violating the main hypothesis behind expressions (67), (68) and (69). For this reason, in this work an orbit-based model, like the one proposed in [22], is adopted in this work. The counter-clockwise CCO of the damper is divided into points where the forces are evaluated. The equation of motion is then written in the frequency domain applying the Fourier transform to both the orbit points and the forces:

$$\begin{bmatrix} F_x(\Omega) \\ F_y(\Omega) \end{bmatrix} = -\left(i\Omega\begin{bmatrix} C_{xx} & C_{xy} \\ C_{yx} & C_{yy} \end{bmatrix} - \Omega^2\begin{bmatrix} M_{xx} & M_{xy} \\ M_{yx} & M_{yy} \end{bmatrix}\right)\begin{bmatrix} X(\Omega) \\ Y(\Omega) \end{bmatrix} \tag{70}$$

Equation (70) can be re-written as:

$$\begin{bmatrix} F_x(\Omega) \\ F_y(\Omega) \end{bmatrix} = -H(\Omega)\begin{bmatrix} X(\Omega) \\ Y(\Omega) \end{bmatrix} \tag{71}$$

Where $H(\Omega)$ is the matrix of complex stiffness.

In equation (71), four unknowns are present, the H_{ij}, but only two equations are available. For this reason, the same procedure is applied to the clockwise orbit, obtained applying a negative value of ω. So the final system to be solved is:

$$\begin{bmatrix} F_x^{cc}(\Omega) \\ F_y^{cc}(\Omega) \\ F_x^{c}(\Omega) \\ F_y^{c}(\Omega) \end{bmatrix} = -H(\Omega) \begin{bmatrix} X^{cc}(\Omega) \\ Y^{cc}(\Omega) \\ X^{c}(\Omega) \\ Y^{c}(\Omega) \end{bmatrix} \tag{72}$$

Where, the apex c stands for clockwise and the apex cc stands for counter-clockwise.

Once the matrix of complex stiffness is obtained, the single coefficients can be calculated as:

$$C_{ij} = \frac{Imag(h_{ij})}{\omega} \tag{73}$$

$$M_{ij} = -\frac{Real(h_{ij})}{\omega^2} \tag{74}$$

3. MODEL VALIDATION

3.1. Cavitation

In the previous chapter four different models to deal with cavitation were introduced. In the following pages the models are compared on a reference geometry and one of them will be chosen as the best option one according to the convergence and the speed with which a solution is achieved. In order to evaluate only the solution algorithm for the cavitation, the effect of air ingestion is not considered and the whole geometry of the damper is simulated. The boundary condition used is ambient pressure, $1e5\ Pa$, at both axial ends.

The geometry selected is the one reported in [37]:

$R = 64.8\ mm$
$L = 22.7\ mm$
$c = 0.1\ mm$
$\mu_L = 2.66\ \times 10^{-3} Pa \cdot s$
$\omega = 10000\ rpm$
$\varepsilon = 0.5$
$P_v = 1000\ Pa$

Table 3-1 Dimensions of reference damper in [37]

At first, the pressure evolution obtained, without dealing with the negative pressure zone, are shown. The results reported in Fig. 3-1, are referred to the model with the classical Reynolds equation, model A. The results in Fig. 3-2 are instead referred to the model in which the temporal inertia is taken into consideration, model B. Together with the pressure profile, the tangential pressure gradients, at the mesh lateral edges, are shown. The purpose is to establish if the condition for the tangential periodicity is legitimate or not. The shaft is placed on the negative side of the x axis and the rotation is counter-clockwise.

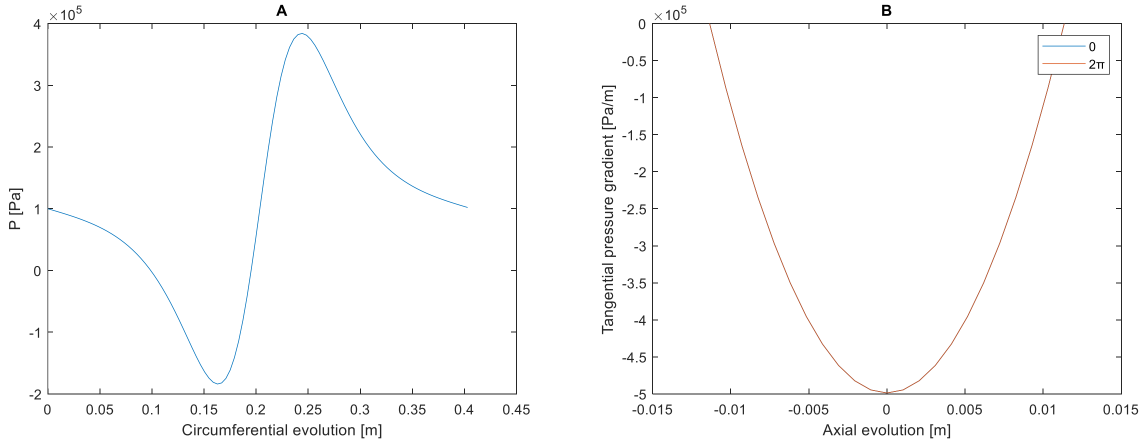

Fig. 3-1 A) Pressure evolution at mid-plane B) Circumferential pressure gradient at 0 *and* 2π. Model A

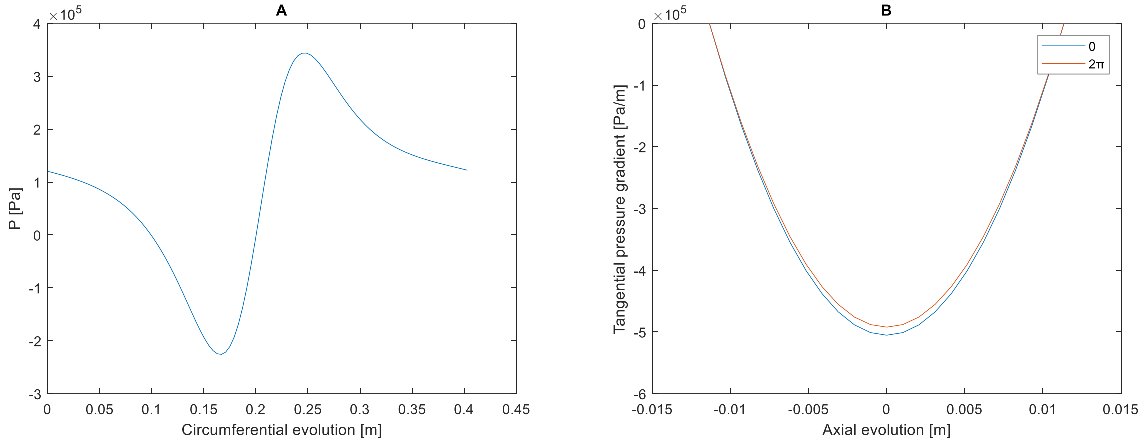

Fig. 3-2 A) Pressure evolution at mid-plane B) Circumferential pressure gradient at 0 *and* 2π. Model B

Before the discussion on the models to treat the negative pressure zone, let us focus on the effect of the Reynolds number on the pressure distribution obtained with model B. As stated in the previous chapter, when the inertia effect is added, the positive peak in pressure is usually lower and shifted to the right with respect to the one obtained with the inertia-less formulation of the Reynolds equation. The negative peak is increased, in absolute value, when the inertia effect is considered. Now the density of the liquid is taken as 870 $[\frac{Kg}{m^3}]$ and so $Re = 3.425$.

If the Reynolds number is increased, for example considering twice and three times the density, just as a comparison, Fig. 3-3 is obtained.

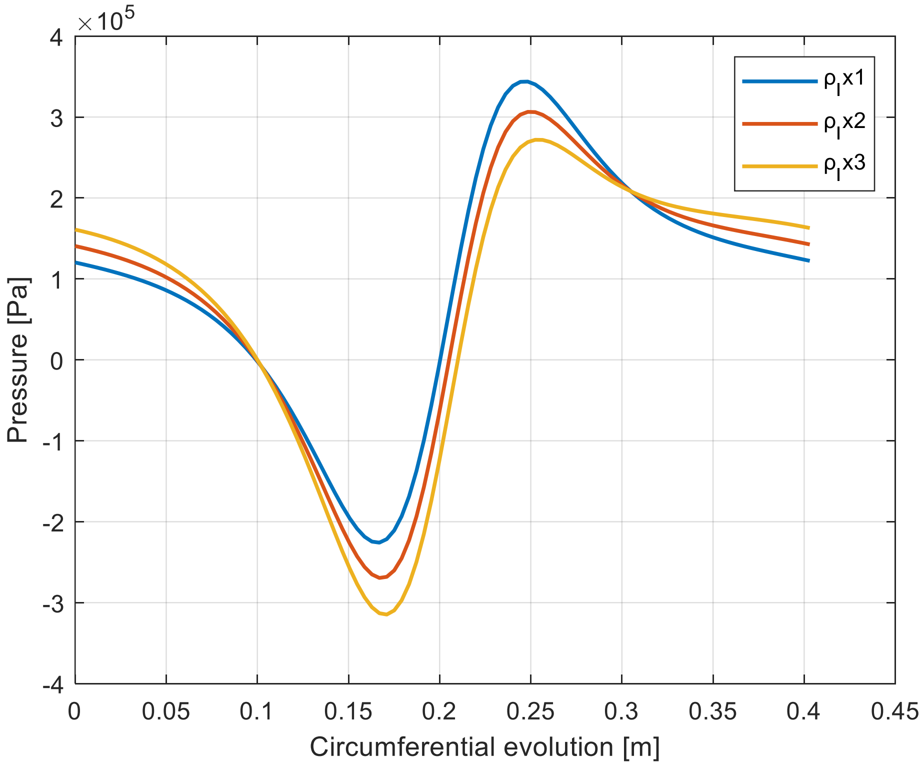

Fig. 3-3 Pressure evolution with different values of density

In Fig. 3-3, we can appreciate the change in the pressure evolution due to the increase of the Reynolds number, indication of the weight of the inertial term. The positive pressure zone is flattened out and the positive peak is reduced while the negative peak is increased in magnitude. This effect will be strongly evident in the pressure evolution inside grooves where the clearance is typically one order of magnitude higher than the one in the main lands, comporting a stronger influence of the inertial term.

For what regards the first model, model C.1, taken from [10], without the inertia term see Fig. 3-4 and Fig. 3-5 for what regards the result with the inertial contribution. Unfortunately, even with the iterative update of the Reynolds number, it is not possible to completely eliminate the peak in the pressure profile, formed in the transition zone between the cavitated and uncavitated section of the damper. For this reason this model will not be adopted.

The results obtained for the second model, model C.2, the one extracted from [12], are shown in Fig. 3-6 for what regard the expression without the inertial term and, Fig. 3-7, for what regards the expression that takes into consideration the effect of temporal inertia. The standard pressure distribution for the model C.1 and C.2 are almost identical. From a comparison between the pressure profile with the negative pressure and the one obtained with model C.1 and C.2, see Fig. 3-8, it is possible to notice that the region that assumes the vapor pressure, due to the LCP algorithm, is larger than the negative pressure zone. The positive peak is slightly shifted to the left and is 6% higher in value.

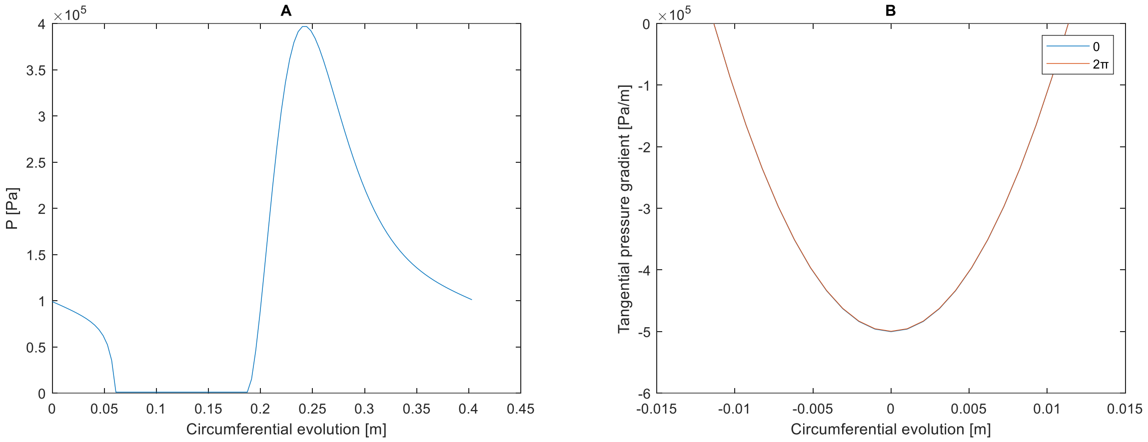

Fig. 3-4 A) Pressure distribution at mid-plane B) Circumferential pressure gradient at 0 and 2π. Model C.1 without inertia

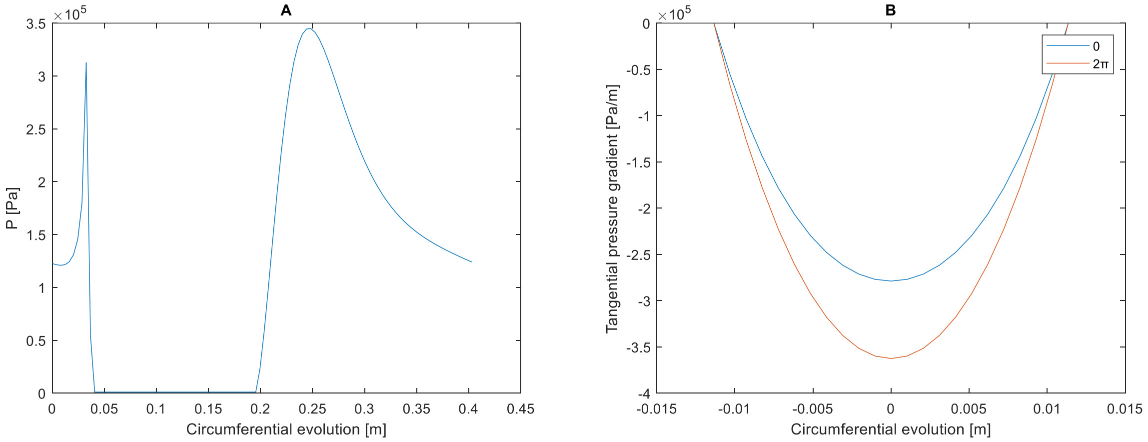

Fig. 3-5 A) Pressure distribution at mid-plane B) Circumferential pressure gradient at 0 and 2π. Model C.1 with inertia

Unfortunately, for both model C.1 and model C.2, it was not possible to smooth the pressure peak in the transition zone in the case of the inertial term addition. Different discretization schemes were tested for the second order derivative but, unfortunately, none of them brought any improvement. It must be considered that these two models were developed for oil film bearings. In that application the inertia term is not present. The author assumes the presence of a numerical issue, brought by the second derivative term, responsible for the bad results obtained. In order to solve this problem, the numerical and mathematical issues of the linear complementarity must be studied more deeply.

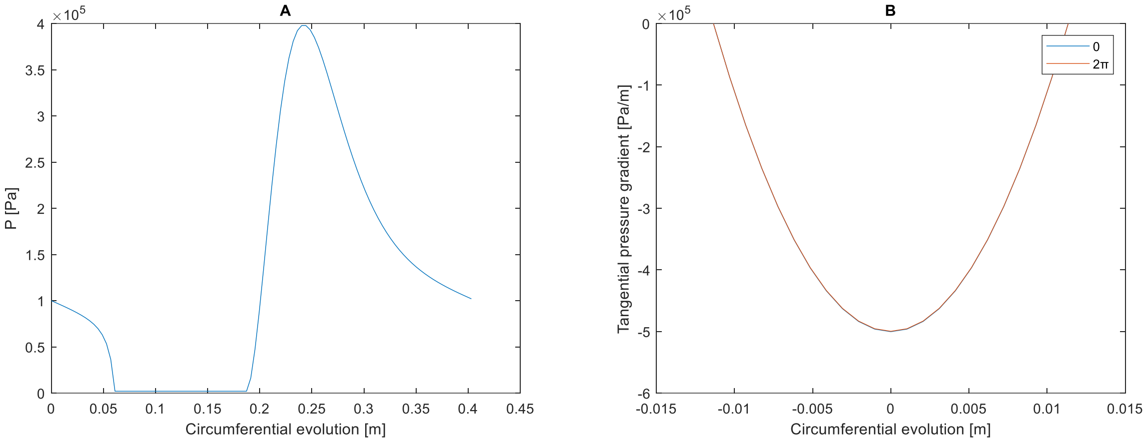

Fig. 3-6 A) Pressure distribution at mid-plane B) Circumferential pressure gradient at 0 and 2π. Model C.2 without inertia

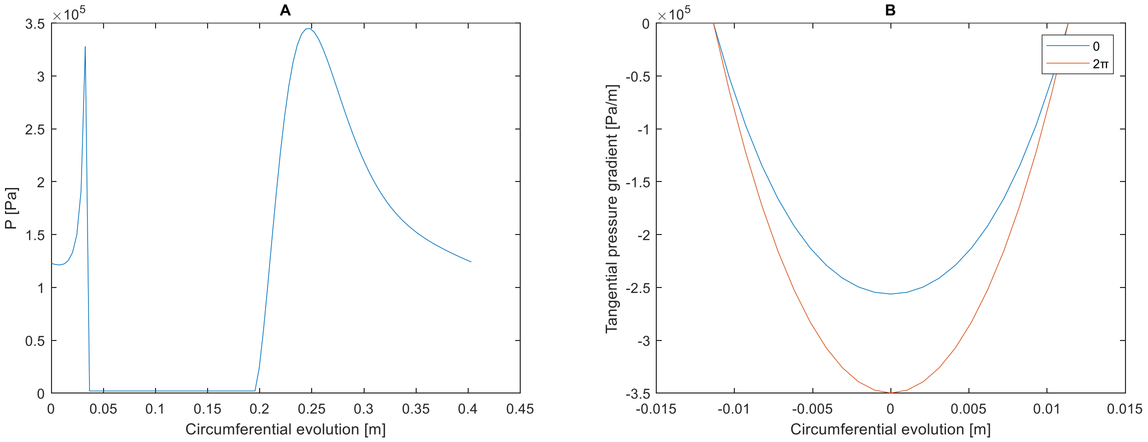

Fig. 3-7 A) Pressure distribution at mid-plane B) Circumferential pressure gradient at 0 and 2π. Model C.2 with inertia

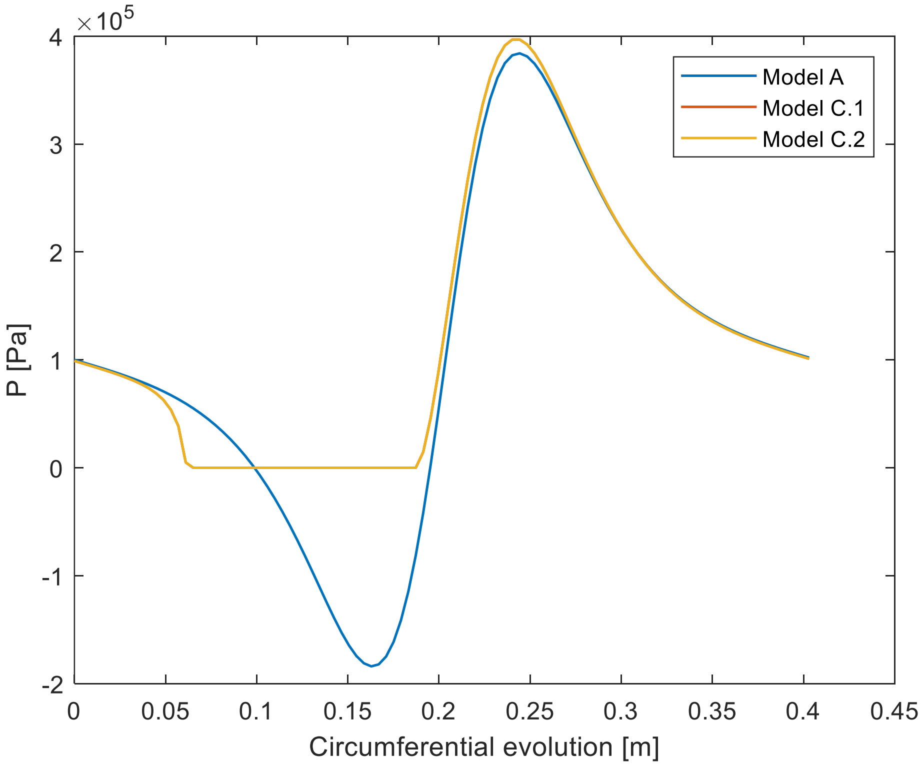

Fig. 3-8 Comparison between pressure obtained with model A, with model C.1 and with model C.2. No inertial term.

Also model D, the one based on the Elrod's cavitation algorithm, was tested with the SFD geometry proposed in [45]. The algorithm elaborated resulted slow and inefficient in the evaluation of the zone of negative pressure. The inclusion of the inertial term compromised even more the rate of convergence of the numerical tool and in some cases, the method lost its stability. Also San Andres, in [48], proposes a similar approach for dealing with cavitation and reports that, the 2-D generalization and the introduction of other terms may compromise the code stability. For these reasons, also this model is not considered suitable and the results obtained are not shown.

In Fig. 3-9 and Fig. 3-10 the results obtained with the model E are presented. The pressure distributions obtained, both for the case with and without the inertia consideration, are very similar to the results obtained without treating the negative pressure. Of course in the region where cavitation happens, the algorithm developed, is able to bring the pressure to the vapor pressure value. In Fig. 3-11, the visualization of the different pressure profiles is displayed. For what regards the model without the inertial term, it is possible to see that the area where the pressure is put to the vapor pressure value is similar in extension to the negative pressure region of the standard result, model A. The rest of the pressure evolution is not affected. For this reason, this model, cannot be considered the actual representation of what is happening. However, due to the impossibility to obtain a smooth pressure evolution with the LCP models in presence of inertia, the error introduced by the model E will be considered acceptable. Model E is also faster than both the LCP models and easier to integrate with the air ingestion model, model F. Considering all the positive aspects, the model E will be taken as the reference one to be used in case of cavitation.

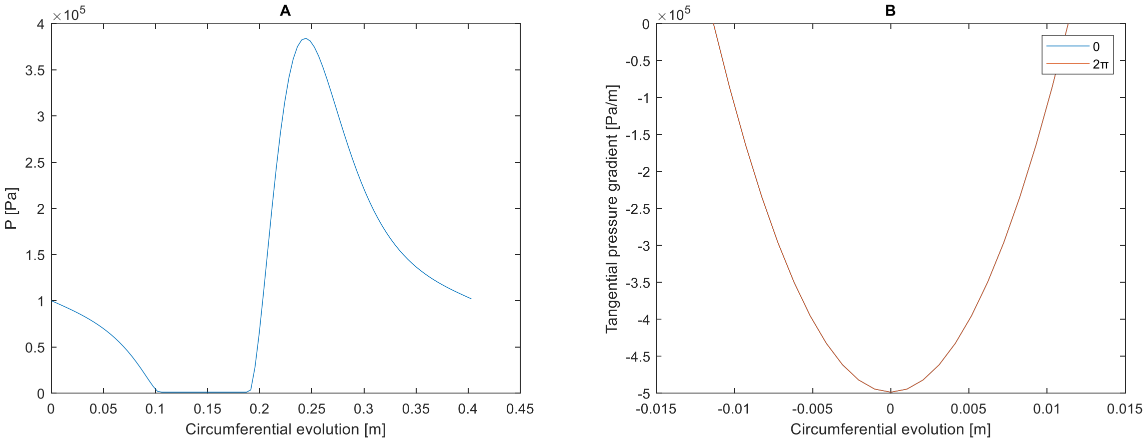

Fig. 3-9 A) Pressure evolution at mid-plane B) Circumferential pressure gradient at 0 and 2π. Model E without inertia

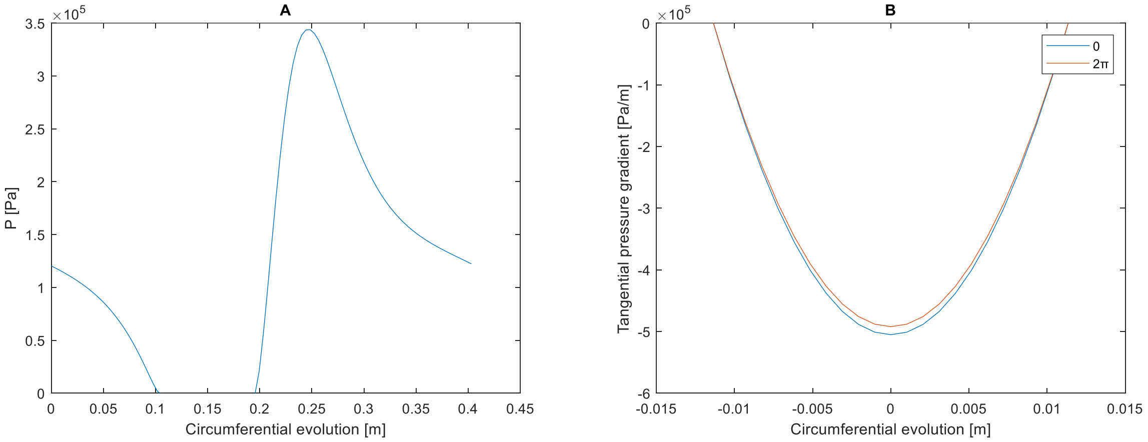

Fig. 3-10 A) Pressure evolution at mid-plane B) Circumferential pressure gradient at 0 and 2π. Model E with inertia

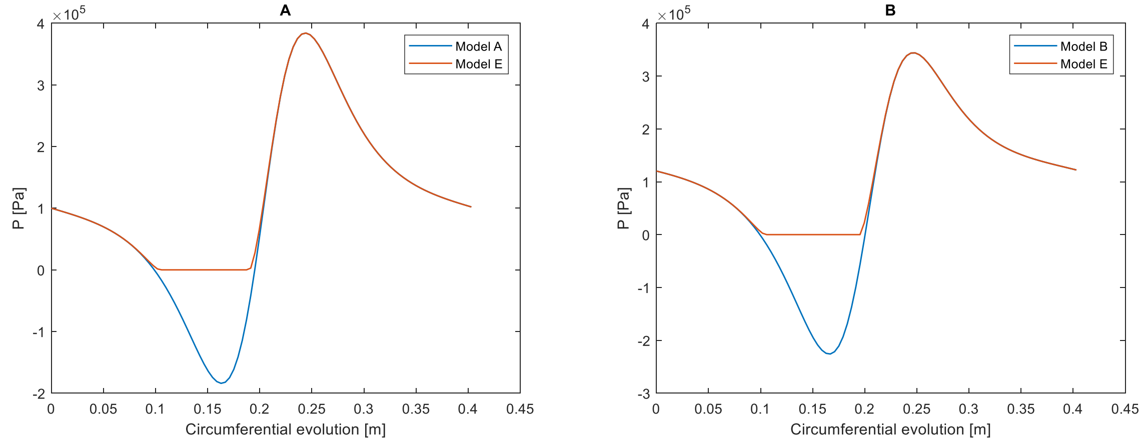

Fig. 3-11 Comparison between pressure evolution obtained from model A and model E without inertia (A) and with inertia (B)

3.2. Air ingestion

As mentioned before, the model developed in this work, used to evaluate the effect of the air ingestion in the lubricant, is based on the work shown by Diaz and San Andres in [30] and the considerations presented in [31]. At first, the same model proposed in the previous references was investigated. The geometry tested is summarized in Table 3-2.

$R = 64.7\ [mm]$
$L = 31.1\ [mm]$
$c = 0.343\ [mm]$
$\mu_L = 0.0775\ [Pa \cdot s]$
$\rho_L = 870\ \left[\frac{Kg}{m^3}\right]$
$\omega = 500\ [rpm]$
$\varepsilon = 0.18\ [mm]$

Table 3-2 Geometry and oil properties of damper studied in [30]

In Fig. 3-12 the test rig used in [30] and [31] is shown.

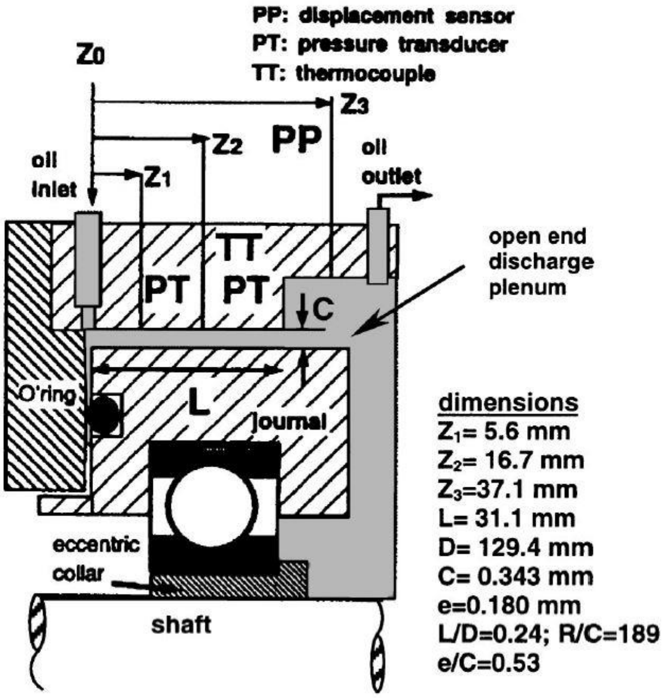

Fig. 3-12 Test-rig representation from [30]

The reference air volume fraction is varied from 0 to 0.6, as boundary conditions, zero gradient will be considered at the left side of the damper and a constant pressure of 1.8 bar will be considered at the right end, the vapor pressure is 10 Pa. The peak-to-peak pressure, radial and tangential forces are evaluated at two axial positions: $Z_1 = 5.6\ [mm]$ and $Z_2 = 16.7\ [mm]$.

As we can see from the following figures, the increase of air content in the lubricant, tends to flatten the pressure evolution and the peaks are shifted to the right: see Fig. 3-13:

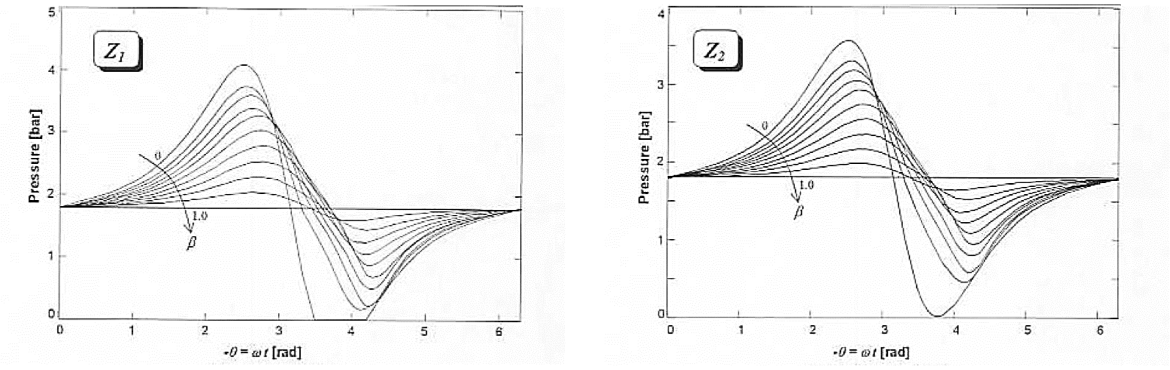

A B

Fig. 3-13 Pressure evolution at axial position Z_1 and Z_2, from [29]

The same graphs, replicating the model are obtained:

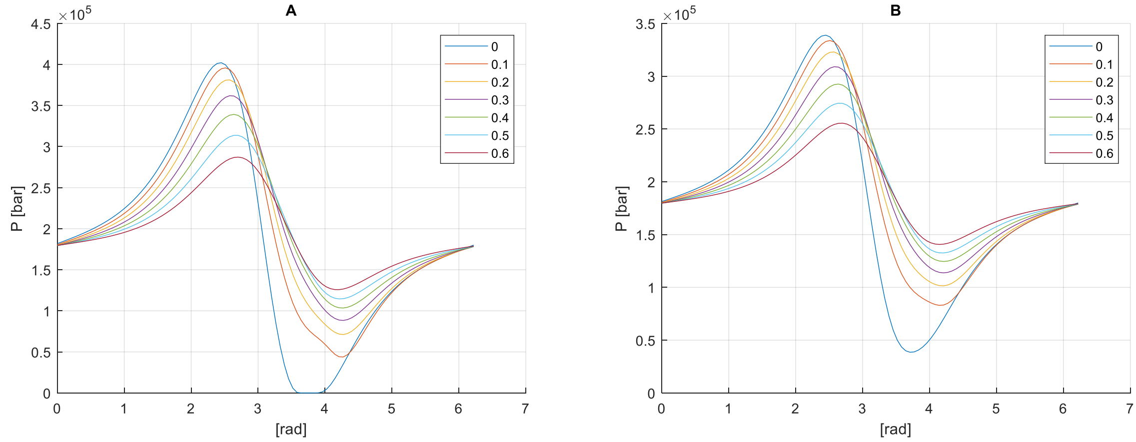

Fig. 3-14 A) Pressure evolution at Z_1, B) Pressure evolution at Z_2. Standard model.

The model works but the reciprocating frequency considered is rather small. In order to establish if the model is reliable, the same damper was tested with higher frequencies. Unfortunately the model is not able to produce realistic results when the frequency becomes three or four times higher than 500 rpm. The reason of the behavior of the model is not known but it is possible to assume that when the frequency is increased, the area of negative pressure is larger and for low values of ingested air, pressure oscillations are registered in this area, probably due to the high circumferential pressure gradients.

For this reason the air ingestion model has been integrated in the iterative model for the resolution of the negative pressure zone. In order to couple the models, the density and viscosity of the fluid are calculated as reported in equation (9) and (10).

The pressure evolution obtained with the new hybrid model is:

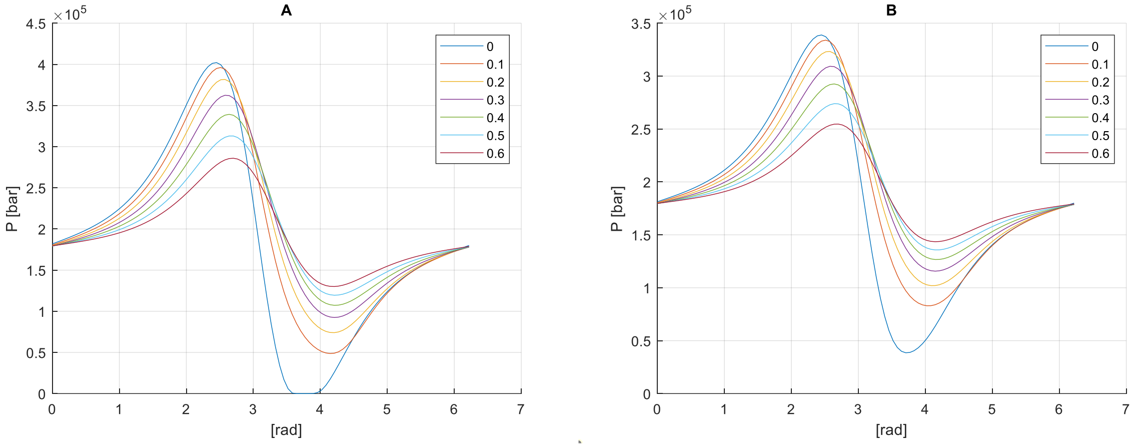

Fig. 3-15 A) Pressure evolution at Z_1, B) Pressure evolution at Z_2. LCP plus air ingestion model

In [29], the author shows some comparison graphs between the numerically calculated peak-to-peak pressure, tangential and radial forces against the experimentally derived values, for the whole range of β_0. In Fig. 3-16 the value of the peak-to-peak pressure, at the two axial positions, are reported. The values refer to the experimental results and numerical results obtained by Diaz and the numerical results obtained with the hybrid model introduced above. It is possible to appreciate the correspondence between the values obtained, the model presented in this work is able to reproduce the same results of the one found in literature for the first axial position. For the second axial position, the model proposed here slightly underestimates the experimental and numerical values proposed in [29]. The maximum discrepancy at the second axial position is around 14%.

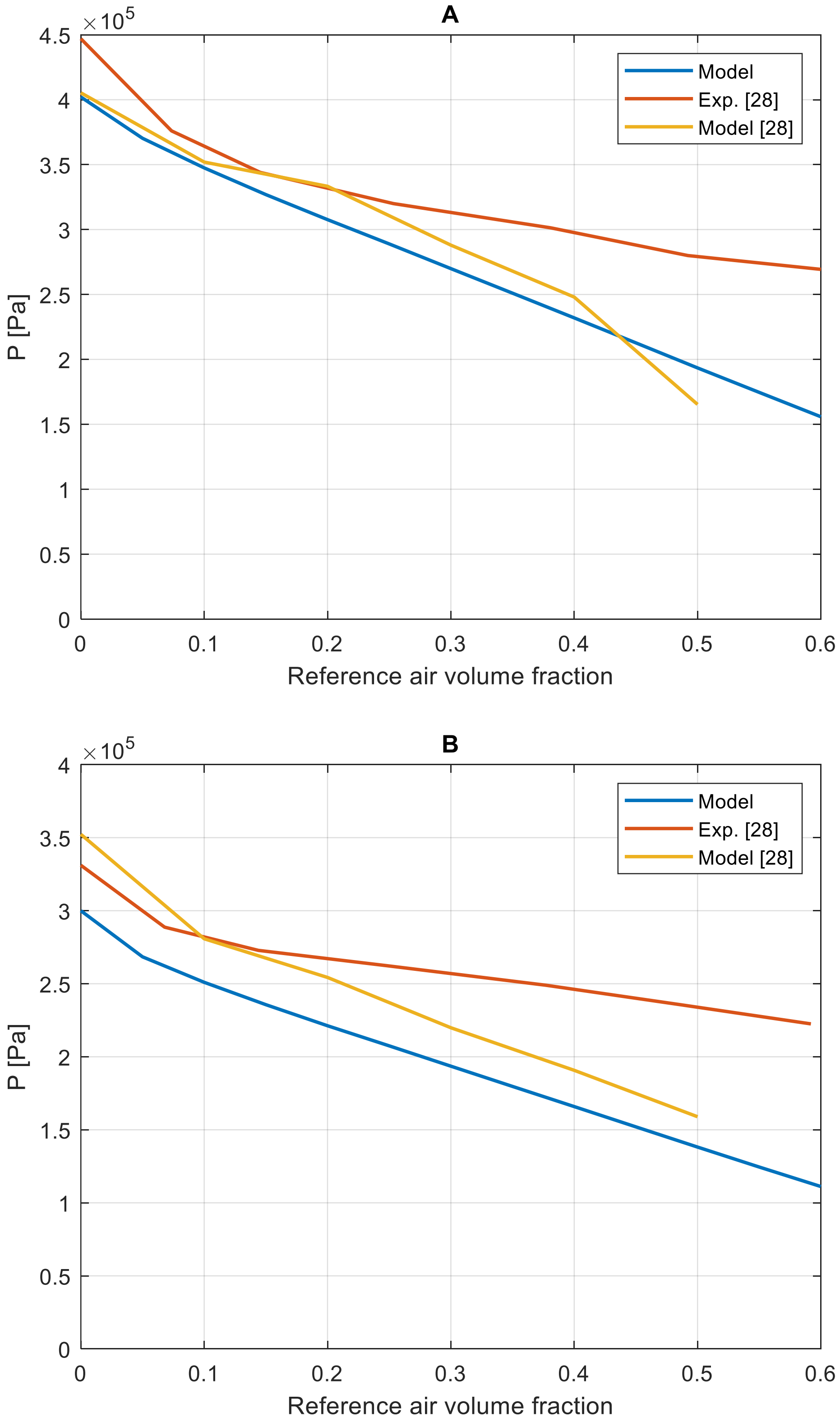

Fig. 3-16 Peak-to-peak pressure at Z_1 (A) and Z_2 (B). Results obtained with the LCP plus air ingestion model

In Fig. 3-17 the results for the tangential forces are presented. For extrapolation reasons, only the results of Diaz's model are presented. It is possible to see that at the first axial position, the results obtained with the two models are almost identical. For what regards the second axial position, the model adopted in this thesis slightly underestimates the results shown in [29]. The maximum percentual difference between the two sets of data is around 13%.

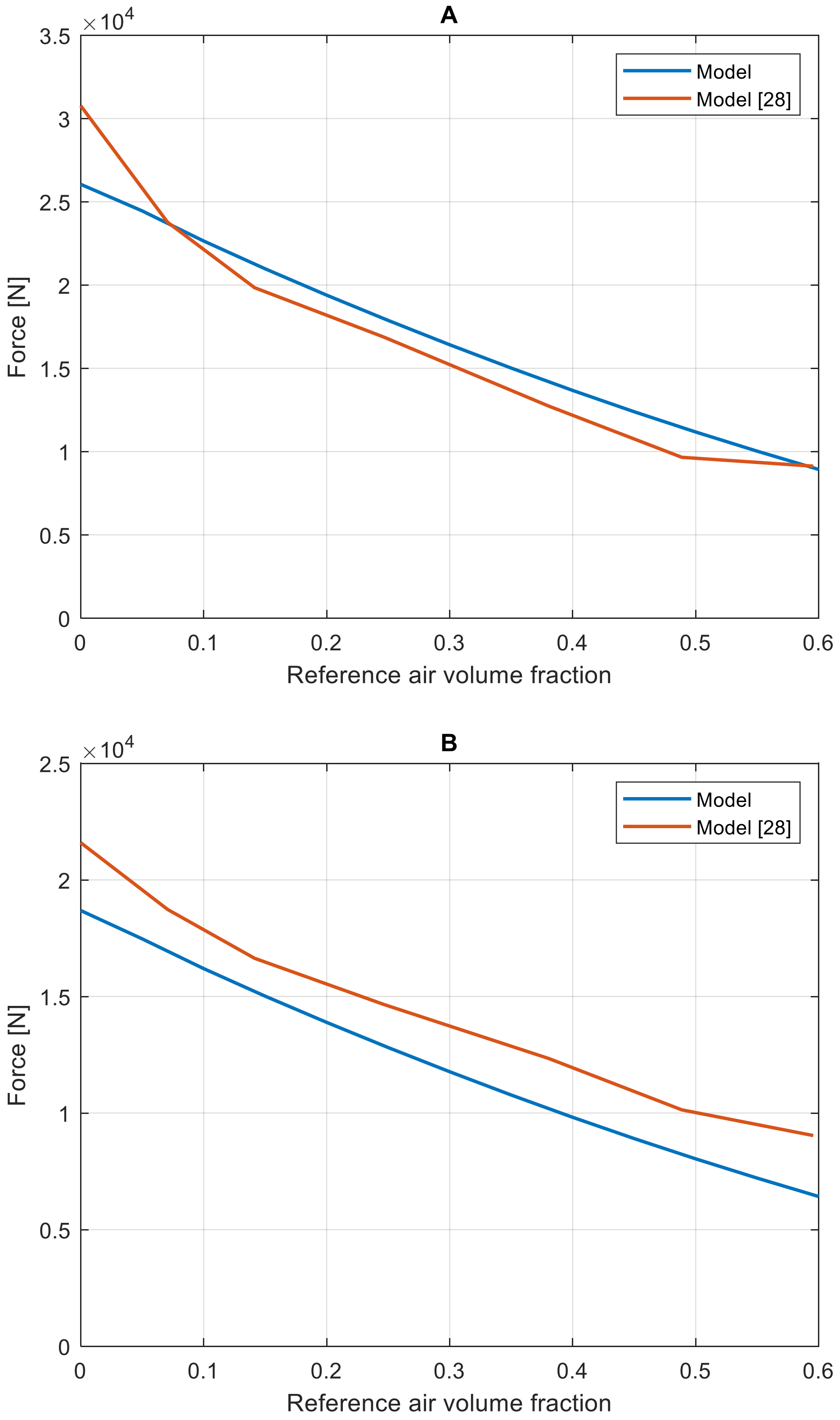

Fig. 3-17 Tangential force at Z_1 (A) and Z_2 (B). Results obtained with the LCP plus air ingestion model

In Fig. 3-18 the results obtained for the radial force are presented. In both cases, the results obtained from the hybrid model are slightly higher than the numerical results reported in the reference. Both numerical results underestimates the experimental ones. In [29], the author, proposes as an explanation the fact that the zero axial gradient boundary condition used in the model, is not able to completely describe the feeding mechanism of the damper and that a static effect, determined by the supply pressure, is left out from the modeling. The explanation seems legitimate since, the feeding oil enters in the system in a radial direction pointing towards the center of the damper. The discrepancy between the numerical results, is indeed higher at the first axial position so in the proximity of the feeding orifices.

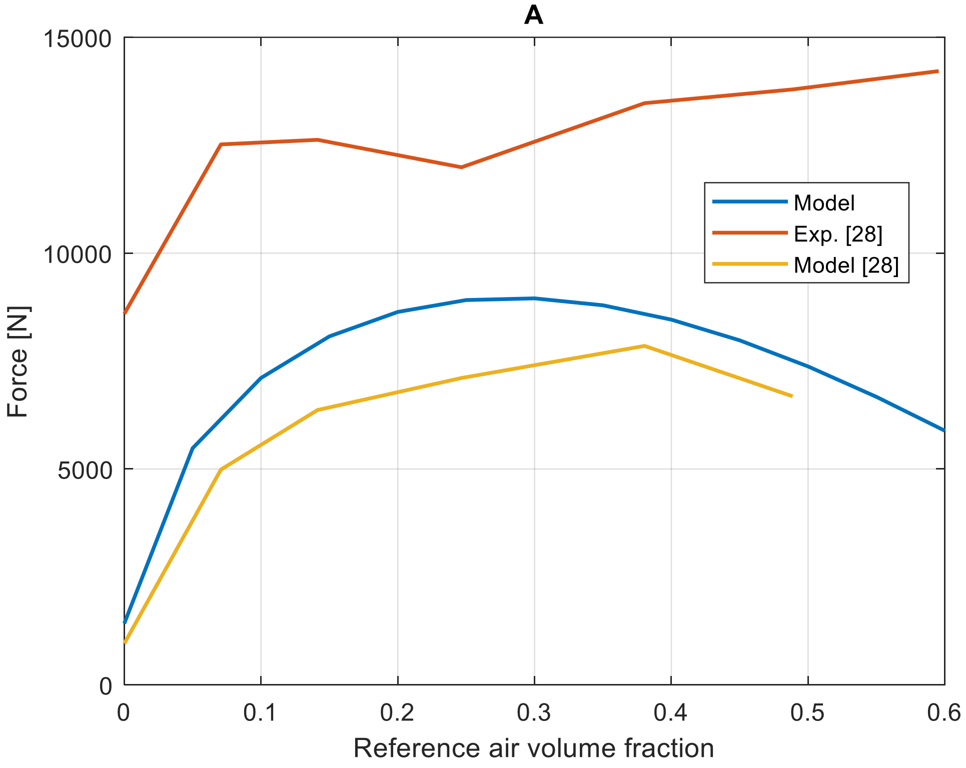

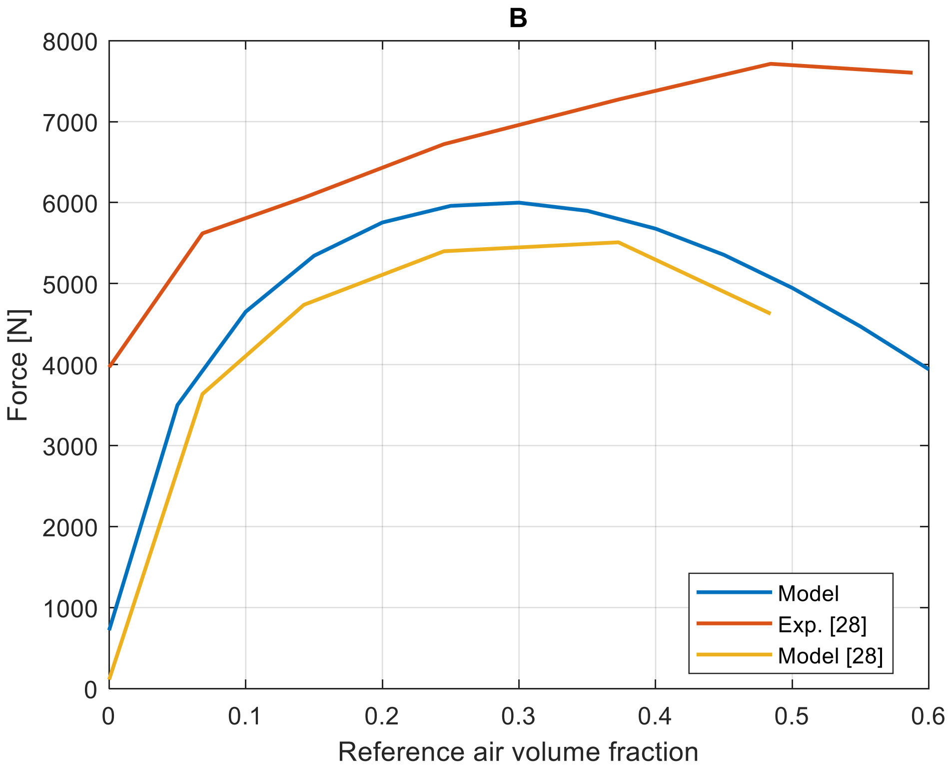

Fig. 3-18 Radial force at Z_1 *(A) and* Z_2 *(B). Results obtained with the LCP plus air ingestion model*

3.3. General validation

An important experimental investigation on squeeze film dampers was performed by San Andres and his research group in the past years, see [13]. The results of that work will be taken as reference in order to validate the model described in the previous chapter. The research group tested six different geometries, investigating the effect on the dampers' performances of the clearance, the damper length, the presence of grooves and seals and many others. For our purpose, only three configurations will be considered. The different configuration studied are:

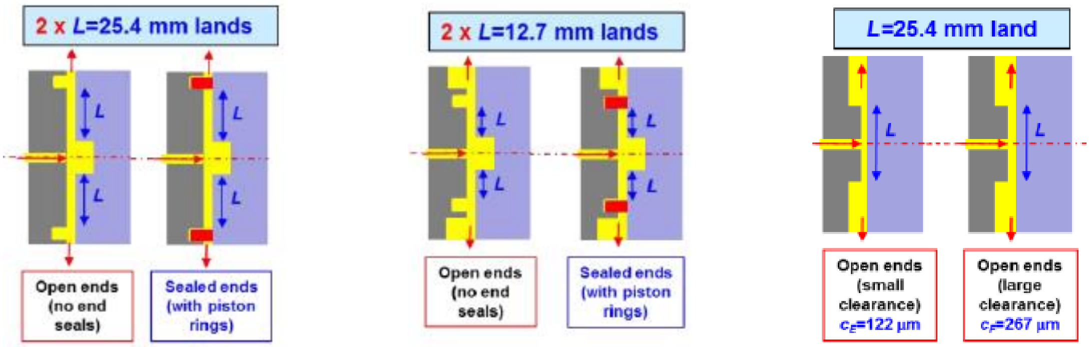

A B E, F

Fig. 3-19 Different SFDs tested in [13]

The differences between the four dampers are expressed in Table 3-3, the radius of the shaft is always $127\,mm$. The oil used is ISO VG 2 with $\rho = 805\,\frac{kg}{m^3}$ and $\mu = 2.65 \times 10^{-2}\,Pas$.

	A	B	E	F
cl	*0.141-0.251*	*0.138*	*0.122*	*0.267*
L	*2x 25.4*	*2x 12.7*	*25.4*	*25.4*
d_G	*9.5*	*9.5*	no	no
L_G	*12.5*	*12.5*	no	no
d_E	*3.5*	*3.5*	no	no
L_E	*2.5*	*2.5*	no	no
seal	yes	yes	no	no

Table 3-3 Dimensions of dampers in Fig. 3-19 Different SFDs tested in [13]

Fig. 3-19, measures in [mm]. Seals indicates the possibility to mount piston-rings at the end of the damper. Subscript G stands for inlet groove and subscript E stands for exit groove

The force coefficients obtained with the model developed previously are compared with the ones shown in [13] in order to verify if the model is reliable in the prediction of the behavior of the damper in case of different configurations.

3.3.1. Damper E,F

At first the dampers with the simplest geometries were considered for the validation of the model. The data used can be found in [13] and in [14], the thesis where the general results are presented. Both dampers are tested with centered and statically eccentric circular orbits. The results for centered orbits are considered as reference in this work. The orbit radius to damper clearance ratio considered are: 0.05, 0.14, 0.29 and 0.43. The frequencies tested are $10 \div 250\,Hz$ for damper E and $10 \div 100\,Hz$ for damper F. The geometry and frequency range generate $Re \leq 15$.

Both the SFDs can be considered as short dampers due to the low value of the length-to-diameter ratio. In [14], the author states that the values of inlet oil flow rate ($5.1\,LPM$ in damper F and $6.1\,LPM$ in damper E) and supply pressure ($1.36 \times 10^5\ Pa$ in damper F and $2.86 \times 10^5\,Pa$ in damper E) are high enough to assume that no air ingestion is verified. However, if the assumption on short-length bearing is done and the parameter γ, defined in the previous pages, is calculated, the hypothesis of no air ingestion is no more applicable. In Fig. 3-20, the values of β_0 calculated with γ and numerically, for damper F considering the maximum orbit radius, are presented:

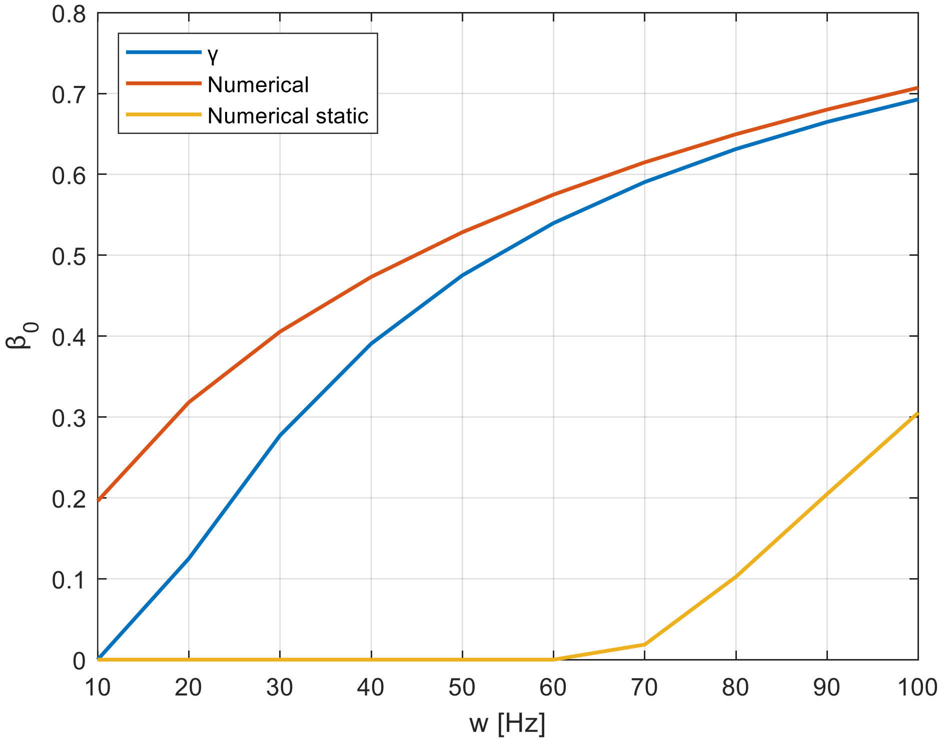

Fig. 3-20 β_0 calculated numerically and with γ

The dampers were tested considering two different boundary conditions: one without considering the inlet system and one, also reported in the reference, where a static pressure field, with the feeding pressure at the middle and the ambient pressure at the discharge, is summed to the dynamic pressure evolution. The presence of the static pressure field does not influence the force coefficients but only the evaluation of the reference air volume fraction. It is possible to see that in both cases, the reference volume fraction is far from being zero. It is possible that, at both ends of the damper, some oil is accumulated before being discharged. So, the damper is not directly in contact with air. In case of a positive axial gradient at the discharge, the external oil is sucked inside, preventing the ingestion of air and for this reason no air ingestion is registered in [14]. Since in the reference air ingestion is not considered, the same will be done here.

In Fig. 3-21, the values of the mass and damping coefficients for damper F are presented. Both coefficients are adimensionalized with values obtained from the classical lubrication theory. The results obtained experimentally and with a numerical model, shown in [14], are compared with the ones obtained with the model presented int this work It is possible to see that the results obtained numerically with both the models are the same for the mass coefficient. Unfortunately, a discrepancy between the numerical results and the experimental ones is present. In [14], for the simulation, the damper is divided in half. The pressure evolution is obtained summing a static pressure profile, obtained considering the supply pressure on one side and the ambient pressure on the other, and the dynamic pressure profile, obtained considering null axial gradient at the supply side and zero static pressure on the discharge side.

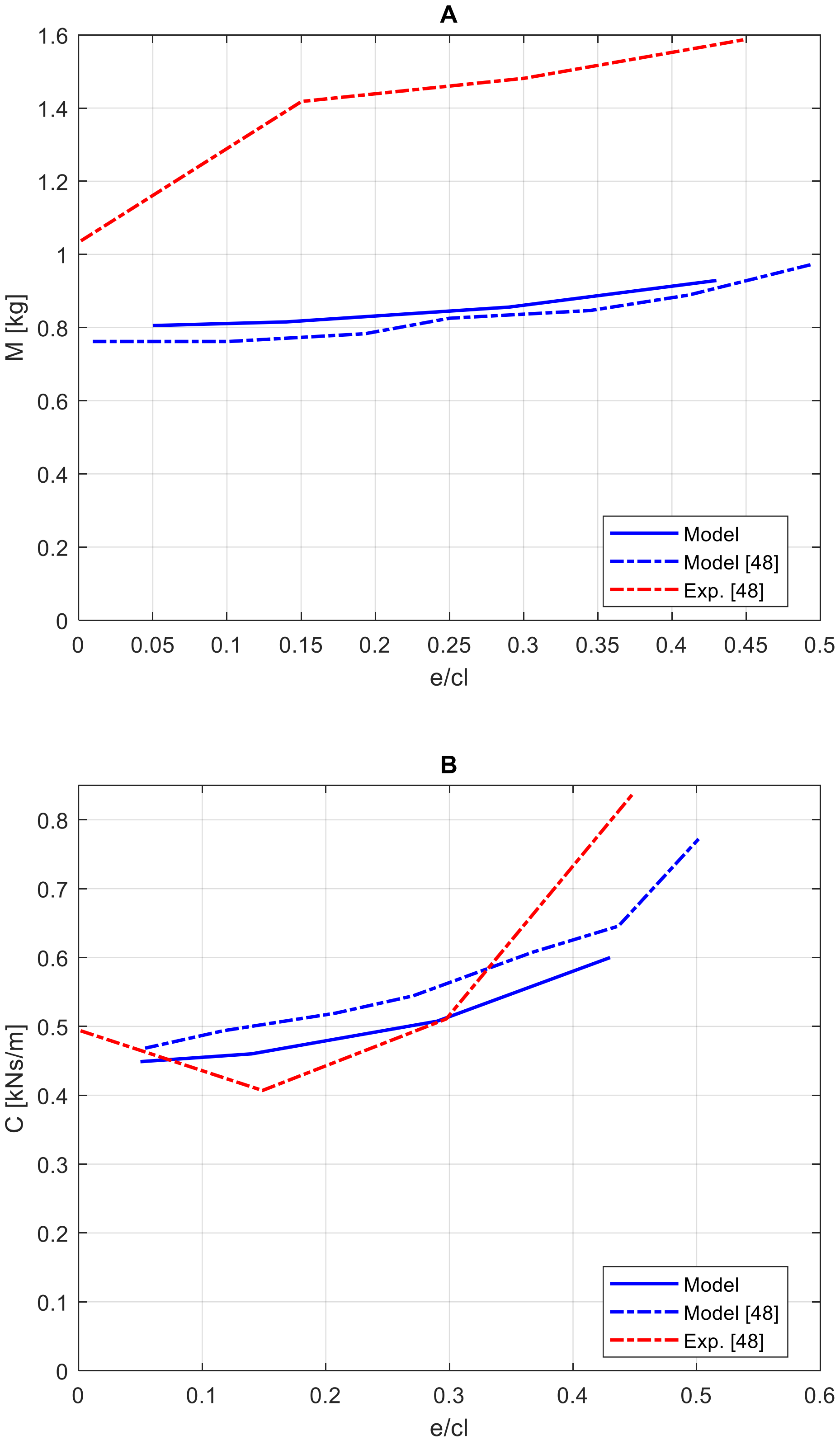

Fig. 3-21 Mass (A) and damping (B) coefficients of damper F:numerical results for model E, numerical and experimental results from [14]

One explanation for the discrepancy between the results can be attributed to the choice of the boundary conditions. Usually, the constant supply pressure at the feeding plane, is adopted to simulate dampers with feeding grooves and not dampers with feeding orifices that, instead are simulated considering null axial gradient. Also in the analysis of the other dampers, it was found that the mass coefficient is the most affected by the boundary conditions. For this reason, the model is considered valid also if the discrepancy between the reference mass coefficients and the one obtained with the model is not negligible. It is not the aim of this thesis to find the ideal boundary conditions that represent the operations of the test rig of the others research groups.

For the damping coefficients, the model proposed in [14] generates slightly higher results than the ones obtained with the model proposed in this thesis. On the other hand, the experimental results for $\frac{e}{cl} < 0.3$ are similar to the ones obtained with the model proposed in this work.

For both coefficients the trend obtained from the numerical results agrees with the trend obtained experimentally. With higher orbit radius the response of the damper is higher.

For what regards damper E, the results proposed in the reference are only the experimental ones, reported for the horizontal and vertical components. The damping coefficients, obtained numerically, are quite close to the experimental results. The maximum difference between the values is 25%. On the other hand, for the mass coefficients, the difference between the numerical and the experimental results is higher, see Fig. 3-22. A possible explanation can be found again in the boundary conditions. The inlet pressure of the oil for the damper with the lower clearance is $2.86 \times 10^5\ Pa$. In [14], a graph reports the value of the peak-to-peak dynamic pressure at the mid plane for $\frac{e}{cl} = 0.31$ and the maximum value is almost half the value of the supply pressure. Such high inlet pressure will for sure modify the shape of the pressure profile determining different values of the force coefficients.

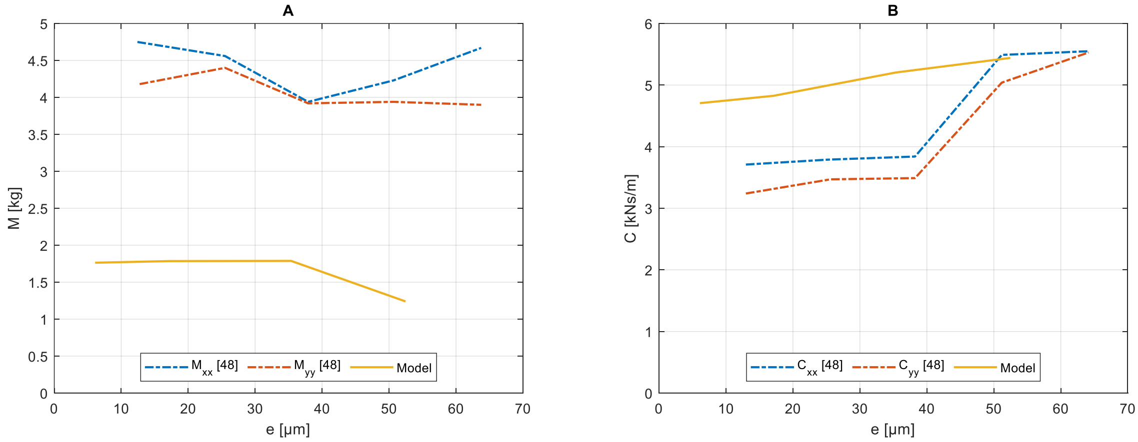

Fig. 3-22 Comparison of mass coefficient (A) and damping coefficient (B) between numerical results and experimental results from [14]

3.3.2. Damper B

For what regards damper B, the benchmark data are taken from [49], for the open ends configuration. For the sealed ends configuration, instead, the reference is [50].

The test rig used in the references is built so to guarantee that the damper is constantly submerged in oil. The goal of the researchers is to separate the effects of the groove from the air ingestion.

At first the whole damper was simulated and the results for both the damping and mass coefficients were far from the one presented in the reference. The same happened when half of the damper was simulated applying a constant pressure, equal to the supply pressure, in the groove region. For this reason the boundary condition with the orifices feeding system was tested.

As stated in the previous chapters, in the groove region the Reynolds number is higher than in the rest of the damper. A complex 3-D flow is developed in that area but only the first layers of lubricant actively work in the development of the dynamic pressure. For this reason an equivalent groove depth, usually less than ten times the land clearance, is adopted. As proposed in [20], different effective groove depths are tested and the one that produces the best correlation with the experimental results is used.

In order to evaluate if the model proposed in this thesis is able to reproduce the same results proposed in [49], the first step was to find the correct hole flow coefficient that can guarantee that, given the feeding pressure reported in the reference, the same inlet flow rate is obtained.

Then the correct value for the groove effective depth was tested. The first value used was the one proposed in the reference, $d_{ge} = 3.8cl$. The results obtained are closer to the reference ones than what it was obtained with the first two hypothesis. After some trials, the effective groove depth that guarantees the closest results to the reference ones was found: $d_{ge} = 3.5cl$. The discrepancy between the two values could stand in the differences between the two numerical models. The one adopted in [49], was developed so to be able to evaluate the interaction between the flows of lubricant at the interface between the groove and the land. Let us consider that both models are based on the two-dimensional Reynolds equation that is not able to simulate the three-dimensional flow evolution in the groove. For this reason, in both cases, the simplification of the effective groove depth is adopted.

In Fig. 3-23 it is possible to see the comparison between the mass coefficient, shown in [49], and the ones obtained with the model developed here. As it was done for the previous damper, the coefficients are adimensionalized with the values obtained with classical SFD lubrication theory. The results are obtained with circular orbits with radius equal to 10% of the clearance and for different static eccentricities. It is possible to appreciate that the discrepancy between the two sets of data is limited. In both cases the horizontal component tends to slightly increase with the static eccentricity while the vertical components behave in the opposite way. For the centered orbit case the model proposed in this work slightly underestimates the results shown in the reference.

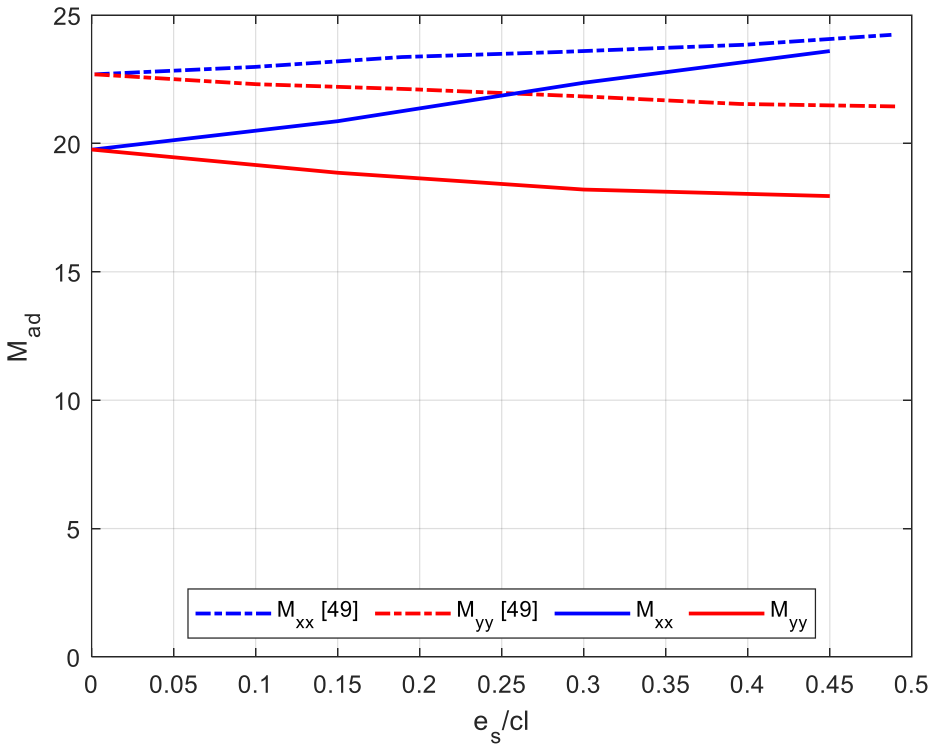

Fig. 3-23 Adimensional mass coefficient for open ends damper B, data from [49] *and model E*

For what regards the damping coefficient the comparison is proposed in Fig. 3-24. The horizontal component is always slightly higher than the one of the reference while the evolution of the vertical component crosses the line of the yy component of the reference. The damping coefficients show a moderate increase with the static eccentricity.

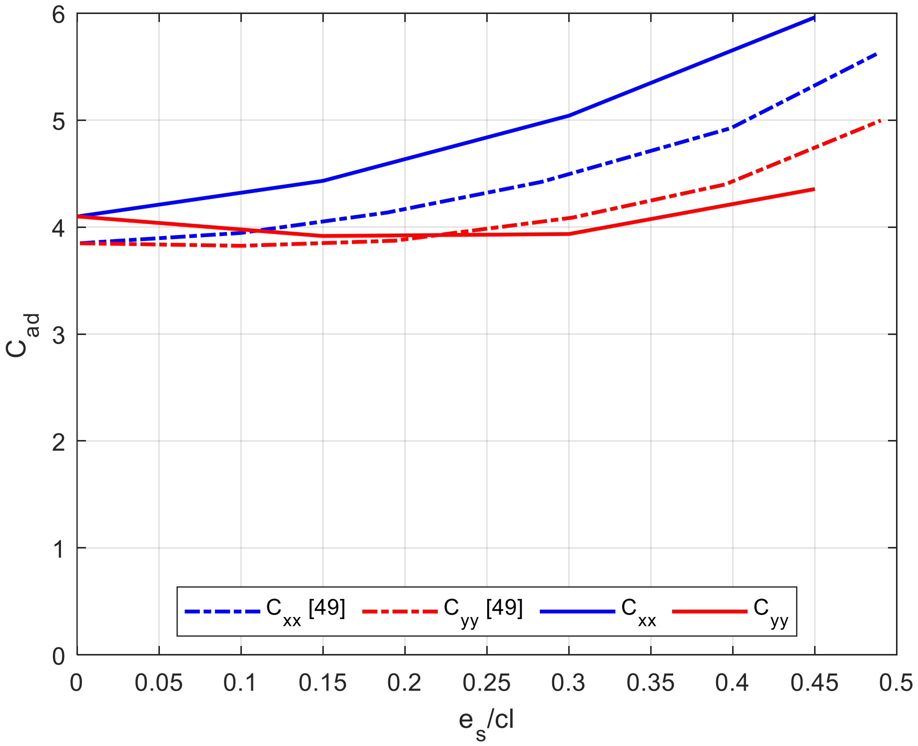

Fig. 3-24 Adimensional damping coefficient for open ends damper B, data from [49] *and model E*

It is interesting to notice that, for both the damping and mass coefficients, the horizontal and vertical components obtained with the model developed deviate quicker one from another with respect to the reference data.

The results shown above are obtained with $\omega = 100\ Hz$. The effect of the frequency was also investigated, see Fig. 3-25. It is possible to see that the mass coefficient rises quickly for low frequency and then becomes rather stable. The reason of this behavior can be attributed to the fact that, when the frequency is low, the dynamic pressure developed inside the damper is much lower to the pressure at the inlet orifices. For this reason the radial force, responsible for the mass coefficient, is strongly influenced by the inlet pressure. With the increase of the whirling frequency, the dynamic pressure becomes more relevant than the component related to the inlet system. The damping coefficient is, instead, not affected by the whirling frequency.

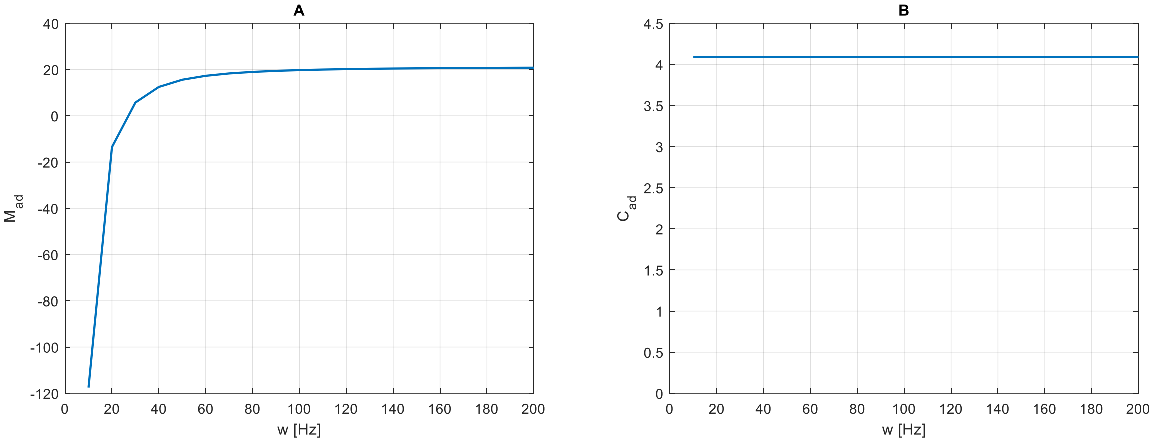

Fig. 3-25 Evolution of adimensional mass coefficient (A) and damping coefficient (B), for open ends configuration, with frequency. CCO with $e = 0.06cl$

For the centered orbit case, the force coefficients reach an asymptote when the frequency is increased. When a static eccentricity is present, the force coefficients at the low frequencies are higher. The presence of the static eccentricity determines a higher dynamic pressure, less influenced by the feeding orifices.

In [50], damper B is tested in sealed configuration. A piston ring is placed in both the extremities in order to reduce the outflow. In order to simulate its presence, the same approach adopted in the reference will be used. At both extremities, the outflow will be considered as:

$$Q_{out} = C_{seal}(P_{end} - P_{out}) \tag{75}$$

Where C_{seal} is the seal coefficient, determined experimentally in the reference, P_{end} is the pressure at the end of the damper and P_{out} is the external pressure, equal to the ambient one.

In Fig. 3-26 and Fig. 3-27 the comparison between the reference adimensionalized mass and damping coefficient and the ones obtained with the model developed in the previous chapter are shown. The results shown are obtained for the frequency range $\omega = 50 - 250\ Hz$. The orbit radius used is $\mathrm{e} = 0.055\mathrm{cl}$.

The prediction is reliable for the CCO case but with the increase of the static eccentricity the two mass coefficients are strongly reduced, especially the horizontal component. At the same time, the cross coupled components are increased. The reason of this discrepancy is the presence of a large cavitated region in the pressure predicted with the model proposed in this thesis. On the contrary, in the reference, the author states that no cavitation is registered. The same behavior with the static eccentricity is registered also for the damping coefficient.

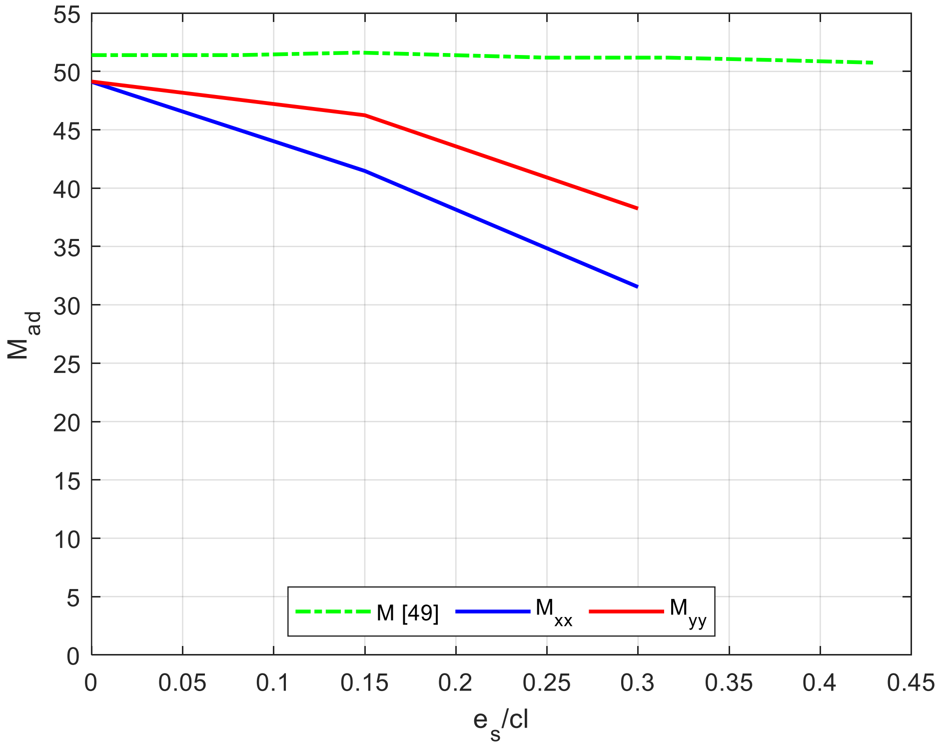

Fig. 3-26 Adimensional mass coefficient for sealed damper B, data from [50] *and model E*

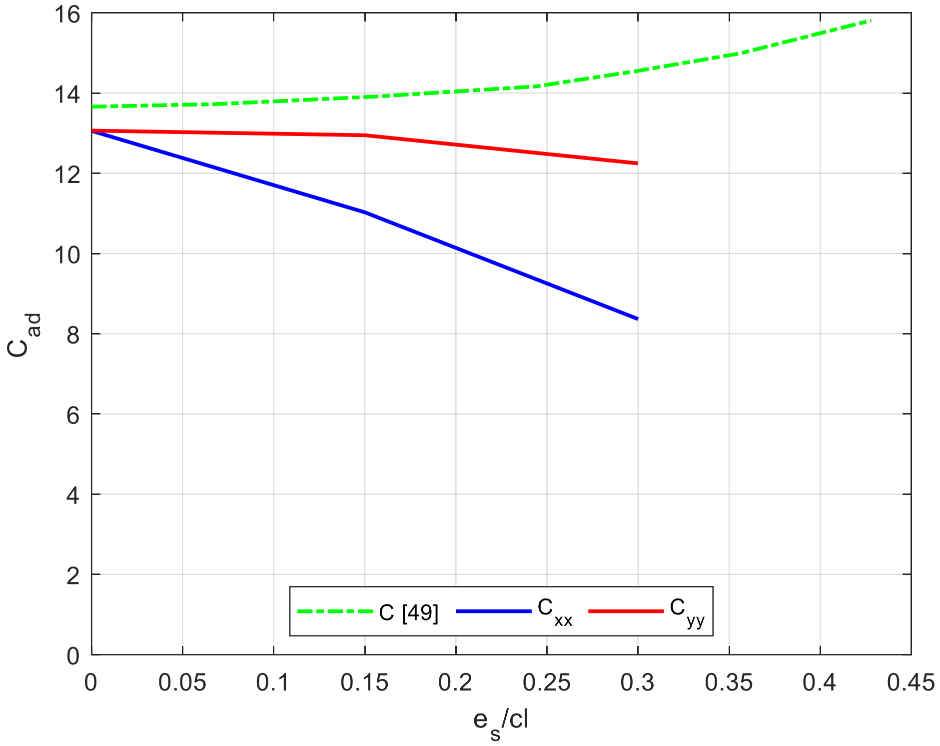

Fig. 3-27 Adimensional damping coefficient for sealed damper B, data from [50] *and model E*

In Fig. 3-28, the evolution of the force coefficients with the whirling frequency is reported. The damper is operated with $e = 0.055cl$ and $e_s = 0.3cl$. It is possible to see that the damping coefficients are stable already at the lowest frequency, while it is not the case for the mass coefficients. On the contrary, when the frequency is increased, the force coefficients, especially the horizontal component, is reduced. Together with this reduction, the cross coupled coefficients are increased, demonstrating that a cavitation zone is established. This phenomenon is not reported by the reference that, on the contrary, states that neither air ingestion nor cavitation are observed. The decrease of the force coefficients with the frequency becomes worse when the static eccentricity is increased.

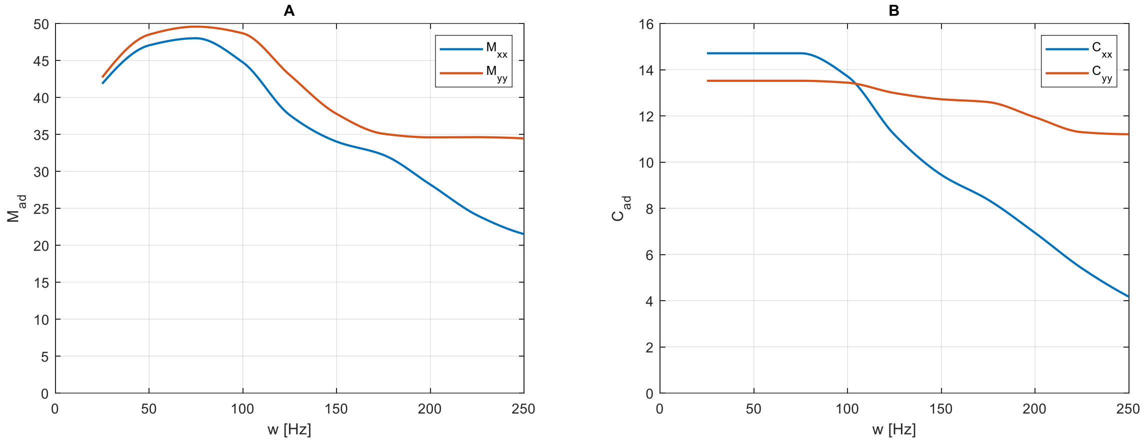

Fig. 3-28 Evolution of adimensional mass coefficient (A) and damping coefficient (B), for sealed configuration, with frequency. $e_s = 0.3cl$ *and* $e = 0.055cl$

A possible explanation, for the discrepancy between the numerical results obtained with this model and the ones shown in [50], can be the following. In the model developed, the radial coordinate is not simulated. For this reason, especially in the groove region, in case of the development of the cavitation zone, the fluid in the top part of the groove, that for now is not considered, can interact with the rest of the oil. Also the oil flow between the groove and the land is not taken into consideration in this model. It is possible to assume that some interaction will be present between the cavitation zone and the flow coming from the groove. On the contrary, the model used in the reference, is able to take into consideration the axial flow of oil between the different regions and, for this reason, is considered more accurate.

3.3.3. Damper A

Damper A has the same geometry of damper B but the length of the active lands is double. This determines higher values of dynamic pressures that in general will determine higher values of the damping and mass coefficients. Due to the higher values of active pressure, also the feeding pressure must be higher in order to guarantee the same feeding flow rate. As it was done for the previous damper, at first the feeding mechanism was tested in order to find the hole coefficients that, given the feeding pressure, guarantees the target inflow. The second step is to determine the effective groove depth that reproduces the closest results to the one show in the references. For the open ends results, the final value is $d_{ge} = 2.4cl$ when, the suggested value in [49], is $d_{ge} = 2.6cl$. In the open ends configuration the damper is tested for the frequency range $110 - 210\ Hz$. In Fig. 3-29 and Fig. 3-30, the values of the mass coefficients and damping coefficients for different values of the static eccentricity are shown. Since the length of the active length is different also the normalizing values of the mass and damping coefficients are different. Consider, as reference, that the normalizing force coefficients for damper A are more than seven times greater than the ones for damper B.

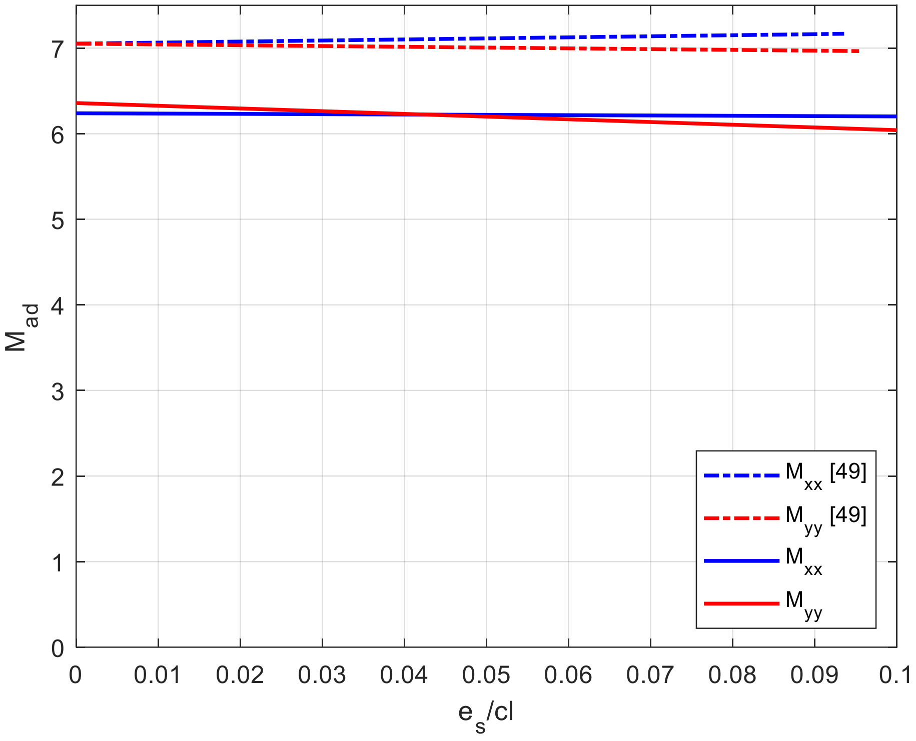

Fig. 3-29 Adimensional mass coefficient for open ends damper A, data from [49] *and model E*

It is possible to see that, for low values of the static eccentricity, the difference between the reference mass coefficients and the one obtained with the model is reduced. The reference coefficients are 15% higher than the numerical ones. For damper A, only low values of the static eccentricity are shown. For higher static eccentricities, a large region of cavitated fluid is developed. However, in [49], the authors do not report the establishment of cavitation. The reason of this discrepancy is assumed to be the same reported for damper B.

In Fig. 3-30, it is possible to see that the damping coefficients have almost the same values of the reference ones.

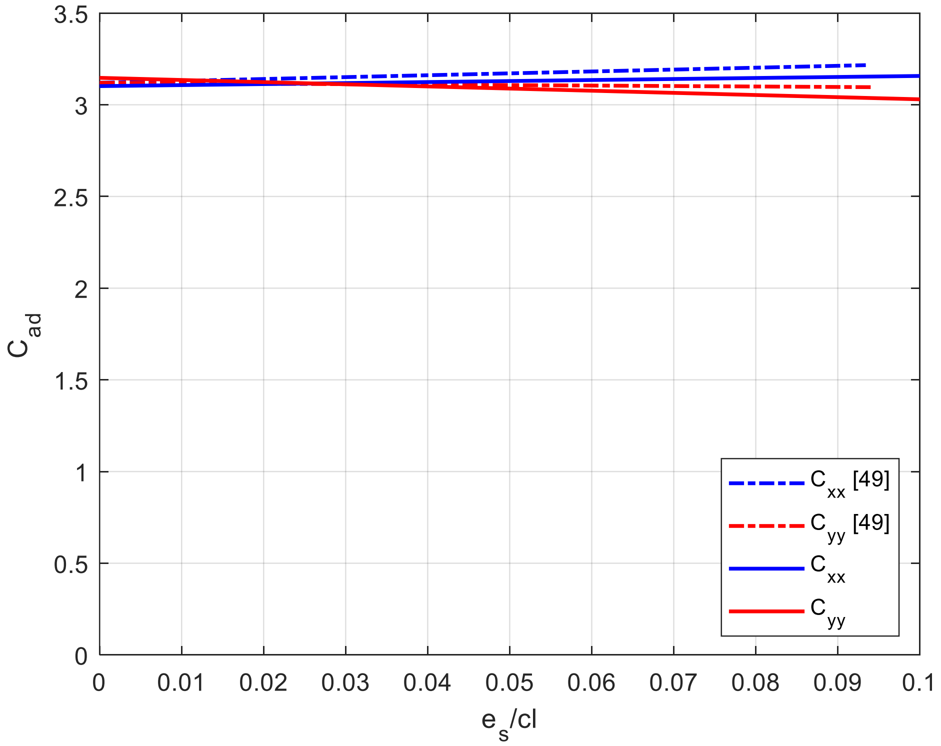

Fig. 3-30 Adimensional damping coefficient for open ends damper A, data from [49] *and model E*

In Fig. 3-31, the evolution of the force coefficients with the whirling frequency is shown. The static eccentricity is set to 30% of the damper clearance and the orbit radius is 10% the clearance. It is possible to see that the mass coefficient becomes almost half at the last frequency tested. On the other hand, the decrease of the damping coefficient is around the 30% of the initial value.

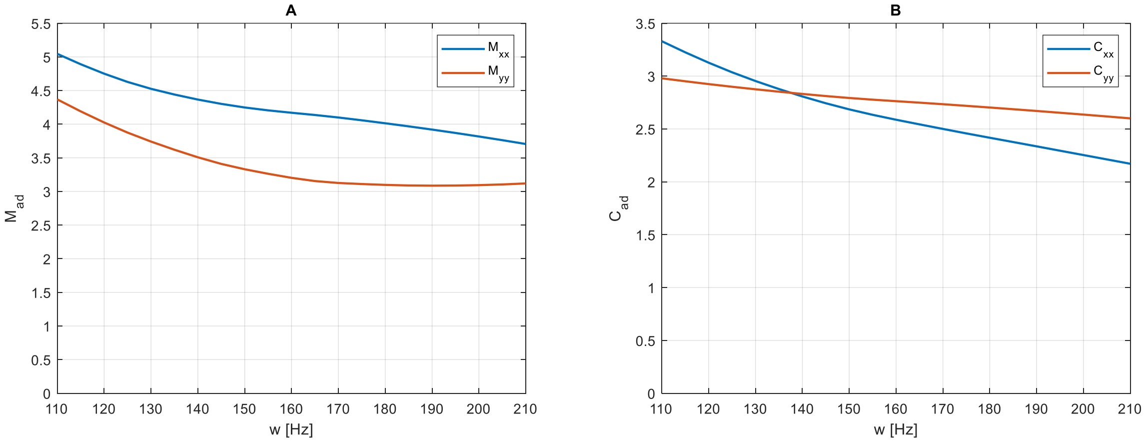

Fig. 3-31 Evolution of adimensional mass coefficient (A) and damping coefficient (B), for open ends configuration, with frequency. $e_s = 0.3cl$ *and* $e = 0.1cl$

Also damper A is tested with the extremities sealed with piston-rings. The frequency range considered is $w = 110 - 210\,Hz$ and the orbit radius is $\mathrm{e} = 0.055\mathrm{cl}$. The boundary condition adopted to simulate the seal behavior is the same as the one reported in the previous chapter but with a different seal coefficient. The results are obtained with $d_{ge} = 2.6cl$ while the one proposed in [50] is $d_{ge} = 3cl$.

In Fig. 3-32, the adimensional mass coefficient is presented. Also for the sealed configuration the results for a small static eccentricity are shown. The reason of the decrease of the coefficients is the establishment of a cavitated region. If the static eccentricity is small, the discrepancy between the reference data and the analytical ones is restrained, around 15%.

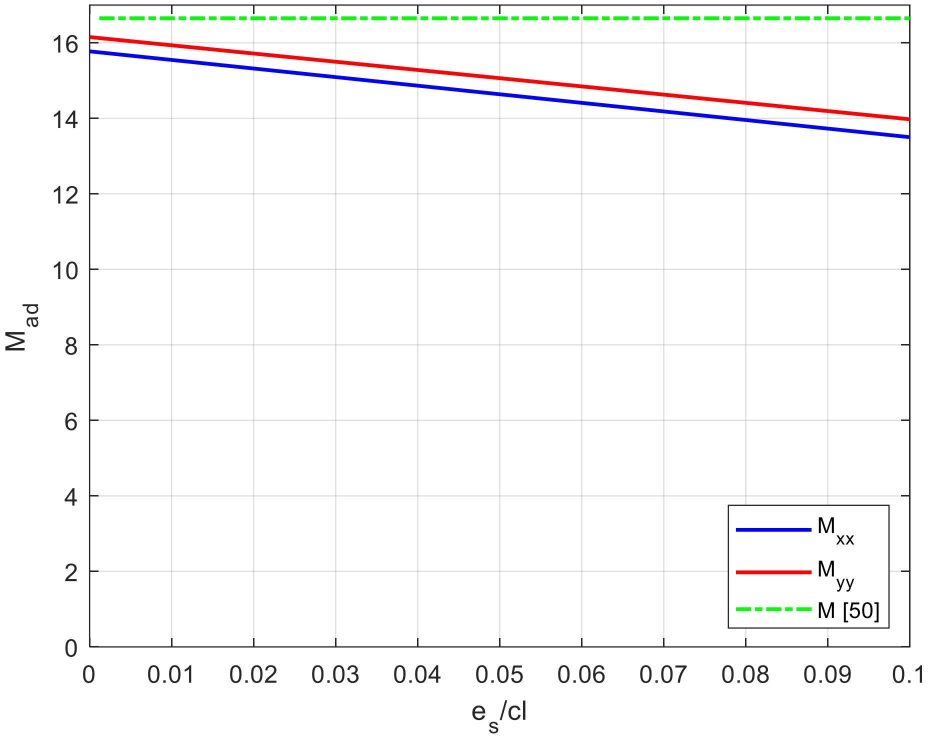

Fig. 3-32 Adimensional mass coefficient for sealed damper A, data from [49] *and model E*

In Fig. 3-33, the damping coefficients are reported. The similarity between the reference value and the numerical value is noticeable. However, as reported above for the mass coefficients, the presence of a cavitated zone is responsible of the decrease of the coefficients with the static eccentricity. When the static eccentricity is low, the extension of the cavitated region is also lower.

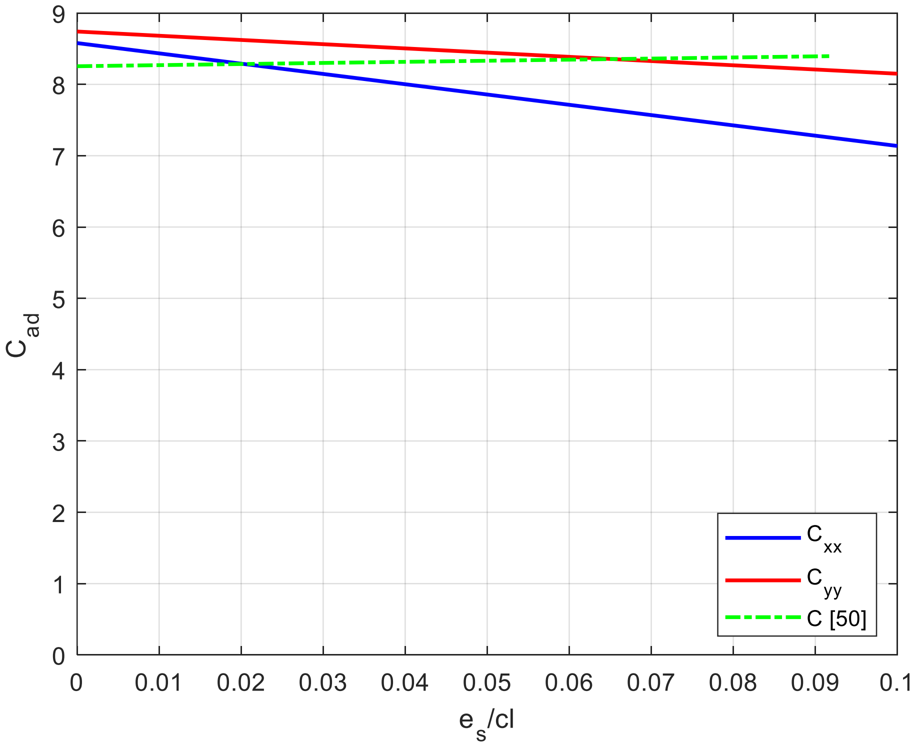

Fig. 3-33 Adimensional damping coefficient for sealed damper A, data from [49] *and model E*

Also for this case, the evolution of the force coefficients with the frequency is reported, see Fig. 3-34 when $e = 0.055cl$ and $e_s = 0.3cl$. It is possible to see that the behavior of the mass coefficient is different from what it was encountered before. While the xx component is decreased, the yy component increases its value when the whirling frequency is higher. On the contrary, the two damping coefficients are both slowly decreasing with the whirling frequency. Keep in mind that cavitation is active already from the first frequency.

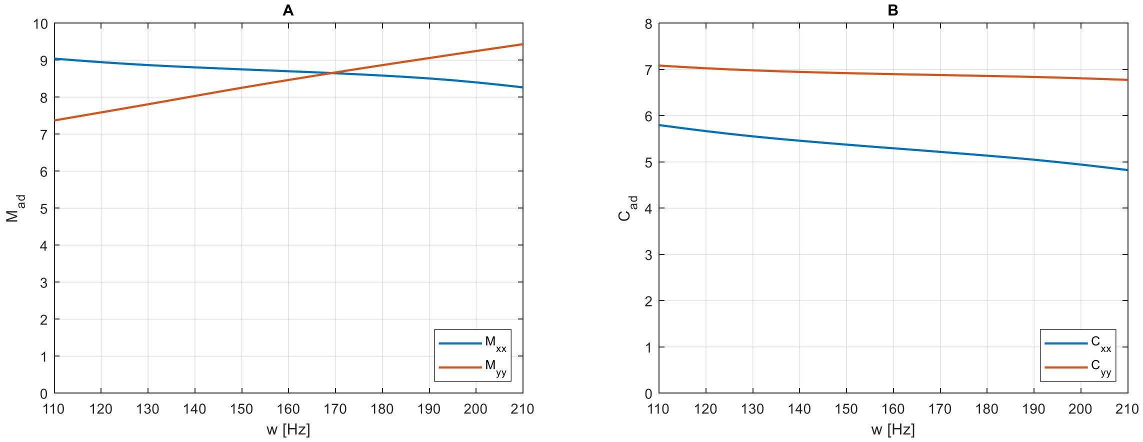

Fig. 3-34 Evolution of adimensional mass coefficient (A) and damping coefficient (B), for sealed configuration, with frequency. $e_s = 0.3cl$ *and* $e = 0.055cl$

For both damper A and damper B, the behavior of the proposed model can be considered reliable in case of CCO. On the contrary, especially when the dynamic pressure generated is high enough to determine the presence of a large cavitation region, the results obtained with the model cannot be considered reliable.

For what regards the cross-coupled coefficients, if cavitation is not present, their value is at least two orders of magnitudes lower than the direct ones. For this reason they can be considered negligible. They tend to increase with the static eccentricity and in the case of cavitation. However their value, at least for the frequencies and configurations tested, is always lower than the direct force coefficients.

4. MESH INDEPENDENCY

For every geometry that is tested it is important to find the level of refinement of the mesh above which, the changement of the results, can be considered negligible. In some cases it may be considered necessary to adopt a coarser mesh in order to keep the computational time at a reasonable value. In order to evaluate the grid independency, the radial and tangential force evolution is studied. The reason why these two parameters are chosen is that they are used to calculate the force coefficients, the final results to obtain.

An example of grid independency test is shown here for damper F of the previous chapter. At first, half the damper will be simulated and square elements will be considered. The number of axial points N_z is selected and then $N_x = kN_z\frac{2\pi R}{L}$ with $0 < k \leq 1$. With $k = 1$ the elements are squared. In Fig. 4-1 and Fig. 4-2 it is possible to see the effect on the tangential and radial forces and the relative error with the increase of the number of points.

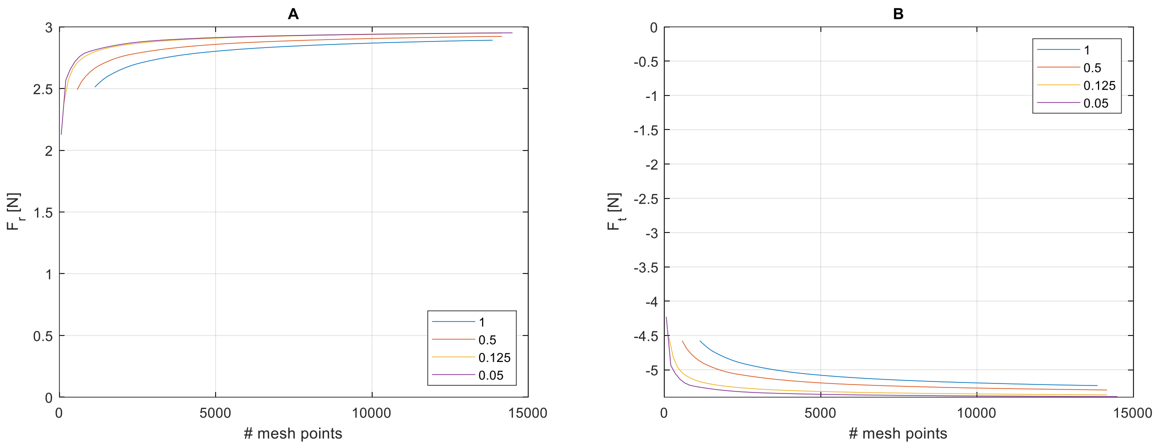

Fig. 4-1 Radial (A) and tangential (B) force for half damper simulation.

It is possible to see that increasing the number of points both forces will reach an asymptote. When k is reduced, i.e. when, for the same number of axial points, the number of tangential points is reduced, the shape of the forces are flatter. At the same time, the relative error is reduced more quickly.

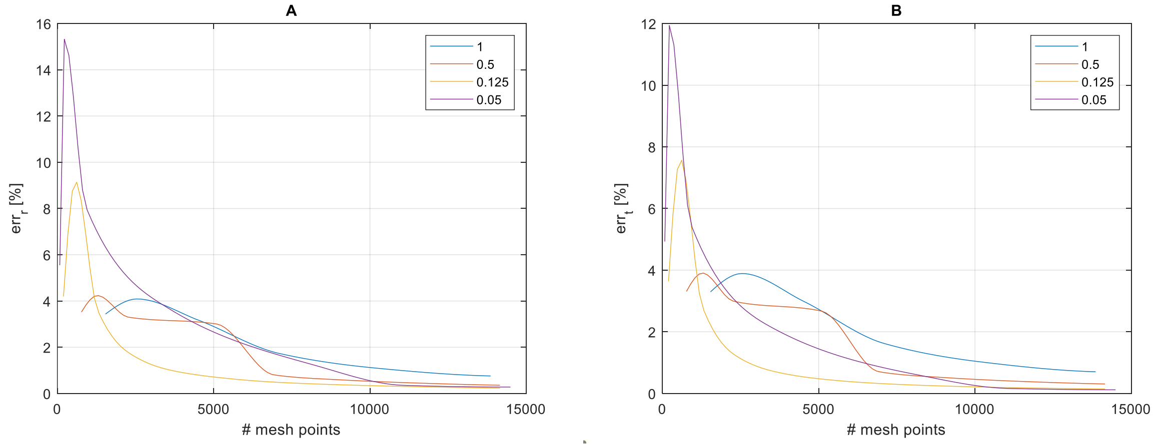

Fig. 4-2 Radial(A) and tangential(B) relative error for half damper simulation

In general, a relative error below 1% is considered acceptable. In order to keep the calculation time as limited as possible, the best mesh to adopt is the one with $k = 0.125$ and around 5000 mesh points.

In Fig. 4-3 Fig. 4-4 and the same results but when the whole geometry of the damper is simulated are shown. It is possible to see that the variation of the forces and the relative error with the mesh number of points, is less important than in the previous case. It is interesting to see that both relative errors are always below 1%. If the whole damper geometry is simulated, more mesh points are needed so, for this reason, the results obtained are more constant. It is also interesting to notice that the force values obtained with the whole damper geometry are slightly higher than the ones obtained for the simulation with half the geometry.

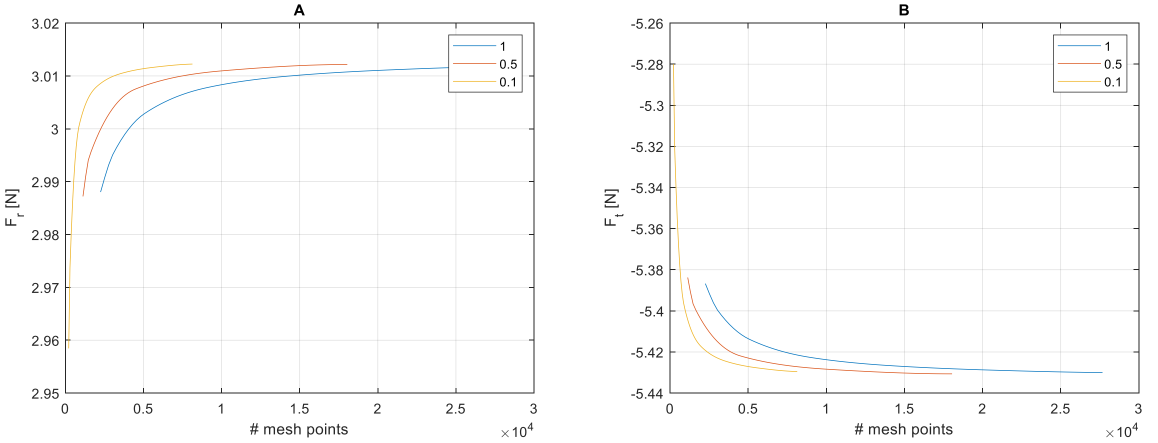

Fig. 4-3 Radial (A) and tangential (B) force for whole damper simulation

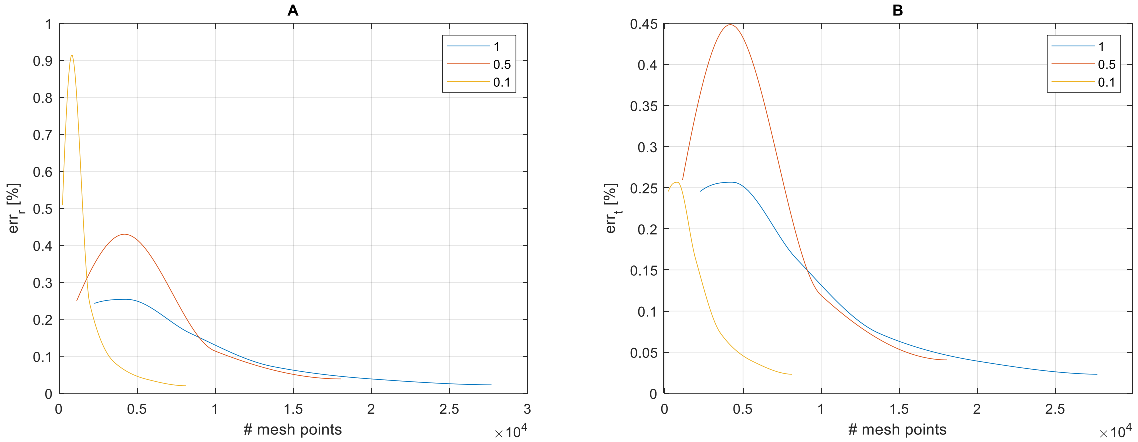

Fig. 4-4 Radial (A) and tangential (B) relative error for whole damper simulation

In general, if the effect of the feeding system is not considered, half of the damper is simulated. The calculation time is indeed lower when a rectangular mesh is applied to the half damper geometry. On the other hand, when the hole feeding system is considered, the whole geometry of the damper is simulated. Since the boundary condition used to represent the behavior of the feeding hole considers the flow in four directions, it is more correct to consider the whole damper rather than half of it because the symmetry plane would cut in half the hole making it more complex to correctly assign the boundary conditions. Considering that, even with squared elements, the relative error is well below the 1% threshold, a squared mesh is used to simulate dampers where the effect of the feeding system is considered. In this way the discretization of the orifices is easier.

5. FORCE COEFFICIENTS FOR DIFFERENT GEOMETRIES

In this chapter, dampers with basic geometries, will be tested. The effect of design parameters like the clearance, the length of the damper, the feeding and sealing system are investigated. The effect of this parameters on the air ingestion and cavitation will also be exposed.

5.1. Effect of smaller clearance

As reported in Table 3-3 the only difference between damper E and F is the clearance. For both dampers, air ingestion is, for now, neglected. As we see in Fig. 5-1, the smaller clearance determines higher force coefficients, both mass and damping. The force coefficients are adimensionalized with the coefficients, for damper F, obtained with classical lubrication formulas shown in [14]. The frequency range considered are the same ones reported in the previous chapter.

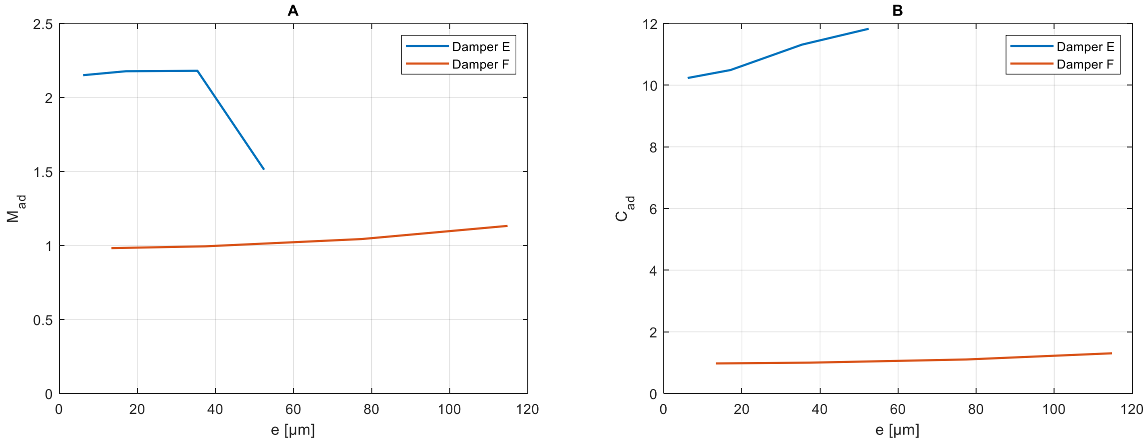

Fig. 5-1 Adimensional mass(A) and damping (B) coefficients for damper E and F

The mass coefficient for damper E is more than twice the one for damper F. However, when the orbit radius is high, the first one suffers a drop. The reason behind this behavior, is the presence of vapor cavitation. When the clearance is reduced and the frequency is increased, more dynamic pressure is generated so a larger region of the damper will deal with cavitated fluid. On the contrary, the damper coefficient is not affected in the same way. For the damper with half the clearance its value is always almost 10 times higher.

In Fig. 5-2 it is possible to see the evolution of the two force coefficients of damper E with the frequency. The decay of the coefficients starts just before 100 Hz. The mass coefficient at the last frequency is half the first one. The decrease of the damping coefficient is instead less severe, around 30%. This translates in an effect on the dynamic properties of the damper.

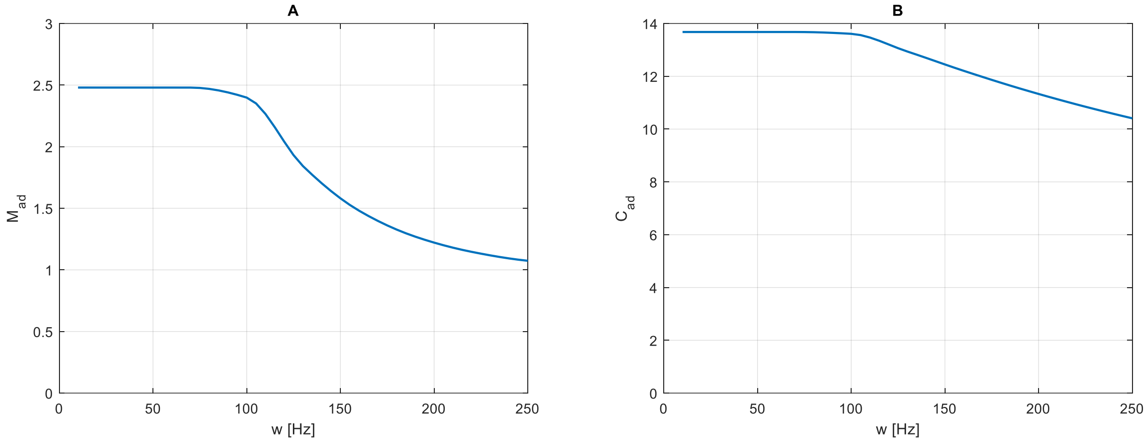

Fig. 5-2 Mass (A) and damping (B) coefficient evolution with frequency. Damper E, $e = 0.43cl$

5.2. Effect of damper length

Like clearance, another design parameter that influences the dynamic performance of the damper is the length. The choice of both these parameters can be strictly limited by the space availability in the region where the damper is mounted. For this reason it is important to understand, when spatial constraints are present, how to tune the performance of the damper. The force coefficients of damper F will be compared with one that is twice as long. In Fig. 5-3 we see the adimensionalized mass and damping coefficients for the two dampers. For now air ingestion will be neglected and the feeding system is not modeled. The same inflow of oil will be considered.

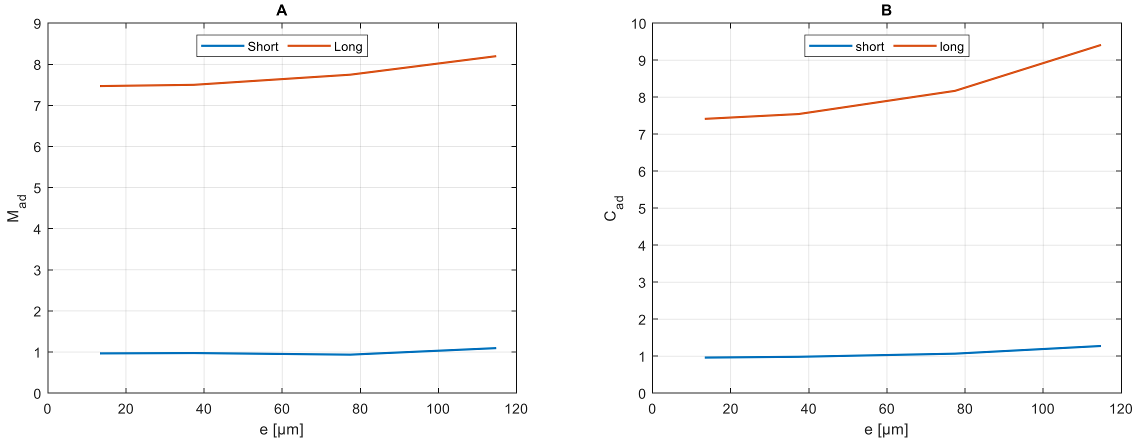

Fig. 5-3 Adimensional mass(A) and damping (B) coefficients for short and long damper, no air ingestion

In order to see if air ingestion can really be neglected, the evolution of the reference air volume fraction, for both the dampers is evaluated in Fig. 5-4. The two dampers are tested at the maximum orbit radius, corresponding to the condition of maximum air ingestion. It is possible to see that, with this boundary conditions, air ingestion is not completely negligible. The air ingestion for the long damper is much more critical. It easy to understand that a longer damper means more volume to be filled up with oil. If the frequency and the orbit radius for the two dampers are the same and also the inflow is constant, for the short damper it is easier to fill all the volume without letting the possibility to the air to enter.

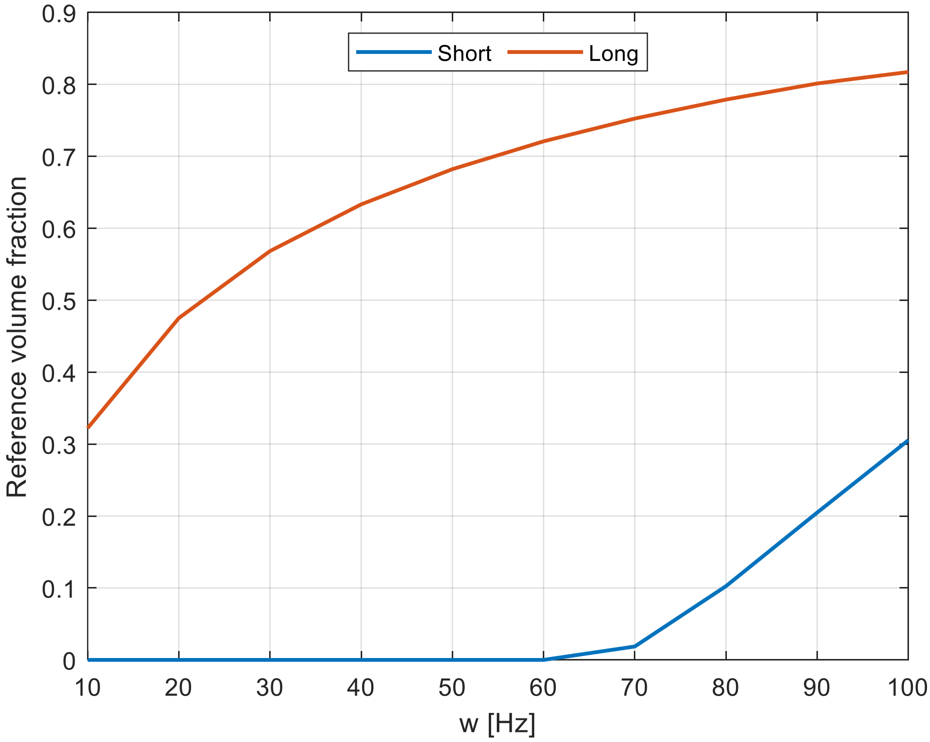

Fig. 5-4 Reference air volume fraction evolution with frequency for short and long damper

5.3. Effect of static eccentricity

The assumption of CCO cannot always be considered valid, especially if a static load is present. In the next figures, the effect of the static eccentricity on both damper E and F is investigated. The results shown are obtained without taking into consideration the air ingestion in order to separate its effect from the effects determined by the presence of the static eccentricity. In both cases the orbit radius is $e = 0.05cl$, the static eccentricities tested are $e_s = [0.1 \quad 0.2 \quad 0.3]^T cl$ and the frequency range for each damper is the same as the one reported in the previous chapter. The phase of the static eccentricity is 45° from the horizontal axis. The choice was done in order to keep the two direct coefficients almost identical.

The same inlet oil flow rate of the reference is considered and, in order to simulate the effect of the feeding system without modeling it completely, a static pressure field, with the feeding pressure at the middle of the damper, is summed to the dynamic pressure. Together with the adimensionalized direct force coefficients, Fig. 5-5, also the numerical evaluation of β_0 is proposed in order to understand if the hypothesis of no air ingestion can be considered always valid.

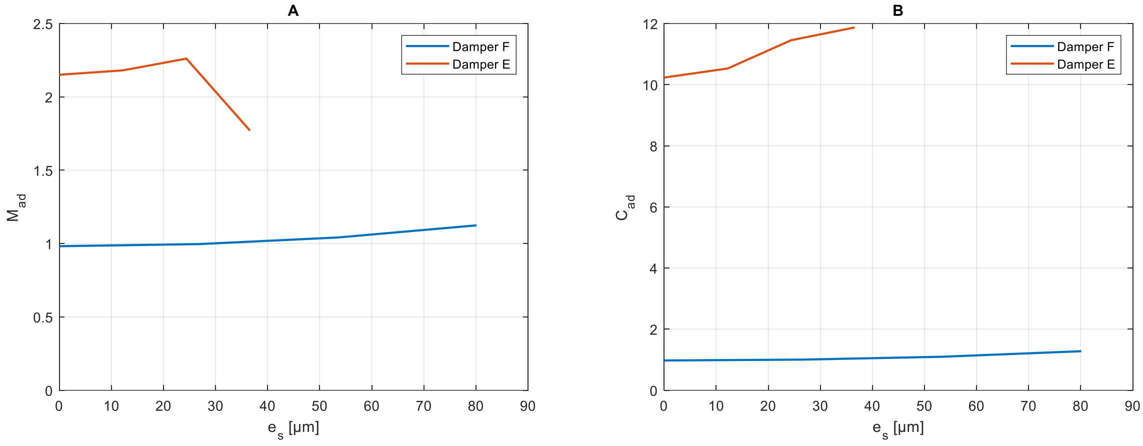

Fig. 5-5 Adimensionalized direct mass (A) and damping (B) coefficients with static eccentricity for damper E and F

For damper F, the one with the largest clearance, both mass and damping coefficients increase with the static eccentricity. The first of almost 15% while the second one of more than 30%. Consider that for the CCO case both coefficients, when the orbit radius is 30% of the clearance, are 12% higher than the ones with $e = 0.05cl$.

The evolution of the cross coupled coefficients is reported in Fig. 5-6. For both dampers, the cross coupled mass coefficients increase with the static eccentricity. However, for damper E, at the maximum eccentricity, the coefficient is negative. The reason is the development of a large cavitation zone, especially at the higher frequencies. The cross-coupled damping coefficients have a negative sign and their absolute value is increased with the static eccentricity. For damper E, at the maximum eccentricity, the absolute value of the damping coefficient is higher due to the presence of the cavitation zone.

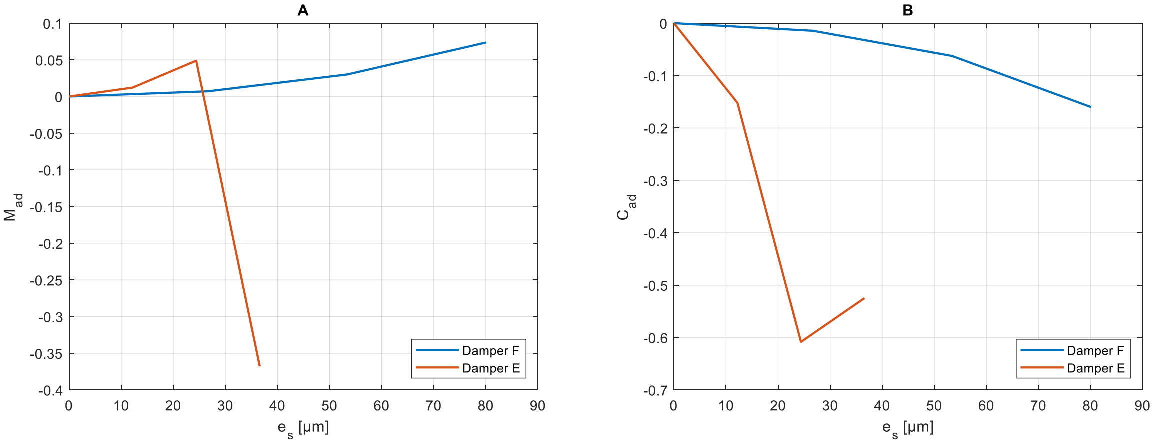

Fig. 5-6 Adimensionalized cross-coupled mass (A) and damping (B) coefficients with static eccentricity for damper E and F

In Fig. 5-7, the evolution of the direct and cross-coupled coefficients of damper E with the frequency is reported. Both direct coefficients decrease with frequency due to the presence of cavitation.

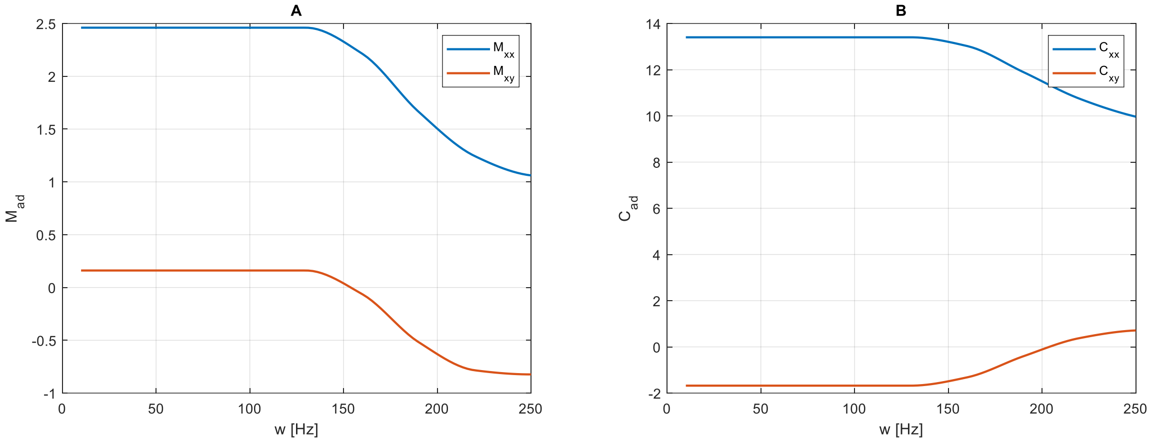

Fig. 5-7 Adimensional direct and cross coupled mass (A) and damping (B) coefficients with whirling frequency. Damper E, $e = 0.05cl$, $e_s = 0.3cl$

It is interesting to see that cavitation has the opposite effect on the cross-coupled coefficients. The mass ones are decreased while the damping ones are increased.

Due to the signs of the cross-coupled coefficients, especially the damping ones, it is important to keep controlled the static eccentricity. If the absolute value of the negative cross coupled coefficients is too high, there is a risk of establishing an instability. When cavitation is registered, the destabilizing effect of the cross coupled coefficients is limited if not eliminated.

In Fig. 5-8, the evolution of the reference air volume fraction with the frequency, for both dampers at the maximum static eccentricity is shown. The high value of the inlet pressure deforms the axial pressure distribution. For most of the operating conditions, the pressure gradient at the extremities is always negative. This guarantees a constant outflow of oil from the damper. When the static eccentricity and the frequency are increased, the dynamic pressure is increased. The consequence is that there are points at the damper’s extremities that have a positive axial pressure gradient, determining the ingestion of air. The maximum values of reference air volume fraction are less than 1% for damper F and 7% for damper E. For the first damper the effect of air ingestion can be neglected. On the contrary, for damper F, if the frequency is higher than 170Hz air ingestion must be taken into consideration.

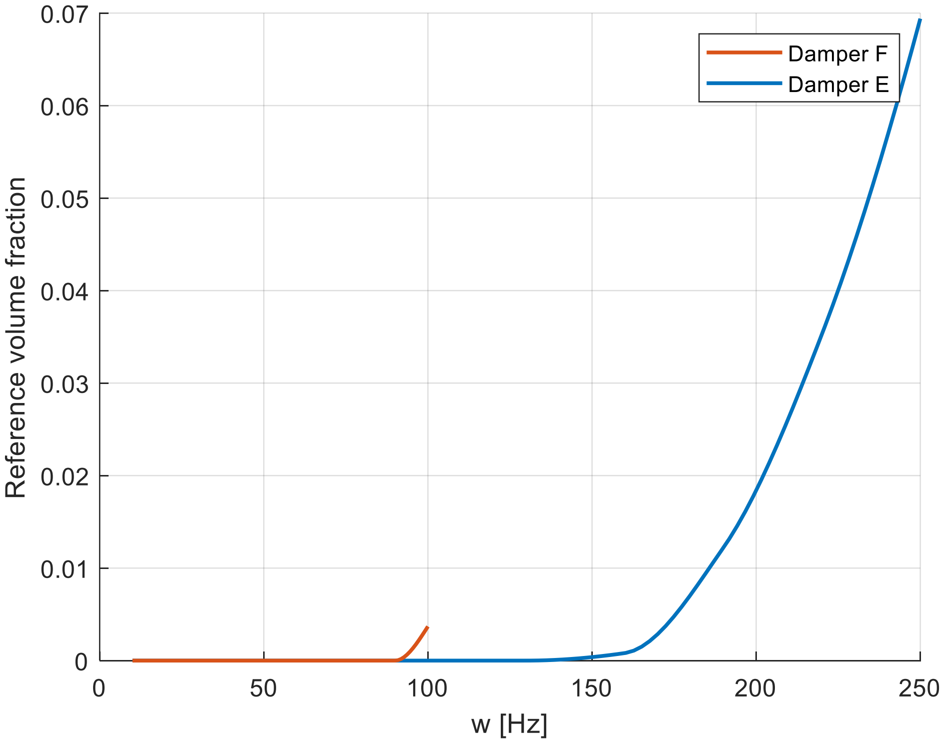

Fig. 5-8 β_0 *with frequency. Damper E and F,* $e = 0.05cl$, $e_s = 0.3cl$

5.4. Effect of feeding system

In order to study the effect of the feeding system, two dampers with the same axial length and radius of damper E and F have been investigated. The clearance considered are $cl = 0.15\ mm$ and $cl = 0.25\ mm$ and in both cases the orbit radius is 10% of the clearance. For the second damper it was investigated both the effect of the feeding pressure and the value of the feeding hole coefficient. For the first damper only the pressure effect is considered. Air ingestion is not considered in order to separates the effects. C_i is expressed in $\left[\frac{m^3}{sPa}\right]$ and correspond to the coefficient defined in 2.6.1.

The introduction of the feeding system, as reported in the previous chapter, has a strong effect on the mass coefficient. When the frequency is low, the dynamic pressure developed is low and the pressure of the oil flowing from the holes strongly influences the overall pressure evolution. On the contrary the damping coefficient is not affected. In Fig. 5-9. it is possible to see the frequency evolution of the mass coefficient for different values of the orifice flow coefficient. With higher C_i the force coefficient is flatter because the incoming flow has lower resistance.

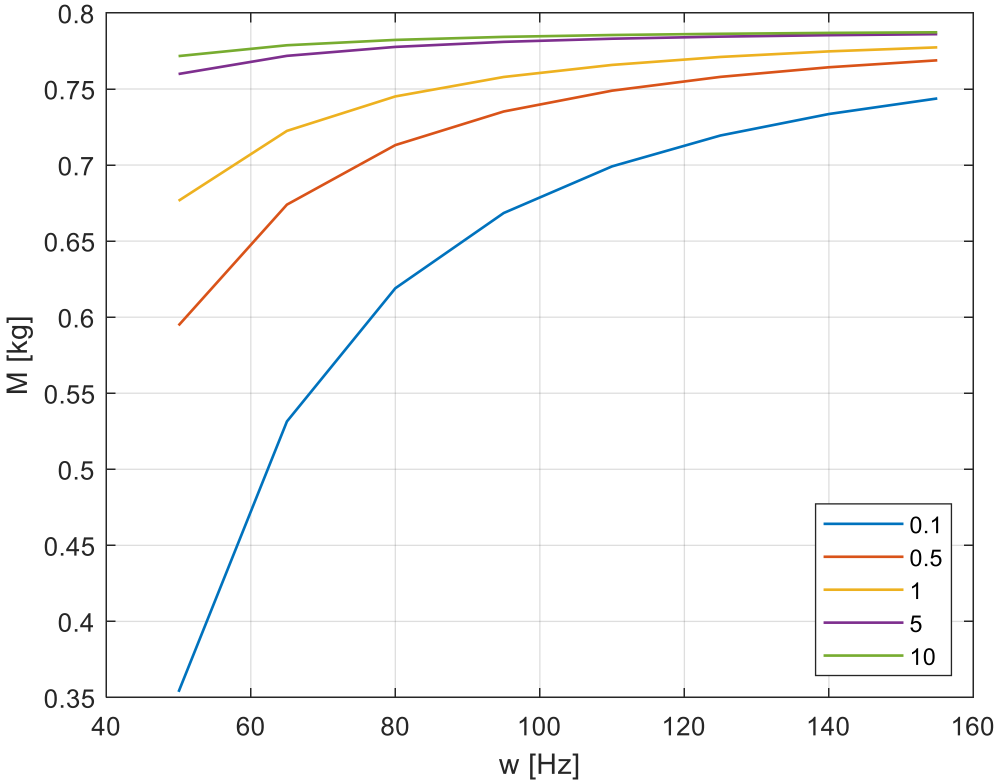

Fig. 5-9 Evolution of direct mass coefficient with frequency for different C_i. In the legend the values are expressed as $C_i \times 10^{-8}\left[\frac{m^3}{sPa}\right]$

In Fig. 5-10, the evolution of the oil inflow with the flow coefficient is reported. With constant feeding pressure, lower flow coefficient means higher flow resistance resulting in lower oil inflow.

Finally, a consideration on the expected value of reference air volume fraction is proposed, see Fig. 5-11Fig. 5-11 Evolution of β_0 with frequency for different C_i. In the legend the values are expressed as $C_i \times 10^{-8}\left[\frac{m^3}{sPa}\right]$. It is possible to see that, with higher inlet oil flow i.e. higher values of C_i, the content of ingested air is reduced. However, at least for the selected values of the hole flow coefficient, the variation of β_0 is not very strong. Let us consider that C_i was changed keeping the same number of points used to model the orifice in the mesh.

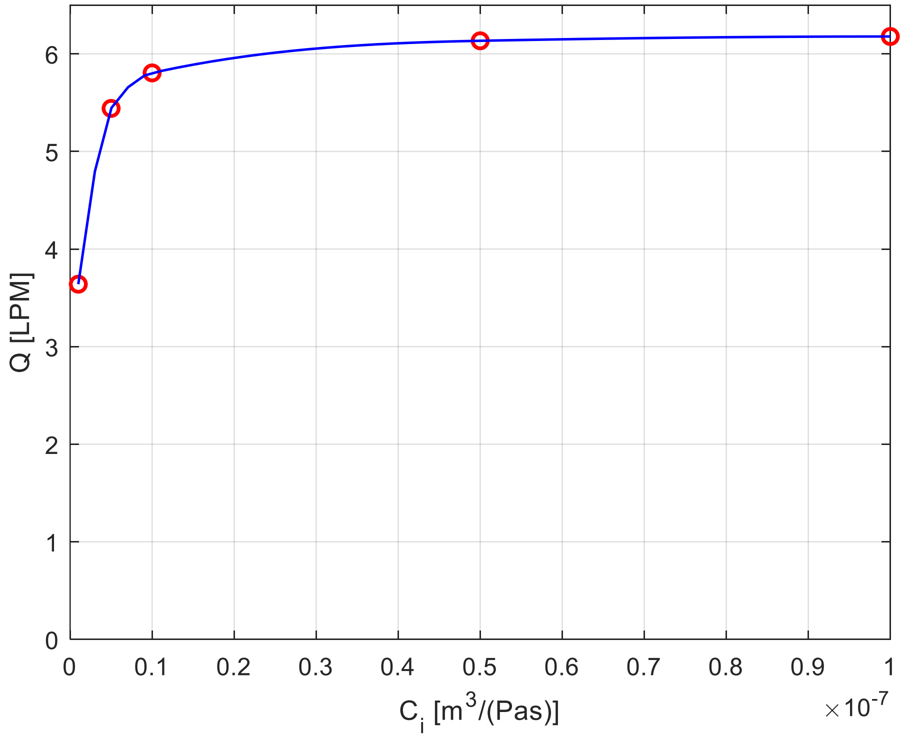

Fig. 5-10 Evolution of oil inlet flow with hole flow coefficient

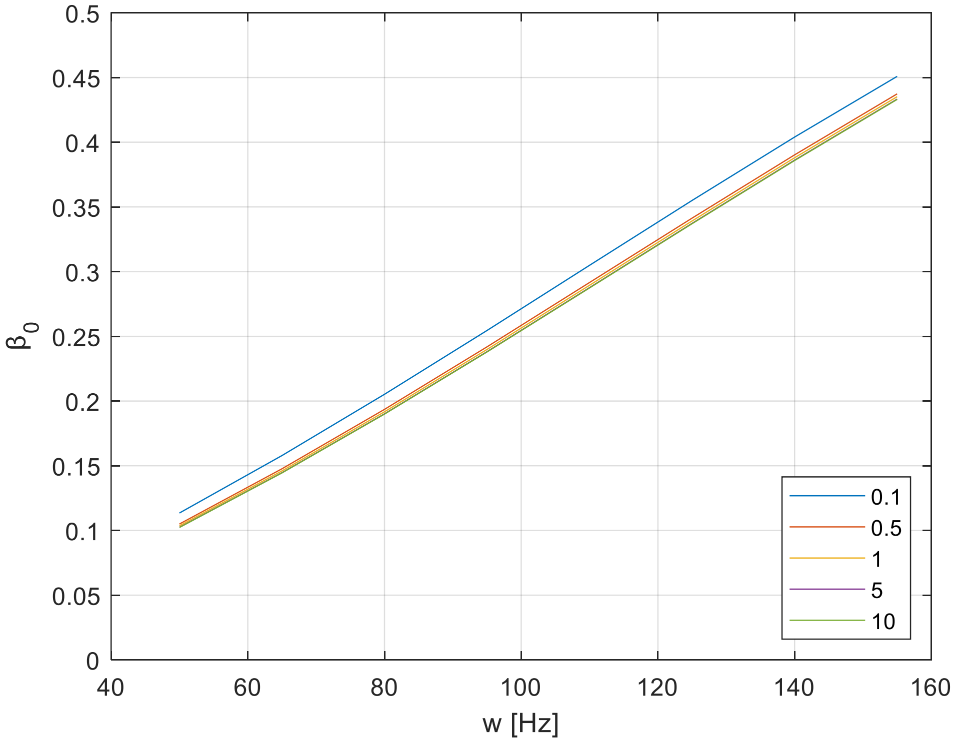

Fig. 5-11 Evolution of β_0 with frequency for different C_i. In the legend the values are expressed as $C_i \times 10^{-8} \left[\frac{m^3}{sPa}\right]$

In the next graphs the effect of the feeding pressure on the damper with the highest clearance is investigated. The feeding hole coefficient is kept constant at $C_i = 1 \times 10^{-8} \left[\frac{M^3}{sPa}\right]$. At first, in Fig. 5-12, it is possible to see the evolution of the direct mass coefficient with the frequency. When the feeding pressure is higher the variation of the coefficient with the frequency is higher. It is easy to imagine that if the feeding pressure is higher its effect on the pressure evolution will be more evident, higher pressure peaks in correspondence of the holes are present.

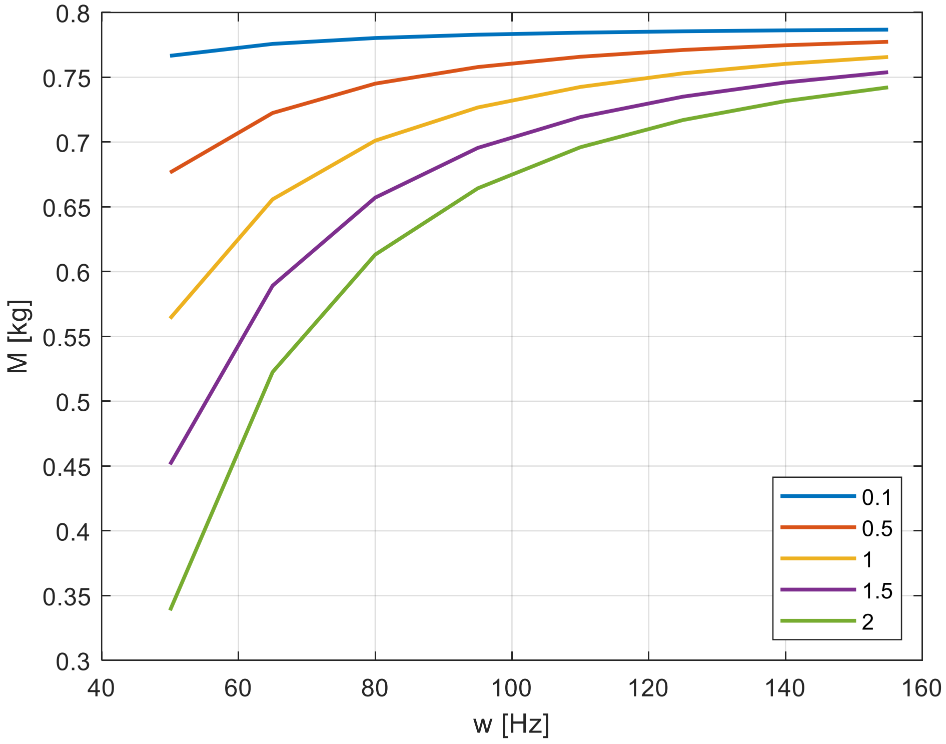

Fig. 5-12 Evolution of mass coefficient with frequency for different values of feeding pressures. Pressure expressed in [bar]

In Fig. 5-13, the evolution of the oil inlet flow rate with the feeding pressure is reported. A linear dependency exists between the two parameter. On the contrary, if the hole flow coefficient is changed, the flow rate has a non-linear behavior and tends to reach an asymptotic value.

In Fig. 5-14, the evolution of the reference air volume fraction with the frequency and for different feeding pressures is reported. Differently from the hole flow coefficient, the effect of the feeding pressure on β_0 is more important. Also in this case the evolution of the reference air volume fraction is almost linear.

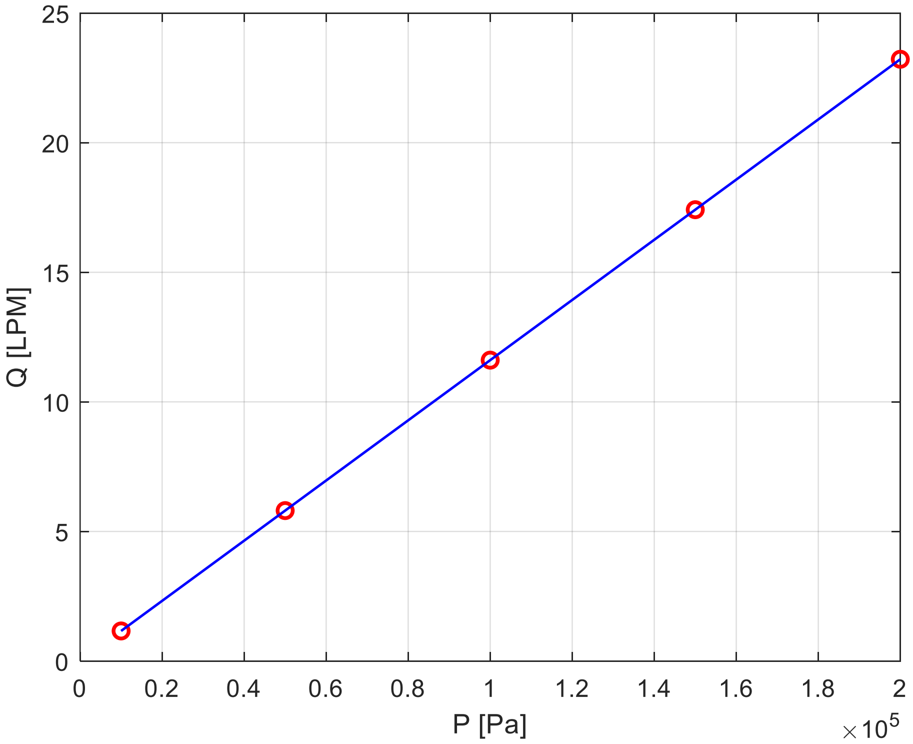

Fig. 5-13 Evolution of inlet oil flow rate with feeding pressure

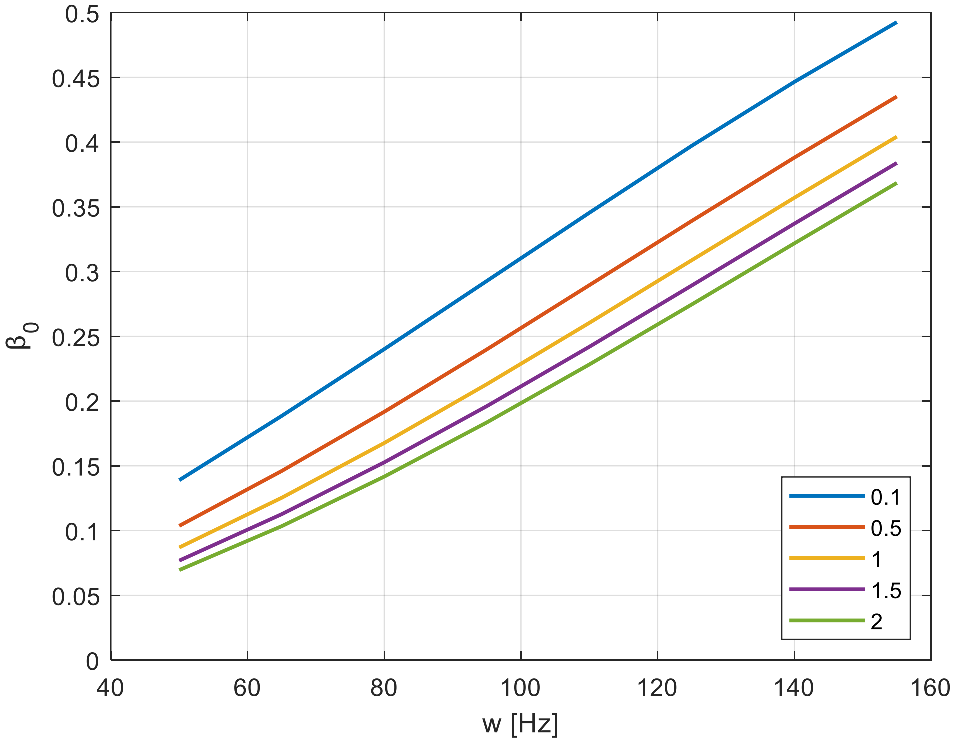

Fig. 5-14 Evolution of β_0 with frequency for different feeding pressure. In the legend the values are expressed in [bar]

The same analysis reported in the previous pages is carried out for the damper with the lowest clearance. In Fig. 5-15 it is possible to see the evolution of the mass coefficient with the whirling frequency with different feeding pressures. As noted for the previous geometry, the higher the feeding pressure, the stronger the dependency of the force coefficient with the frequency.

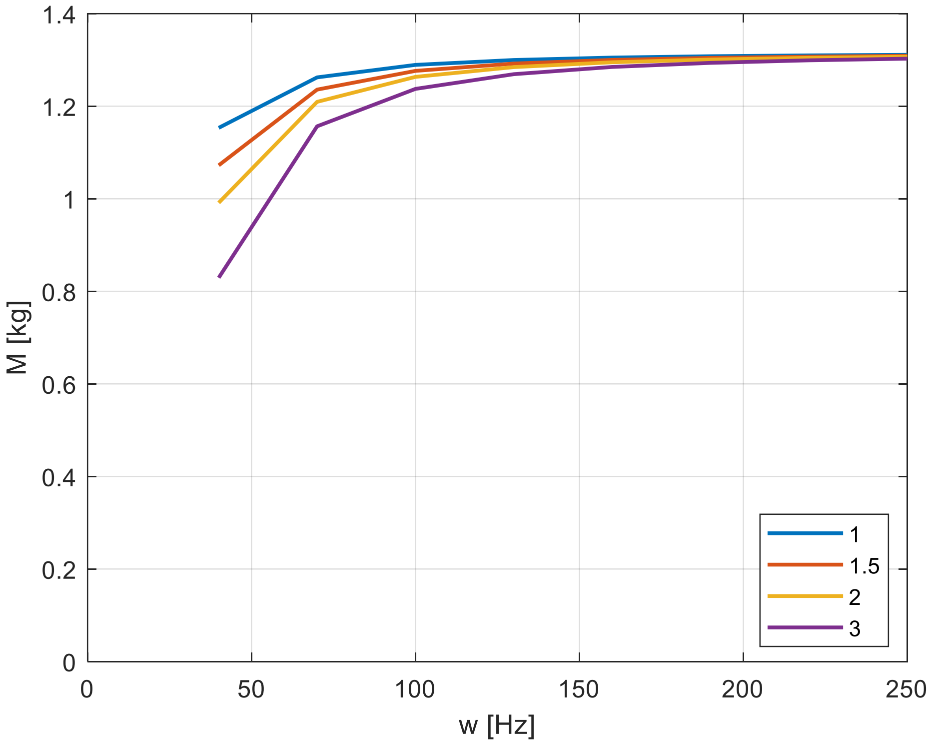

Fig. 5-15 Evolution of mass coefficient with frequency for different values of feeding pressures. Pressure expressed in [bar]

Also for this geometry, the feeding flow rate has a linear dependency with the feeding pressure. It is interesting to notice that the slope of the curve is lower than the one of the previous geometry, see Fig. 5-16. The lower clearance of the damper determines the development of higher dynamic pressures. For this reason the effect of the feeding pressure is less determinant on the dynamic pressure.

In Fig. 5-17, the evolution of the reference air volume fraction with the frequency, for different feeding pressure is reported. As expected, since the dependency of the feeding flow rate with the pressure is lower for the damper with the lowest clearance, also the dependency of β_0 is lower than the case with higher clearance.

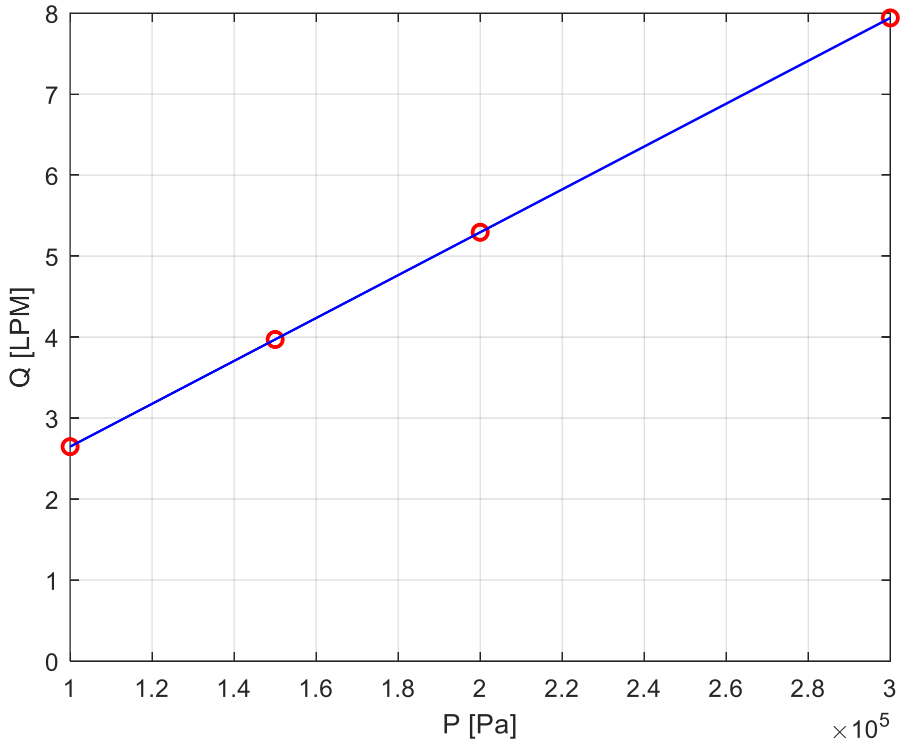

Fig. 5-16 Evolution of inlet oil flow rate with feeding pressure

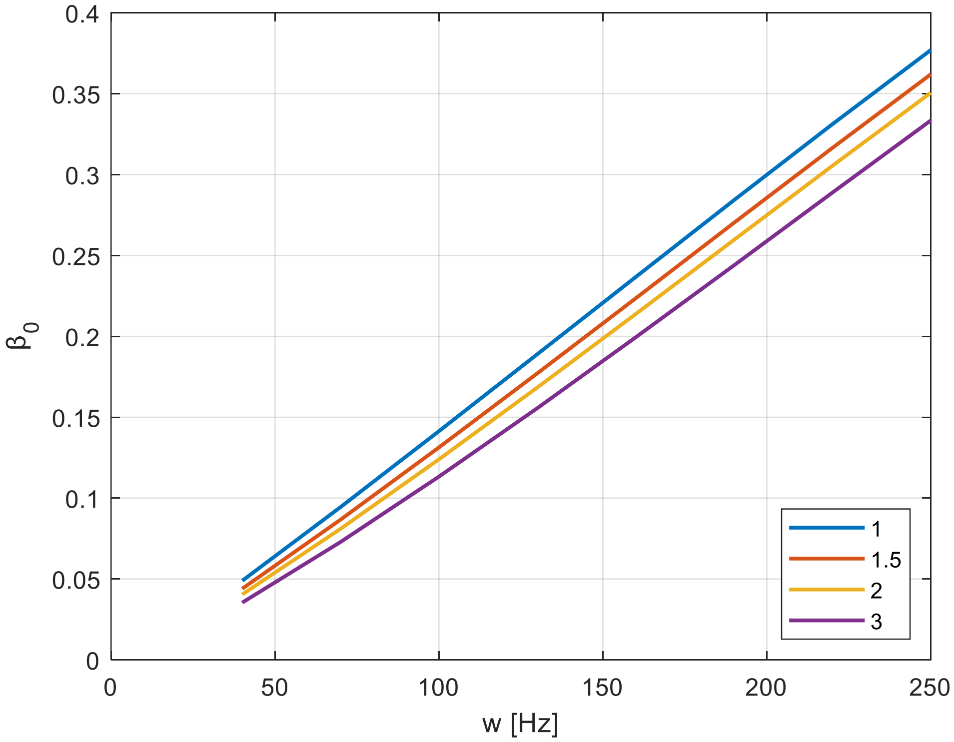

Fig. 5-17 Evolution of β_0 with frequency for different feeding pressure. In the legend the values are expressed in [bar]

The feeding system was also tested for damper F in order to verify if the same force coefficients are obtained. At first, different hole flow coefficients were tested in order to obtain the same feeding flow rate, reported in [14], for the given supply pressure.

As reported below, the mass coefficient shows a strong dependency on the whirling frequency when the model of the feeding system is introduced in the calculation. When the frequency is high enough, the force coefficient reaches an asymptote. On the contrary, the damping coefficient is almost constant with the frequency. In Fig. 5-18, the behavior for $e = 0.05cl$ is reported.

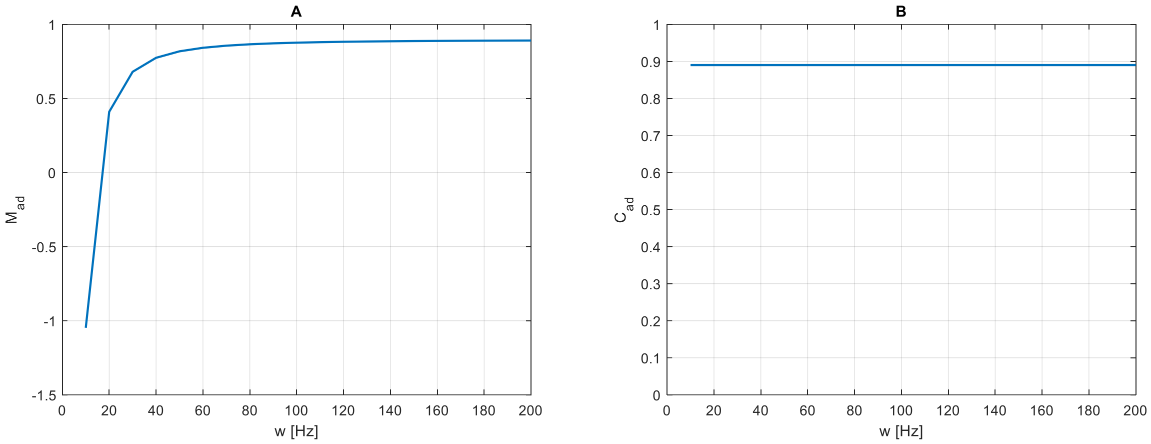

Fig. 5-18 Adimensional mass (A) and damping (B) coefficients for damper F with $e = 0.05cl$

In order to compare the results of the model with and without the feeding system, the results shown below are obtained for $\omega = 100\ Hz$. It can be assumed that above this value, the mass coefficient is almost independent on the frequency. In Fig. 5-19, the two force coefficients are reported for different orbit radius.

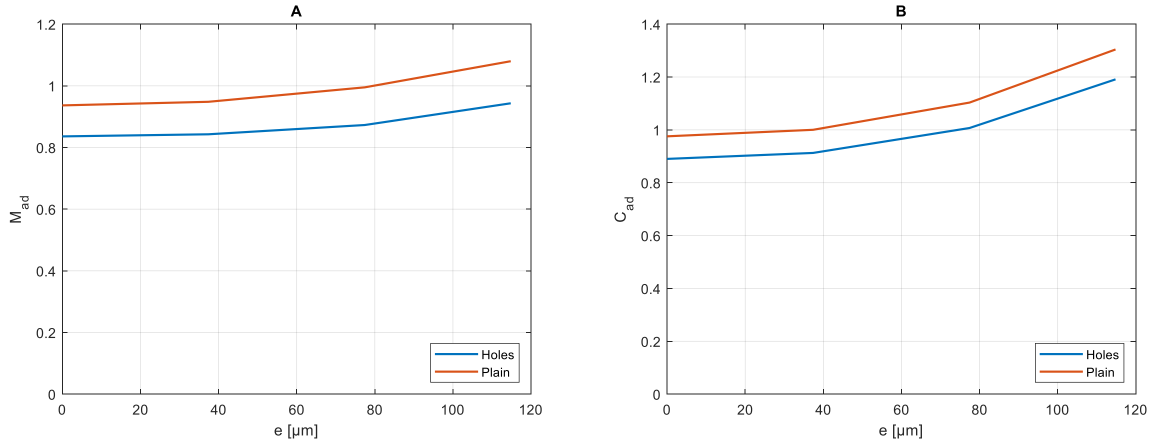

Fig. 5-19 Adimensional mass (A) and damping (B) coefficients for damper F with and without feeding system model

The values obtained with the original model are compared to the ones obtained when the feeding orifices are added. In both cases the second ones are 10% lower than the firsts. The reasons behind the discrepancy can be various. At first the hole model is a simplification of the real feeding system. Then this model does not calculate the radial evolution of the pressure that close to the holes will not be perfectly constant.

In Fig. 5-20, the different reference air volume fractions are shown for $e = 0.43cl$. It is interesting to see that the one obtained with the orifice model assumes intermediate values respect to the ones obtained when the plain geometry, with and without static pressure addition.

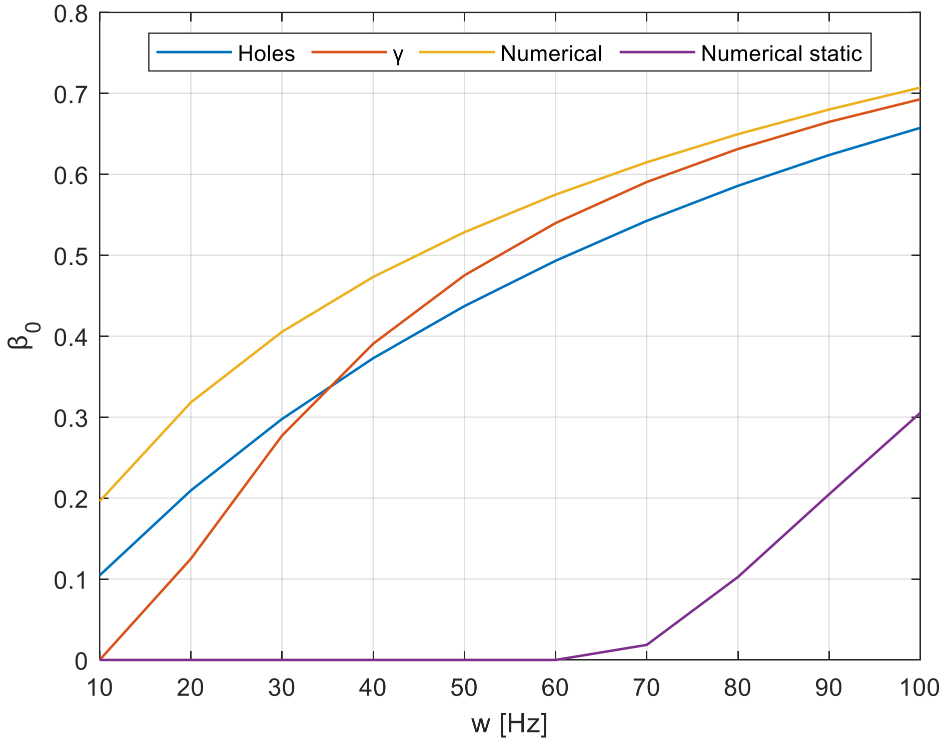

Fig. 5-20 Evolution of β_0 with ω for different models

5.5. Effect of air ingestion

As reported in the literature, air ingestion, together with cavitation, are the main factors that reduce the dynamic properties of SFDs. Air ingestion is a complex phenomenon to model in detail. To completely understand the effect of the presence of air bubbles in the lubricant film, a 3-D model that studies the dynamics of the bubbles should be developed and integrated with a 3-D model for the oil behavior, considering both feeding and discharge system. Luckily, the model proposed here is able to predict, with an acceptable accuracy, the effect of air ingestion on the damper's force coefficients.

In this chapter, the effect of the reference air volume fraction is tested on damper F. β_0 is assigned *a priori* and its effect is checked at 100 Hz, in case of CCO with $e = 0.2cl$ and for statically eccentric circular orbits with $e = 0.05cl$ and $e_s = 0.3cl$. This geometry was also selected in order to avoid the risk of cavitation so to keep the two phenomena separated.

In Fig. 5-21 we see the evolution of the adimensional mass and damping coefficients with the parameter β_0.Both coefficients are divided by their value with no air ingestion and are reduced when the reference air volume fraction is increased. When $\beta_0 = 0.5$, so at the axial extremities, the mixture is composed half by air and half by oil, both coefficients are almost half the original ones.

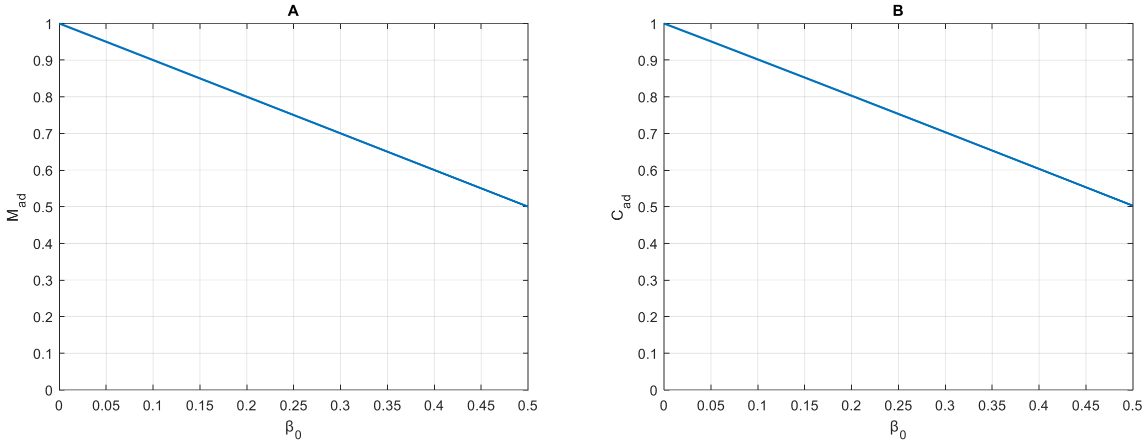

Fig. 5-21 Evolution of adimensional mass(A) and damping (B) coefficients with the reference air volume fraction

It is interesting to see that there is a linear dependency between β_0 and the force coefficients. The cross coupled coefficients are at least five orders of magnitude lower than the direct ones so they can be considered negligible.

The configuration with the static eccentricity was studied in order to see the effect of the air ingestion on the cross-coupled coefficients. In this configuration they have indeed higher values. In Fig. 5-22, the evolution of the adimensional direct mass and damping coefficients with β_0 is shown. Also in this case they decrease linearly with the air content. It is interesting to see that the cross-coupled coefficients have the same trend as the direct ones.

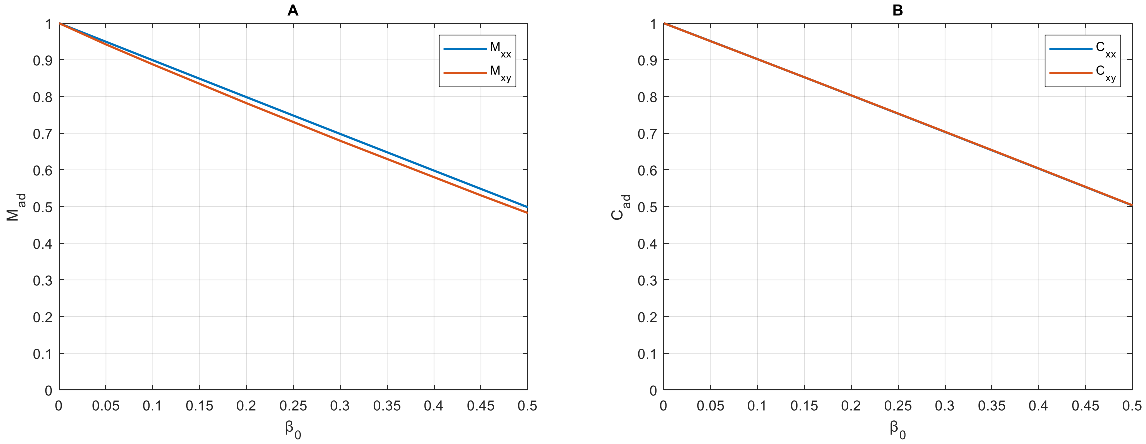

Fig. 5-22 Evolution of adimensional, direct and cross-coupled, mass (A) and damping (B) coefficients with the reference air volume fraction

It is also interesting to see how the air content will affect the ratio between the direct and the cross-coupled coefficients. In Fig. 5-23, it is plotted the ratio between the cross-coupled force coefficient and the direct one. For the damping coefficient the absolute value is considered since the cross-coupled coefficients have a negative sign. For the damping coefficient the ratio remains more or less constant. On the other hand the ratio for the mass coefficient tends to slightly decrease with β_0.

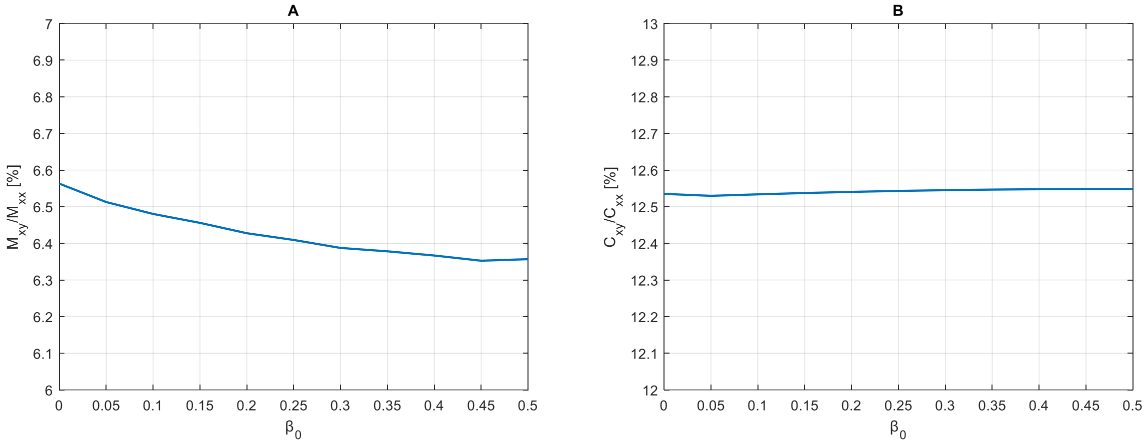

Fig. 5-23 Ratio in percentage between cross-coupled and direct mass (A) and damping (B) coefficients with β_0

5.6. Effect of end seals

The end seals taken into consideration in this analysis are piston rings because its boundary condition requires less parameters to be set. For simplicity, all the parameters that are needed to correctly model the seal, like the height and length of the P-R, are grouped in a general coefficient $C_{seal}\left[\frac{m^3}{sPa}\right]$. In this way the boundary condition is similar to what is used in [50].

At first the effect of the seal, without the presence of the feeding system, is investigated. The geometry selected for this configuration is the one of damper F with $e = 0.2cl$. The frequency range considered goes from 50 to 150 Hz. The seal coefficient is varied from $5 \times 10^{-6} - 5 \times 10^{-10}$ because it was observed that, in the first case the damper behaves almost as in the open ends case. On the other hand, when the minimum coefficient is adopted, the damper behavior is close to the case of completely sealed ends. In Fig. 5-24, the exiting flow rate, divided by the open ends case is shown. It is interesting to see that, with the minimum flow coefficient, the total flow rate is 40% the initial one. The results shown are for $\omega = 100\ Hz$. Keep in mind that the flow rate increases with the frequency. For visualization purposes the data at $C_{seal} = 5 \times 10^{-6}$ is not shown.

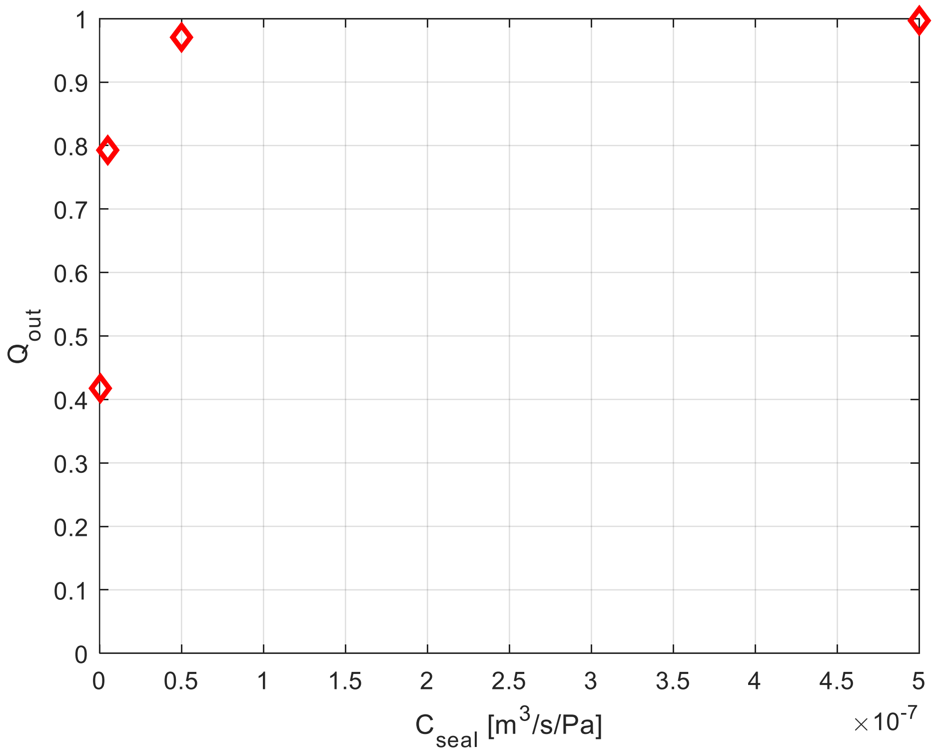

Fig. 5-24 Evolution of adimensional outflow with end seal coefficient.

The force coefficients are constant with the frequency but strongly affected by the seal coefficient. In Fig. 5-25, the evolution of the adimensional mass coefficient with C_{seal} is reported. It is interesting to see that when the seal coefficient is $C_{seal} = 5 \times 10^{-8}$, even if the outflow is reduced of less than the 5%, the mass force coefficient is more than 3 times higher than the one with open-ends configurations.

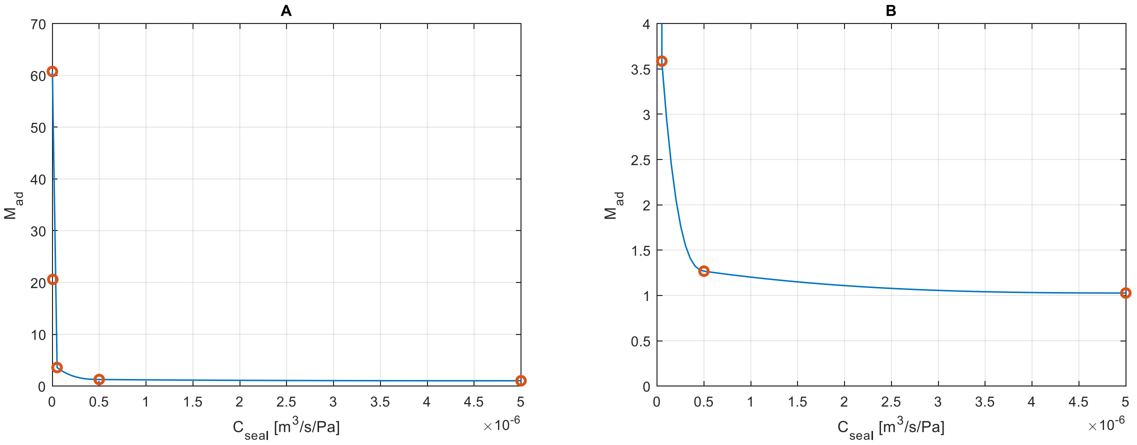

Fig. 5-25 Evolution of adimensional mass coefficient with C_{seal} (A) and magnification (B).

The damping coefficient have a similar trend with C_{seal}. See Fig. 5-26. Only the direct force coefficients are reported because the cross-coupled ones are negligible.

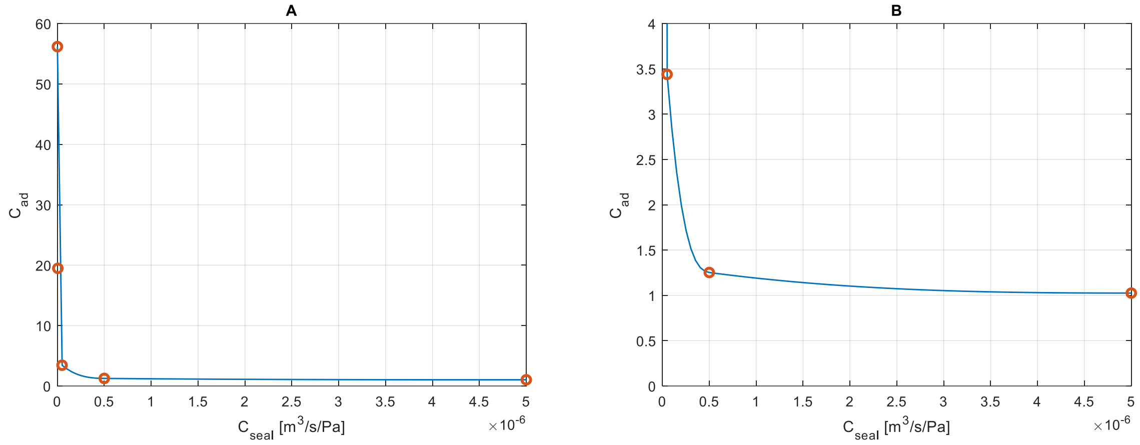

Fig. 5-26 Evolution of adimensional damping coefficient with C_{seal} (A) and magnification (B)

The reason why seals are used are basically two: increase the damping capability of shorter dampers and reduce the ingestion of air. The effectiveness of the P-R in this is shown in Fig. 5-27. The evolution of the reference air volume fraction with the frequency is reported for different values of C_{seal} expressed in $\left[\frac{m^3}{sPa}\right]$. The feeding flow rate is considered constant for all the simulations.

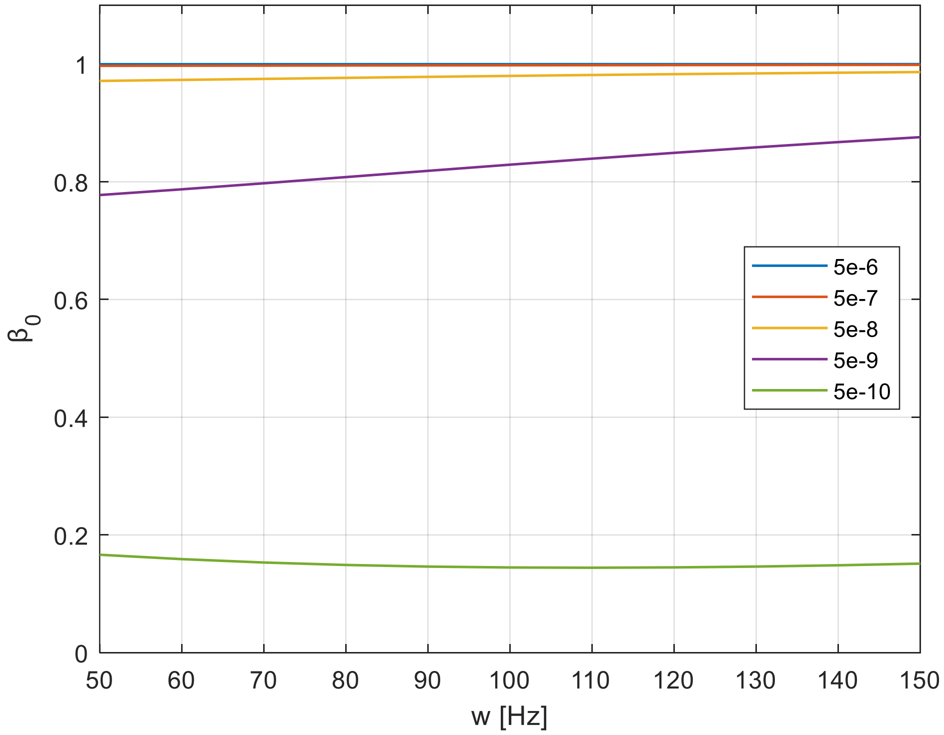

Fig. 5-27 Evolution of β_0 with frequency for different values of C_{seal}. In the legend C_{seal}.in $\left[\frac{m^3}{sPa}\right]$

In a second phase the presence of the sealing device, together with the feeding system was investigated. A feeding coefficient and feeding pressure were selected and the effect of the different sealing coefficients were tested at different frequency. In Fig. 5-28, the evolution of the adimensional exiting flow rate is shown. The data are referred to $\omega = 110\ Hz$. It is possible to see that the reduction of the outflow is higher if the feeding system is modelled together with the sealing one. The reason is quite obvious. When the feeding orifices are added in the geometry, a rise in the pressure evolution is registered in their proximity. This alteration of the pressure evolution affects the pressure distribution on the whole axial evolution of the damper, resulting in a reduction of the positive pressure gradient at the extremities.

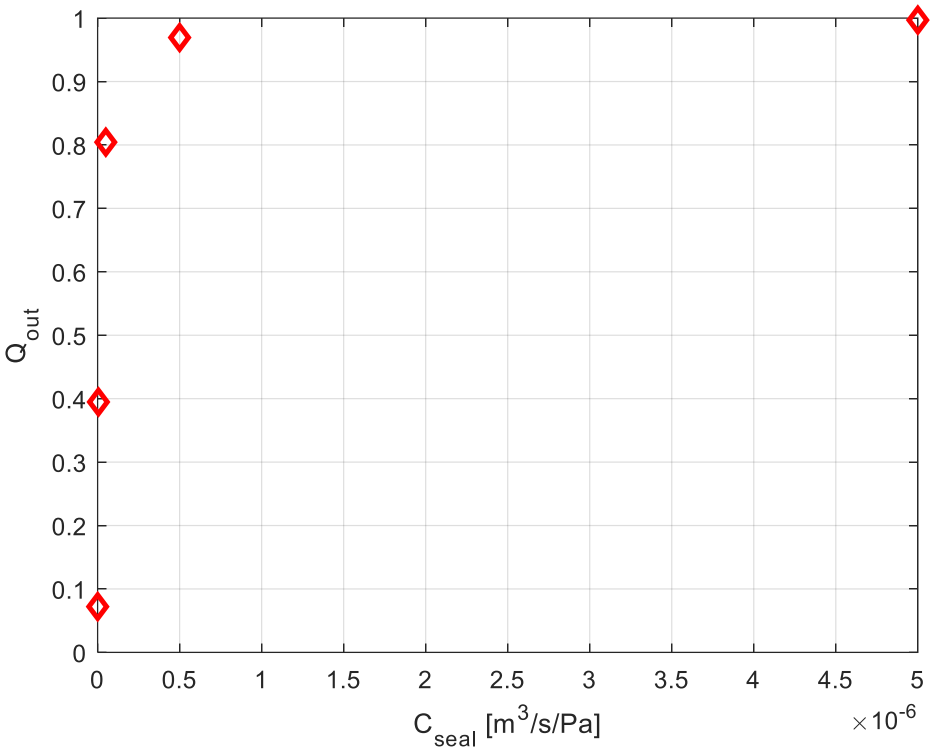

Fig. 5-28 Evolution of adimensional outflow with end seal coefficient. With addition of feeding system

As reported in the previous chapters, the introduction of the feeding systems determines a dependency of the mass coefficients with the frequency. The direct one tend to increase with ω until an asymptote is reached. If the sealing device is introduced, the opposite trend is registered. The mass coefficient is higher at the lower frequency and decrease to reach an asymptote when ω is increased. In Fig. 5-29, the evolution of the adimensional mass coefficients with the frequency, for different values of C_{seal} is shown. Only for $C_{seal} = 5 \times 10^{-6}$ the trend of the mass coefficient with the frequency is the same of the open-ends configuration.

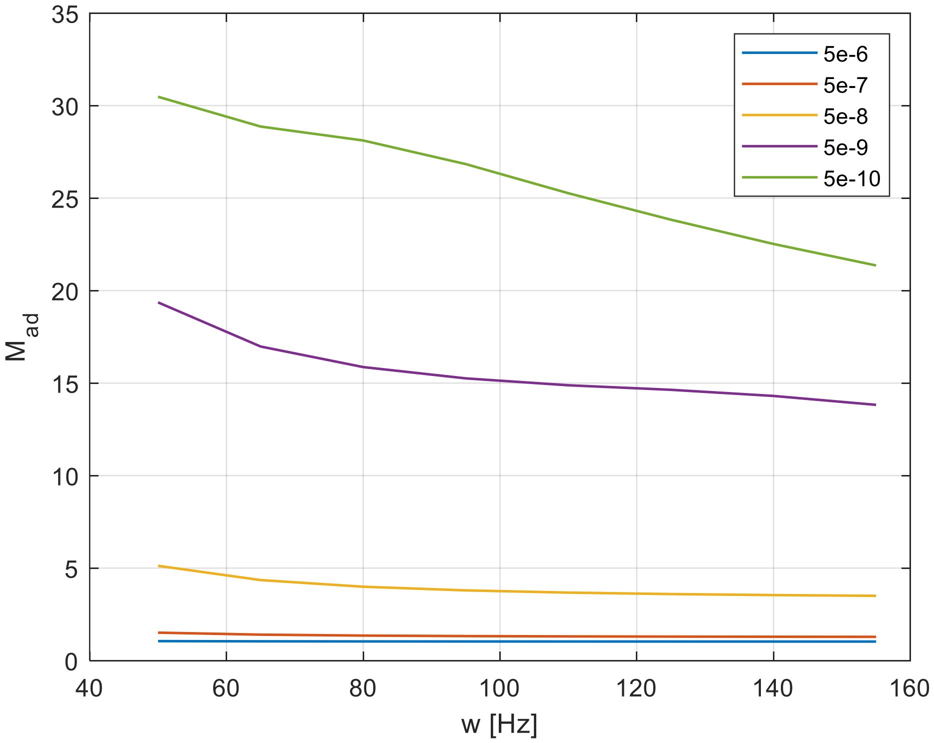

Fig. 5-29 Evolution of adimensional mass coefficient with the frequency for different C_{seal}. With addition of feeding system. In the legend C_{seal}.in $\left[\frac{m^3}{sPa}\right]$

As always, the damping coefficient remains constant with the frequency and is only influenced by the sealing coefficient. In Fig. 5-30, the evolution of the adimensional damping force coefficient with the sealing coefficient is shown. It is interesting to see that Fig. 5-26 and Fig. 5-30 are similar. However, as shown in a previous chapter, the coefficients obtained with the feeding system are, in modulus, lower than the ones obtained if the feeding system is not modeled.

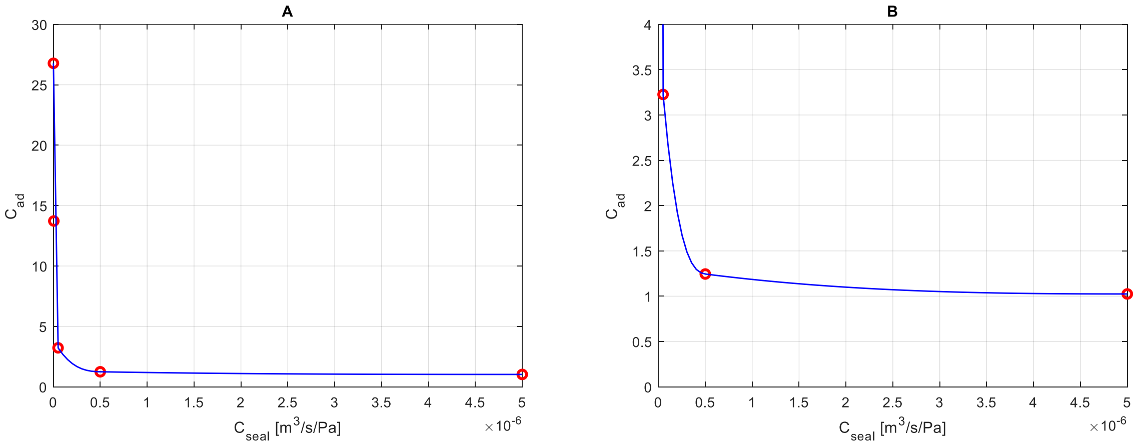

Fig. 5-30 Evolution of adimensional damping coefficient with C_{seal} (A) and magnification (B). With feeding system

In Fig. 5-31, the evolution of β_0 with the frequency, for different values of the sealing coefficient is reported. The data are divided by the values of β_0 in open-ends configuration. It is interesting to see that, if $C_{seal} > 5 \times 10^{-7}$, Fig. 5-31 and Fig. 5-27 shows similar results. On the contrary the results obtained with the lower sealing coefficients are quite different. It is important to specify that the configuration corresponding to the lowest C_{seal} is considered extreme and investigated only for completeness.

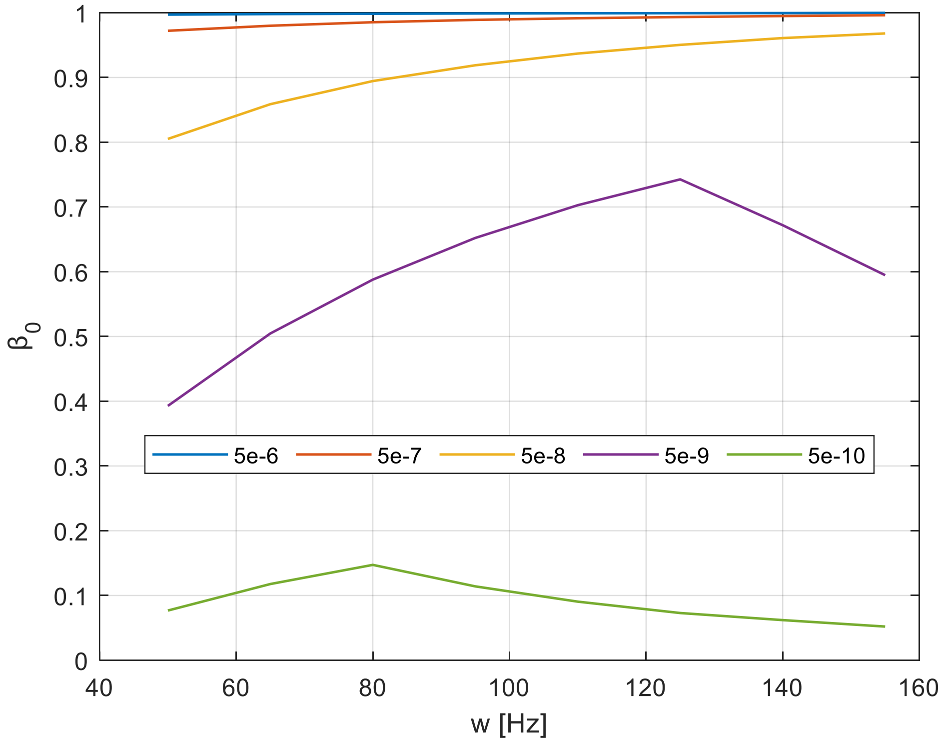

Fig. 5-31 Evolution of β_0 with frequency for different values of C_{seal}. With feeding system.

5.7. Effect of central groove

In this section the force coefficients obtained for damper B in open ends configuration are compared with the ones obtained with a damper with the same land length but without the central groove. In order to facilitate the comparison, the simpler damper is not simulated taking into consideration the feeding system. For comparison purpose, the results shown are obtained at $\omega = 100\ Hz$. In Fig. 5-32, it is possible to see the comparison of the adimensional mass and damping coefficients. The results of both dampers were divided by the normalizing parameters presented in [49]. It is possible to see that the damping coefficients have similar evolutions with the static eccentricity. On the contrary the mass coefficients for the plain geometry are almost ten times lower than the ones obtained with the geometry with the central groove. The addition of the groove determines the presence of a region in the damper where the Reynolds number is higher. In the groove area the effect of the inertial term is much more important than in the rest of the damper. The increase of the inertial effect corresponds Both geometries are simulated without taking into consideration the air ingestion.

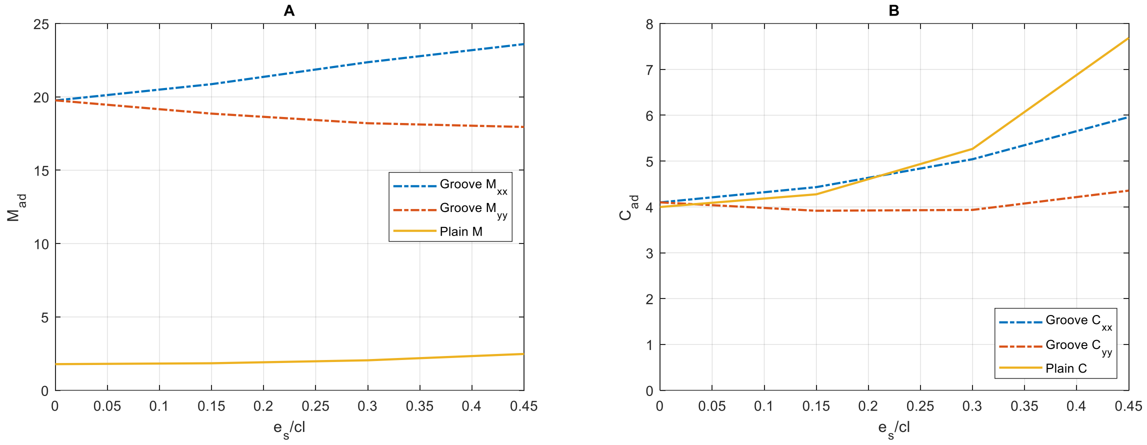

Fig. 5-32 Adimensional mass (A) and damping (B) coefficients with static eccentricity. Results for plain damper and damper with central groove

6. MODEL APPLICATION

In this paragraph the model for the SFD force coefficients is integrated in the finite element analysis of a centrifugal compressor. The shaft of the machine is long 0.7 m and the nominal diameter is 50 mm. The impeller is 70 mm long and has a maximum diameter of 140 mm while the minimum one is 33 mm. In Fig. 6-1, it is reported the finite element discretization of the structure.

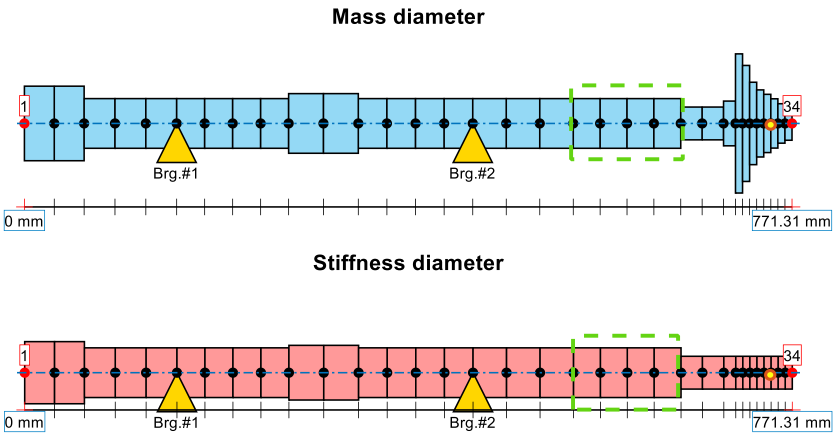

Fig. 6-1 Finite element discretization of the machine

In total 34 nodes are considered. As shown above, the stiffness and mass diameter are different for the different elements. The yellow triangles represents the two roller element bearings. The green rectangle represents the region where a sealing element is placed. As forcing mechanism, an unbalance is placed in the yellow node of the impeller.

In Fig. 6-2, the three-dimensional representation of the compressor model is shown.

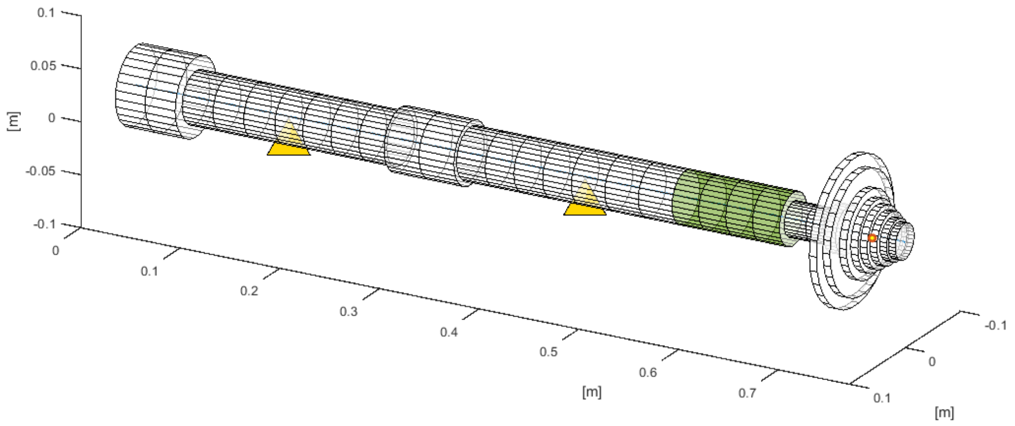

Fig. 6-2 Three-dimensional representation of the model

6.1. Vibration reduction

At first the effect of the seal is not taken into consideration while the attention is focused on the reduction of the vibration of the machine, focusing on the impeller. The operational frequency range of the compressor goes from $0-300\ Hz$ and $200\ Hz$ is considered as the operating frequency. In Fig. 6-3, the forced response to the unbalance at three nodes of the impeller are reported. It is possible to see that, due to the characteristics of the bearings, the system is barely damped and when crossing the natural frequency, at 186 Hz, the vibration's amplitude is, in the last node, higher than $2 \times 10^{-4}\ mm$. Due to the small gaps between the impeller and the cage and to reduce the aerodynamic losses, it is important to reduce as much as possible the level of the vibration.

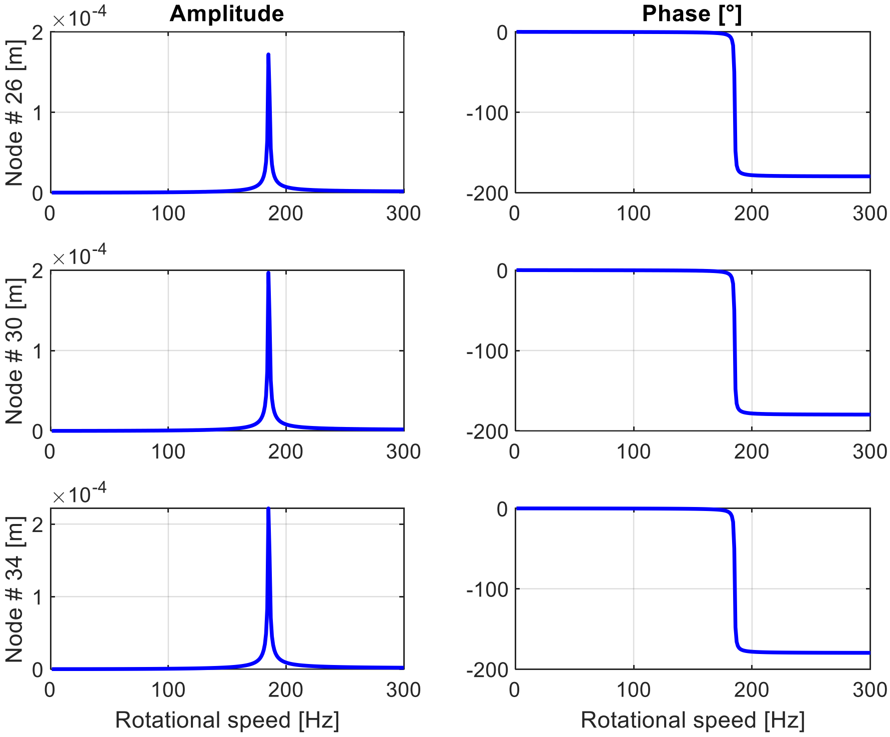

Fig. 6-3 Amplitude and phase of vibration at nodes 26, 30 and 34

For what regards the vibration amplitude at the operating frequency, it assumes values between $7-9 \times 10^{-6}\ m$.

In Fig. 6-4, the Campbell diagram is reported. It is possible to see that the natural frequencies remain similar for the whole operational range This is determined by the low level of structural damping and by the small inertia of the impeller that limits the gyroscopic effect.

In order to reduce the oscillation peak at resonance, a SFD is introduced to add damping. To do so, a supporting structure is needed for the damper. One of the most used techniques in the industry contemplates the use of a squirrel cage. As it is possible to see from Fig. 6-5, the squirrel cage connects the damper to the static structure and is used as a centering mechanism. The whole structure is modeled as a pedestal. A node is added and connected to the node of the bearing to the left with the bearing stiffness. The mass of the bearing, the damper and the cage are concentrated in this new node. The pedestal node is then connected to the ground with the stiffness of the squirrel cage which is considered two orders of magnitude smaller than the one of the bearing.

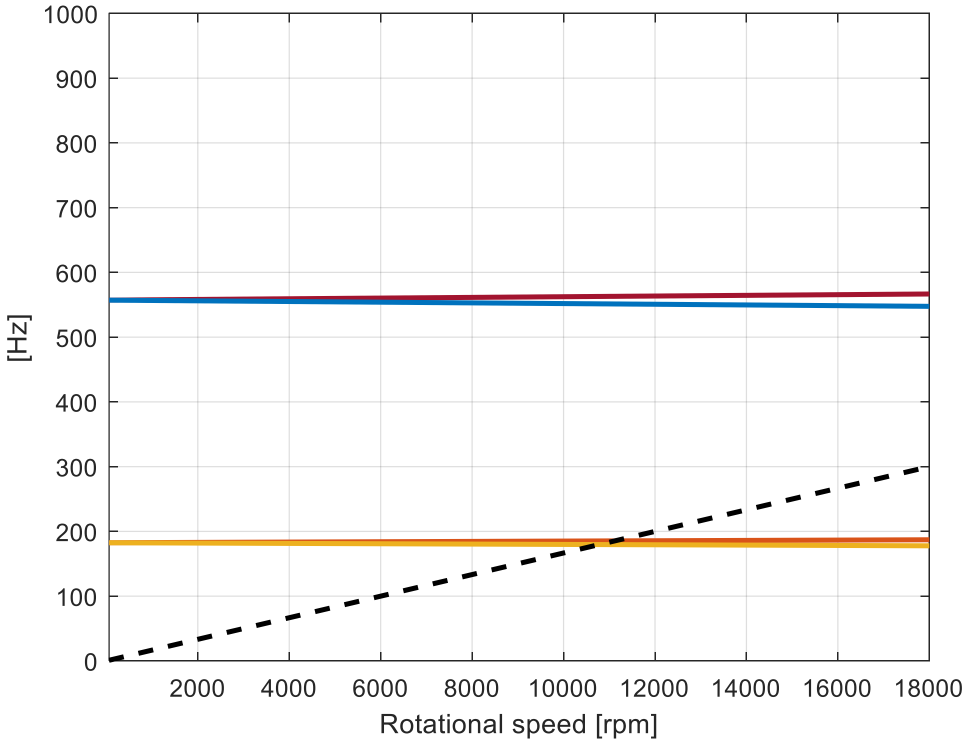

Fig. 6-4 Campbell diagram of model 1

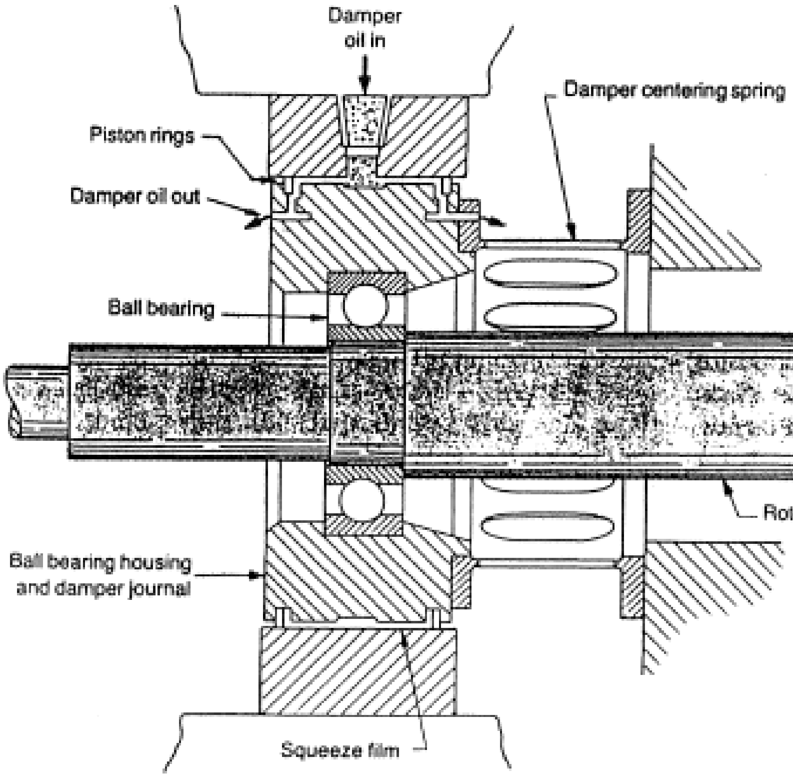

Fig. 6-5 Example of SFD supported with a squirrel cage, called damper centering spring in the figure. From [1]

In Fig. 6-6, it is possible to see the new model of the structure. The mass of the cage is added to the bearing together with the mass coefficient that is developed by the SFD when the shaft vibrates. The structure is then connected to the ground with the cage stiffness and the motion is damped by the damping coefficient developed by the damper. For brevity only the representation of the mass diameter is reported.

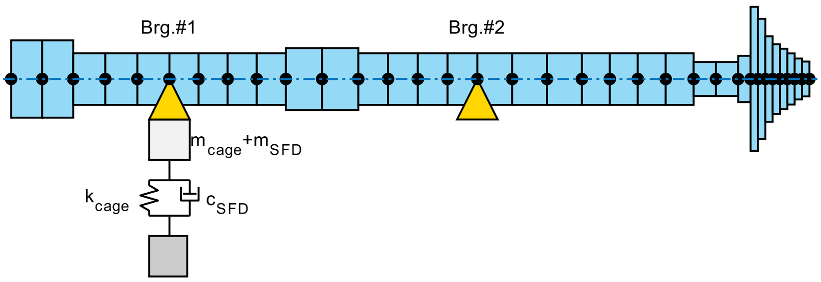

Fig. 6-6 Finite element discretization with squirrel cage

At first the results obtained with the dry damper, i.e. no oil, are shown. Due to the lower overall stiffness the natural frequencies are lower. In Fig. 6-7, it is possible to see the forced response to the unbalance at the three nodes of the impeller. Two resonance peaks are present, one at 161 Hz and the other at 254 Hz.

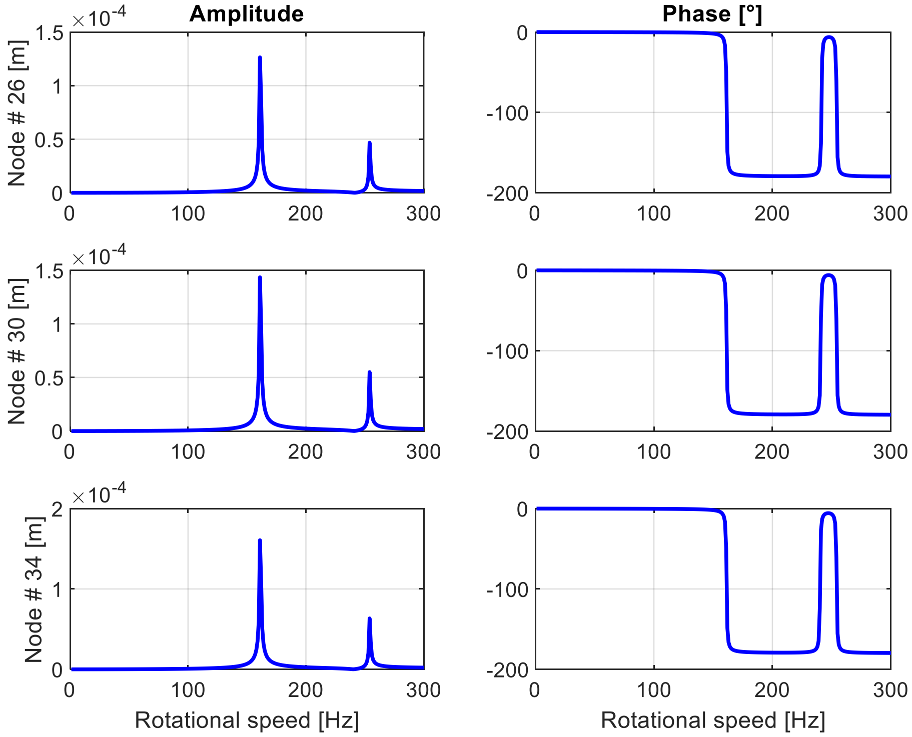

Fig. 6-7 Amplitude and phase of vibration at nodes 26, 30 and 34. Dry system

It is possible to see that, already with the addition of the squirrel cage, the main peak amplitude is reduced of almost 30%. Also the orbit vibration amplitude at the operating frequency is reduced. When the SFD without oil is applied the vibration at 200 Hz is almost three times less than before.

The SFD tested has the following characteristics:

$D = 100\ mm$
$L = 25\ mm$
$cl = 300\ \mu m$

Table 6-1 SFD geometric characteristics

For simplicity a plain damper without grooves, feeding system and seals is considered. The oil used in the model is ISO VG 46 oil with a density of $870 \frac{kg}{m^3}$ and a viscosity of $0.0383\ Pa \cdot s$. The clearance was chosen taking into consideration the forced response to the unbalance of the pedestal node shown in Fig. 6-8. For safety reasons, the clearance chosen is almost five times the maximum amplitude at dry conditions.

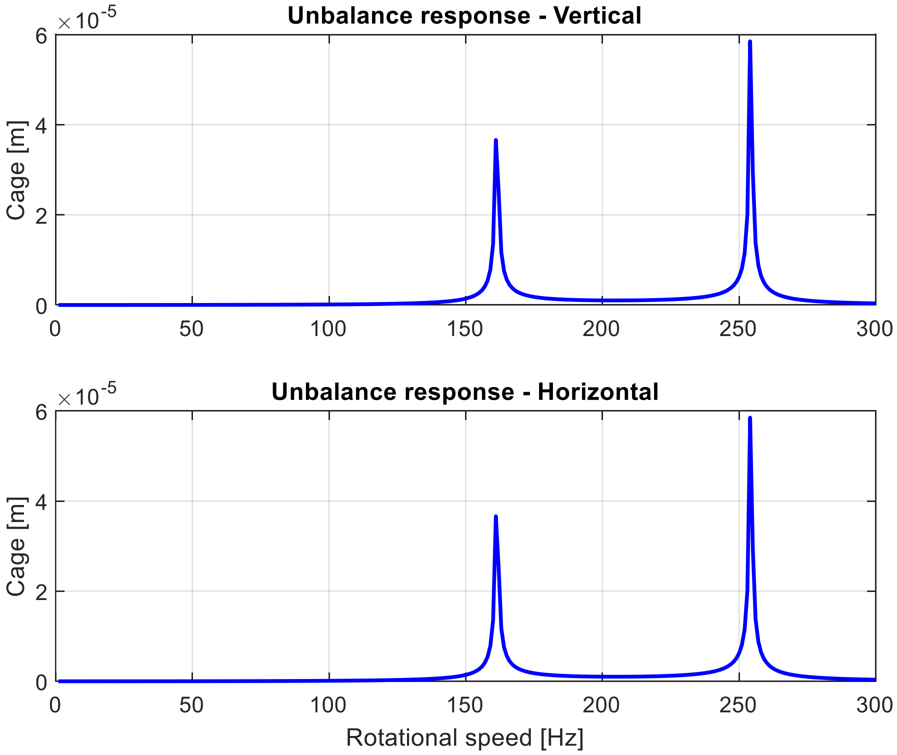

Fig. 6-8 Amplitude and phase of vibration at pedestal node. Dry system

Once the geometry of the damper is selected, the force coefficients for all the frequencies and orbit radius are obtained. CCOs are considered. The new damping and mass coefficients are added in the finite element model and the new orbit radius are evaluated. This procedure is repeated until convergence on the orbit radius is obtained.

In Fig. 6-9, the forced response to the unbalance at the impeller nodes, with the oil addition, is shown. It is possible to see that the result is much different from Fig. 6-7. The first peak disappears in the amplitude graph but a phase change is present at 90 Hz The second peak is shifted at a lower frequency, close to the one of the model without the SFD. It is possible to see that a reduction on the peaks is obtained with the introduction of the squeeze film damper.

To establish the effectiveness of the damper, the forced responses to the unbalance of the model without the damper are compared with the ones shown in the following figure. It is possible to see that the resonance peaks are slightly reduced and shifted to the right, see Fig. 6-10.

In Fig. 6-11, the ratio between the resonance peaks at the impeller nodes for the model with and without the SFD is shown. With this SFD configuration the peaks are reduced of almost 17%. It can be considered an interesting result since no optimization on the damper geometry is performed.

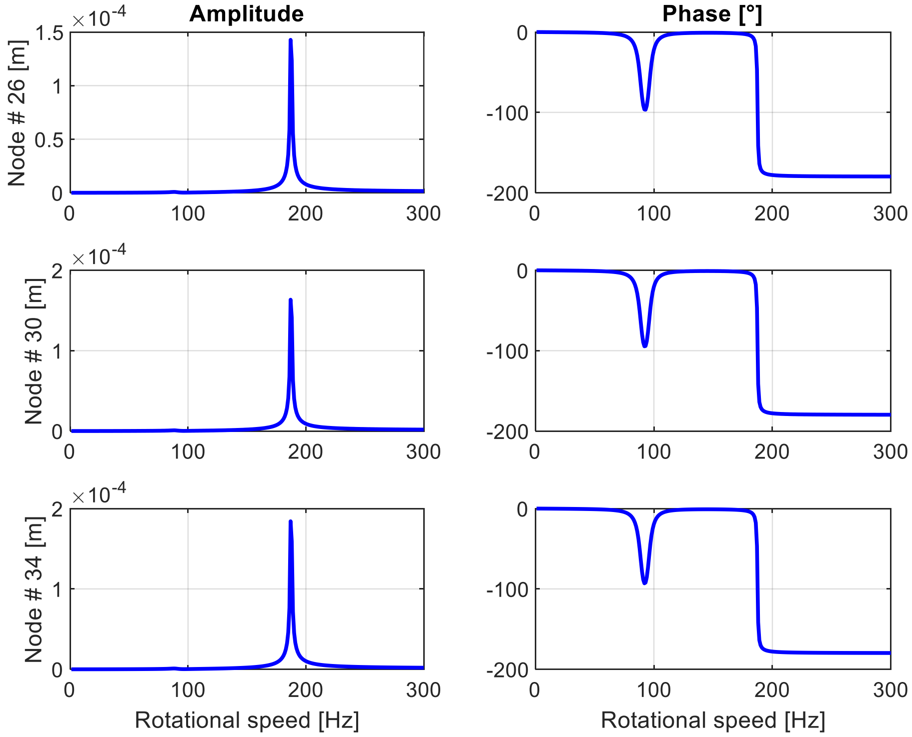

Fig. 6-9 Amplitude and phase of vibration at nodes 24, 30 and 34. Lubricated system

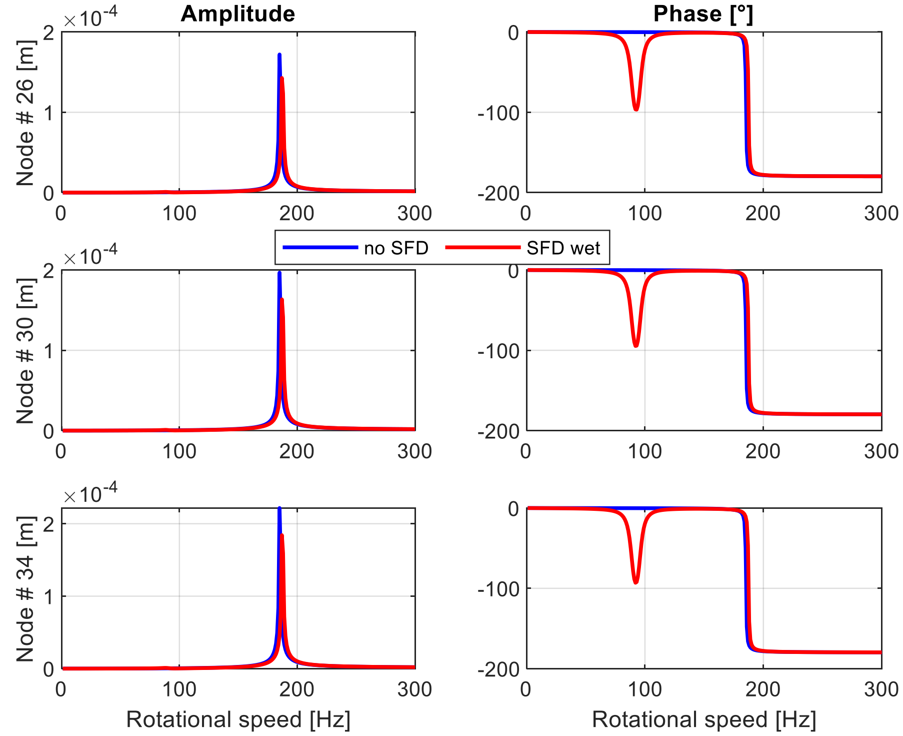

Fig. 6-10 FRF amplitude and phase for model 1 and model 2 with active SFD

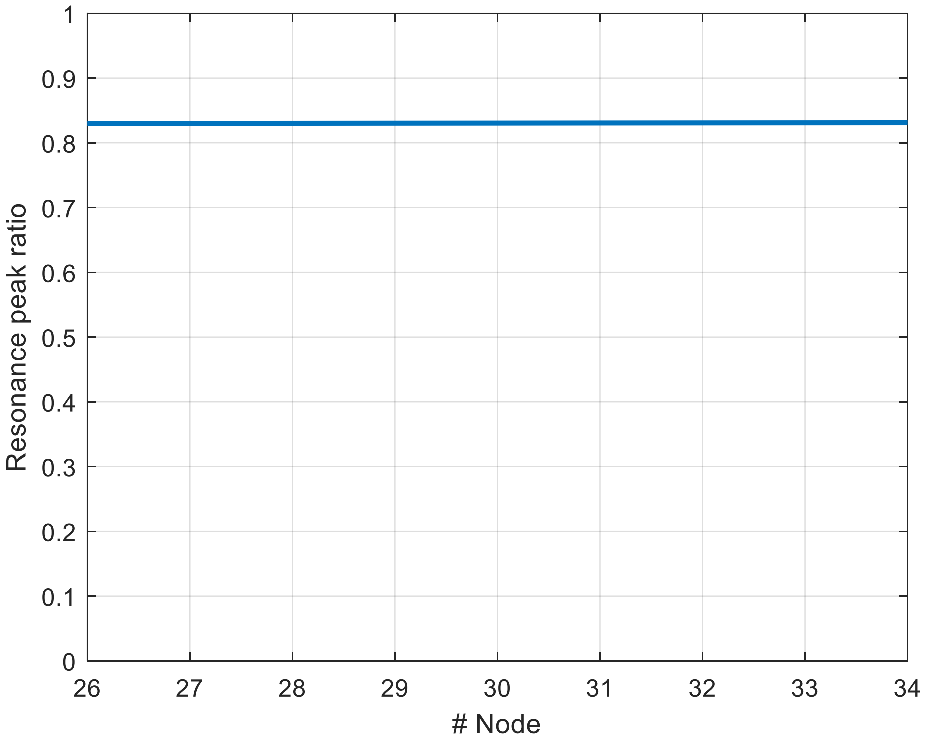

Fig. 6-11 Amplitude peaks ratio at impeller nodes

In Fig. 6-12, the orbit radius at the working rotational speed of the impeller nodes are reported. As it was stated above, in the dry condition the orbit radius are much lower. In the wet condition an increase of the radius is reported. The reason why in the dry condition the orbit radius is strongly reduced is because at the reference frequency the system works in between two natural frequencies. On the contrary the orbit radius for the wet configuration is increased because the natural frequency is slightly higher than the one of the undamped configuration and so closer to the operating frequency.

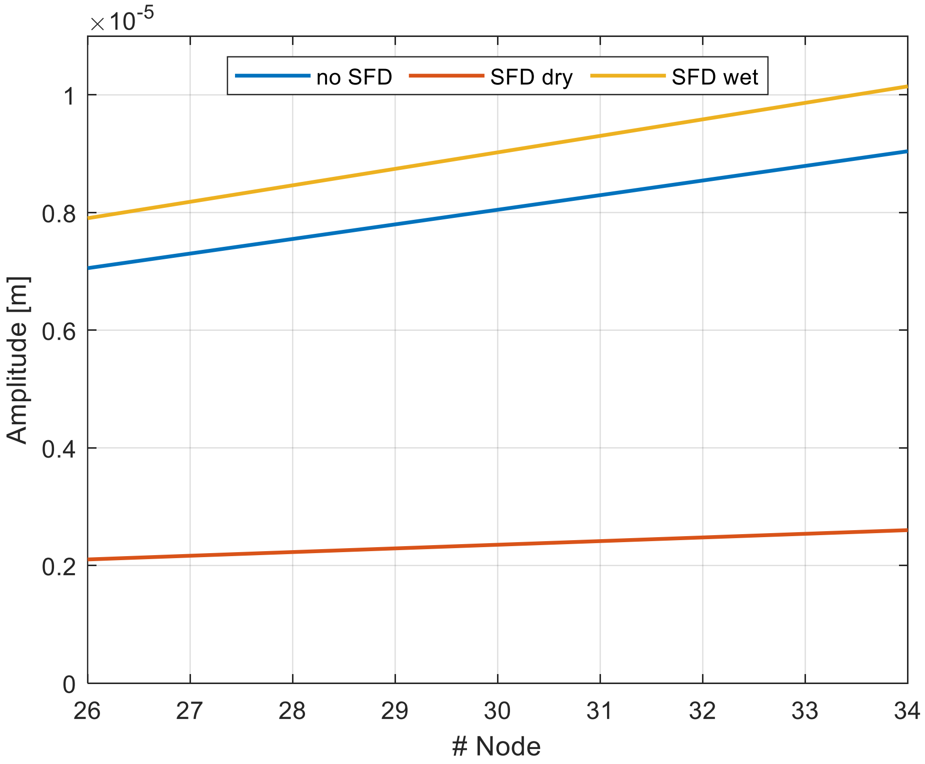

Fig. 6-12 Orbit radius of impeller nodes at rotational frequency $200\ Hz$

In Fig. 6-13, the Campbell diagram of the damped configuration is reported. The green line, not present in Fig. 6-4, corresponds to the mode added to the system with the cage introduction. This mode is responsible of the first amplitude peak in Fig. 6-7 and Fig. 6-8. The natural frequencies decrease with the rotational speed. This behavior can be explained with the addition of the damper coefficients.

In order to see if a different geometry for the damper is more effective, two other configurations were tested. One with $cl = 0.5\ mm$ and one with $cl = 0.2\ mm$. In the first case both the damping and force coefficient are lower than the reference case. In the second one, both force coefficients assume larger values. In Fig. 6-14, it is possible to see the values of both force coefficients with the clearance.

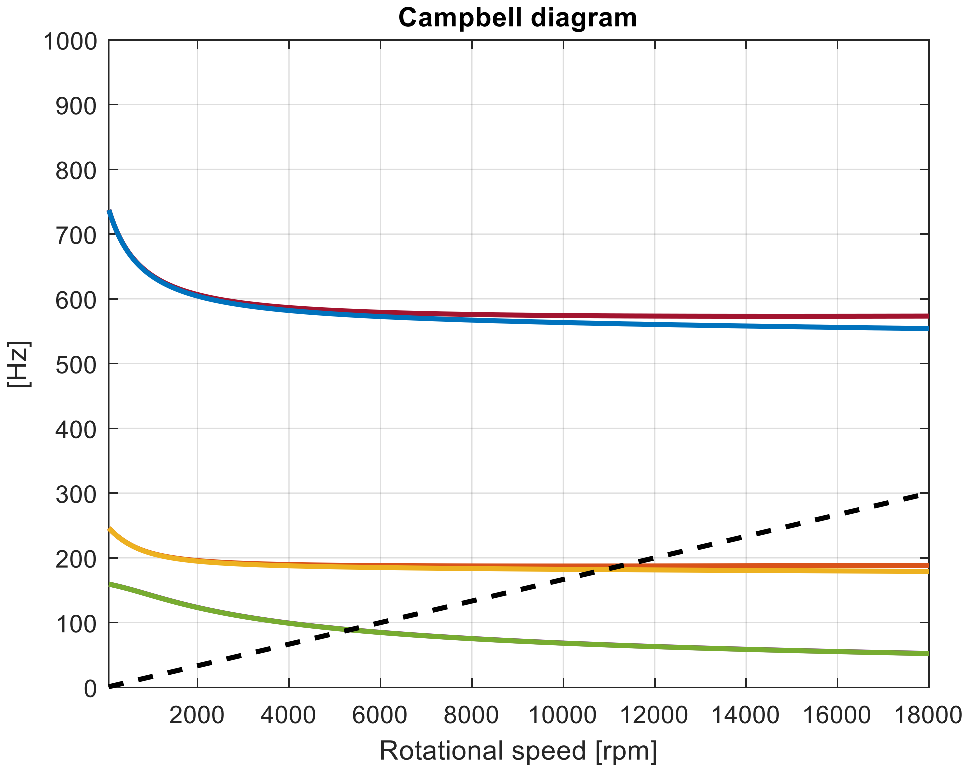

Fig. 6-13 Campbell diagram of model with SFD

In Fig. 6-15, the evolution of the resonance peaks amplitude ratio, at the impeller nodes, for the three configurations is reported. It is interesting to see that the damper with the largest clearance has a detrimental effect in the reduction of the vibrations. It is also interesting to see that the damper with the highest damping coefficient is less effective than the reference one. It is evident that the choice of the squeeze film damper is not straightforward. Enough damping is needed but if the value of the damping coefficient is too high the SFD will be ineffective. It was also observed that the increase in the damping coefficient is effective until the value of the mass coefficient remains low. The strong effect that the mass coefficient has on the dynamic of the system complicates even more the damper selection.

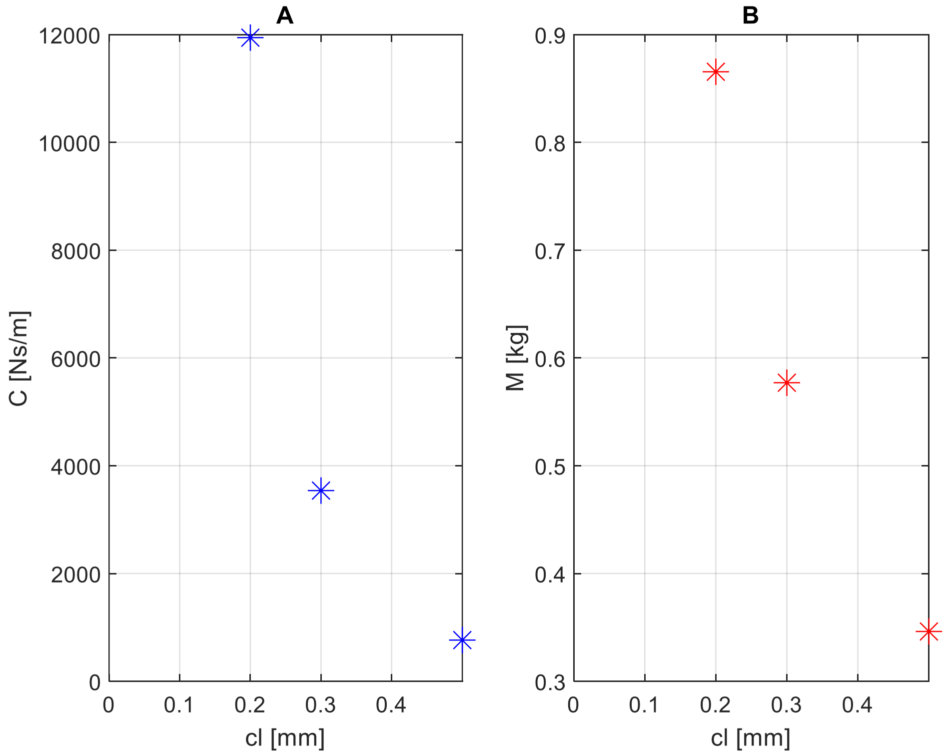

Fig. 6-14 Damping (A) and mass (B) coefficients evolution for the three SFD configurations

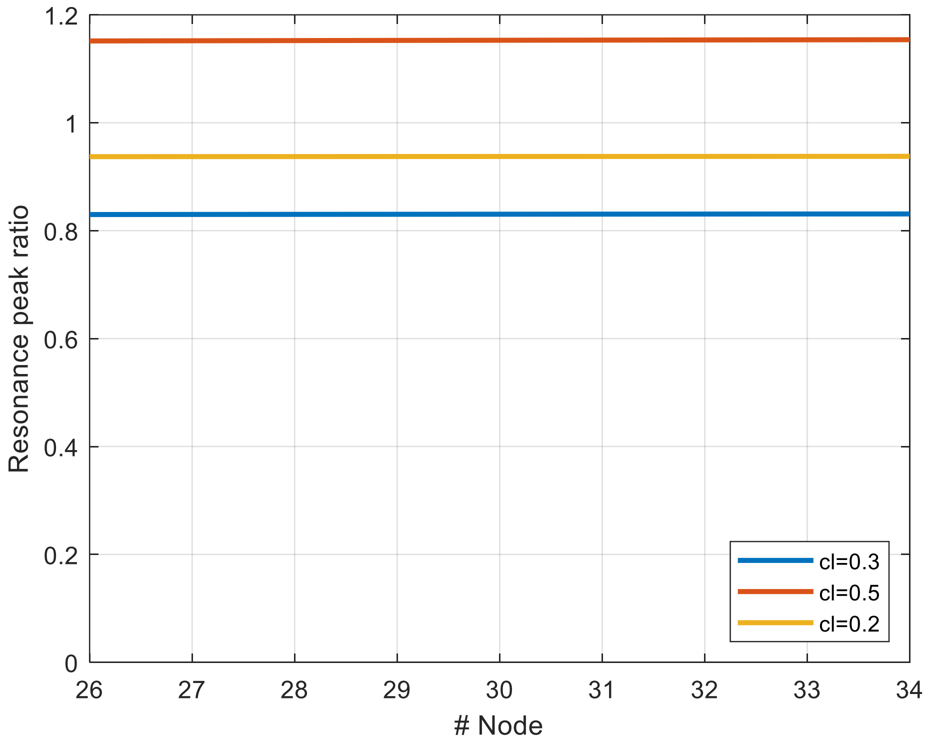

Fig. 6-15 Amplitude peaks at impeller nodes for the three SFD configuration. The damper clearance in millimeters is indicated in the legend

6.2. Instability correction

In this section the effect of the seal placed before the impeller is considered. It is well known that seals can be a source of instability. In order to simulate the presence of the instability, the stiffness matrix at the sealing nodes is considered as:

$$K_{seal} = \begin{bmatrix} 0 & k_{seal} \\ -k_{seal} & 0 \end{bmatrix} \tag{76}$$

The value of k_{seal} is varied in order to establish at which point the sealing presence destabilizes the system. In order to assess the stability of the system, the real parts of the eigenvalues must be checked. In Fig. 6-16, the maximum real part of the eigenvalues is plotted with growing k_{seal}. The first instabilities is encountered at $k_{seal} = 15000\,\frac{N}{m}$. However, it is at $k_{seal} = 17500\,\frac{N}{m}$ that the system is unstable for the whole frequency range. Until $k_{seal} = 35000\,\frac{N}{m}$ only the first eigenvalue has the positive real part, for higher levels of seal stiffness also the real part of the fifth eigenvalue is positive.

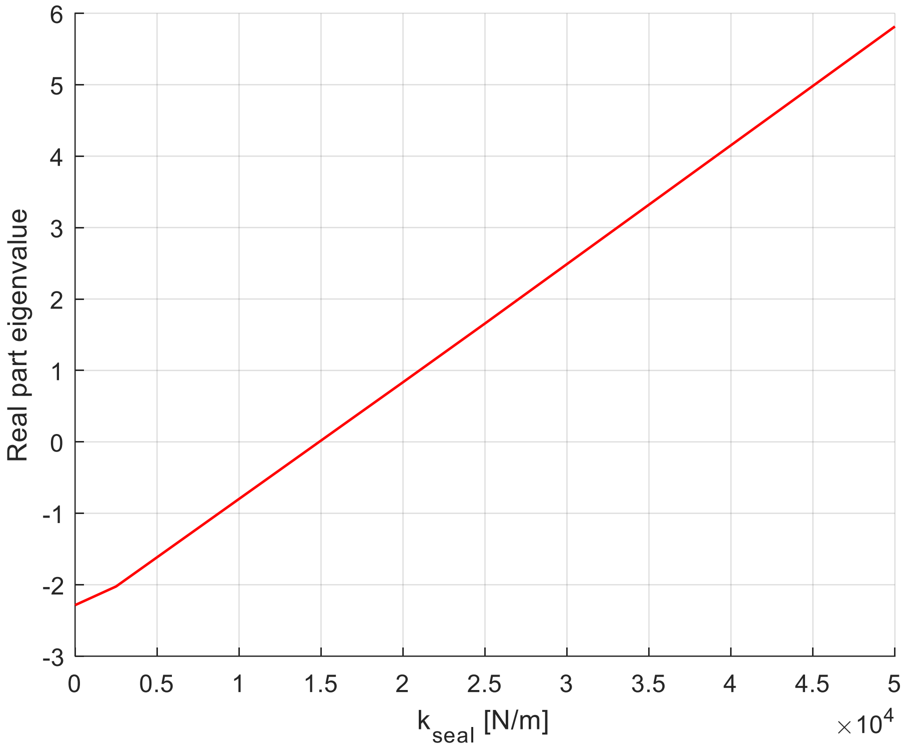

Fig. 6-16 Effect of k_{seal} on the real parts of damped eigenvalues

At first, we will concentrate on $k_{seal} = 17500\ N/m$ because at this value there is a positive damped eigenvalue for the whole frequency range. Theoretically, the addition of the squeeze film damper, should be able to stabilize the system, at least for a frequency range. The reason of the stabilizing effect stands in the introduction of damping that counterbalances the instability brought by the seal. Three different geometries were tested: two simple dampers with $cl = 0.5\,mm$ and $cl = 0.3\,mm$ and one with $cl = 0.4\,mm$ with sealing at the ends.

In Fig. 6-17, the effect of the damper with $cl = 0.5\,mm$ is reported. For convenience the dimensionless damping factor is displayed as indicator for stability. This coefficient is defined as

$$\eta_i = -\frac{Real(\lambda_i)}{Imag(\lambda_i)} \tag{77}$$

Where λ_i is the eigenvalue. When η is positive it means that the i-th mode of the system is unstable.

In Fig. 6-17, the dimensionless damping factor of the first eigenfrequency is reported for the model without the damper together with the values for the first and third eigenfrequencies for the model with the SFD. It is possible to see that the dimensionless damping coefficient related to the first eigenvalue of the damped configuration assumes only positive values. On the contrary, the real part of the third eigenvalue has a shift in sign at around 180 Hz. So this damper configuration is able to stabilize the system up to this frequency.

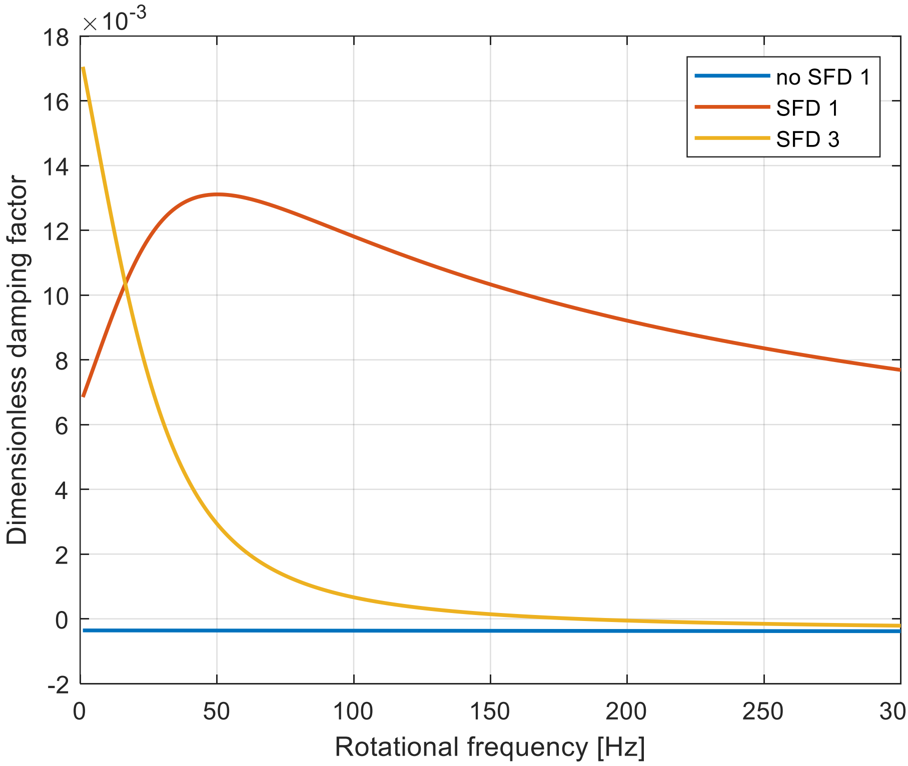

Fig. 6-17 Dimensionless damping factor of first and third eigenvalue for system with SFD of $cl = 0.5\,mm$ and first eigenvalue for system without damper

The fact that the eigenvalue assuming positive values of the real part changes is no mistake. The introduction of the squirrel cage introduces two new degrees of freedom and so two new eigenmodes and eigenvectors. The unstable mode of the model without the SFD should remain the same also after the damper is added to the system. In order to check this statement, the first and third modes at $200\,Hz$, for the damped and undamped system, are displaced in Fig. 6-18 and Fig. 6-19. It is possible to see that the first mode of the system without SFD has the same shape of the third of the system with the SFD so it is possible to say that the unstable mode remains the same after the squeeze film damper is added. The eigenfrequencies of the unstable mode are slightly different due to the introduction of the squeeze film damper.

In **Errore. L'origine riferimento non è stata trovata.**, the mass and damping c oefficients obtained with the different dampers are reported. As expected, the first one is the one with the lowest coefficients. The second guarantees a damping coefficient almost five times the first one while the mass coefficient is less than double. The configuration with the sealed ends produces both mass and damping coefficients one order of magnitude higher than the ones obtained with the geometry with $cl = 0.5\ mm$. All dampers have the same diameter and length of the one adopted in the previous chapter. For the oil properties refer to the previous chapter.

	$cl = 0.5\ mm$	$cl = 0.3\ mm$	$cl = 0.4\ mm$
$M\ \left[\frac{N}{m}\right]$	0.346	0.577	2.733
$C\ \left[\frac{Ns}{m}\right]$	764.376	3538.780	9428.879

Table 6-2 Mass and damping coefficients of the three dampers tested to solve instability

Just looking at the values of the table we would expect the sealed damper to be the most effective and the first one the less effective. However, as shown in Fig. 6-20, the most effective geometry is the one with $cl = 0.3\ mm$ that is able to guarantee stability up to $200\ Hz$. On the contrary, the sealed damper configuration revealed to be the less effective. As it was observed in the chapter on the vibration reduction, the increase in the damping coefficient has a positive effect if the mass coefficient growth is limited. Moreover, if the damping coefficient is too high, its effect is the opposite of the desired one. In this case the stabilizing effect of the sealed damper is less than half of the two other dampers.

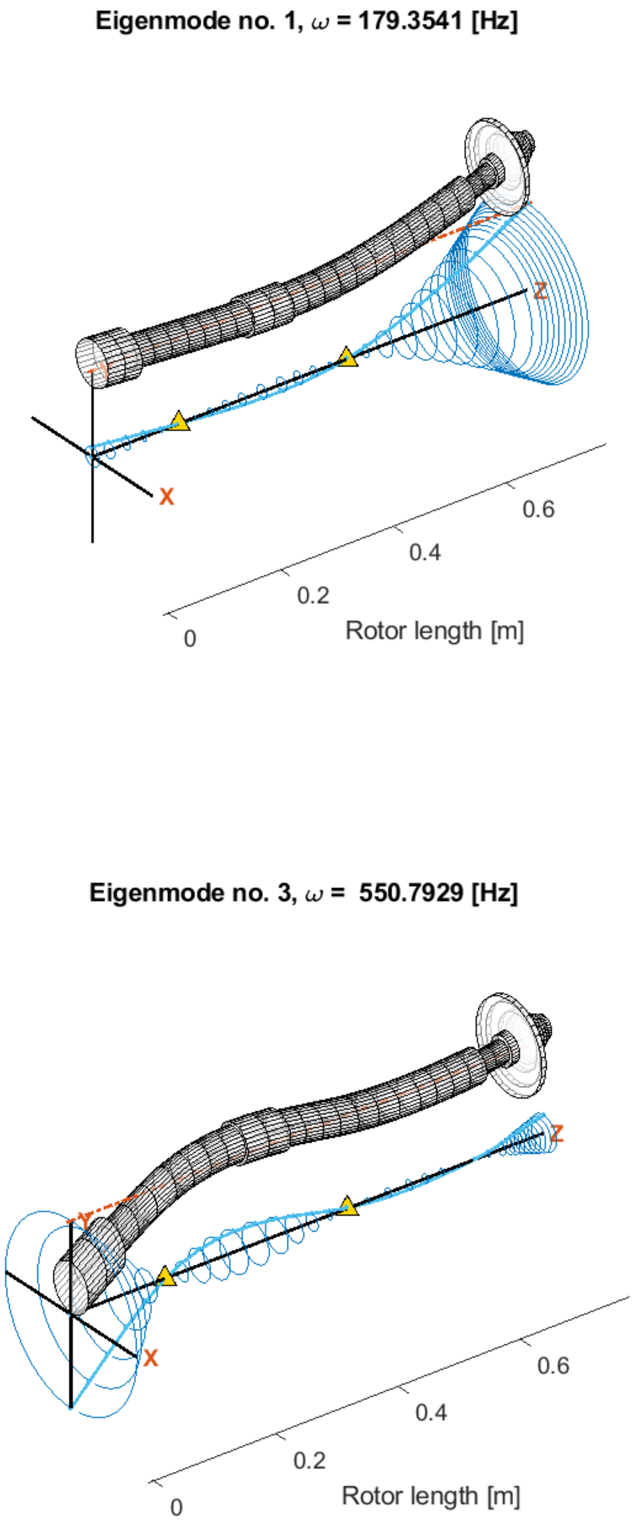

Fig. 6-18 First and third modes for model without SFD

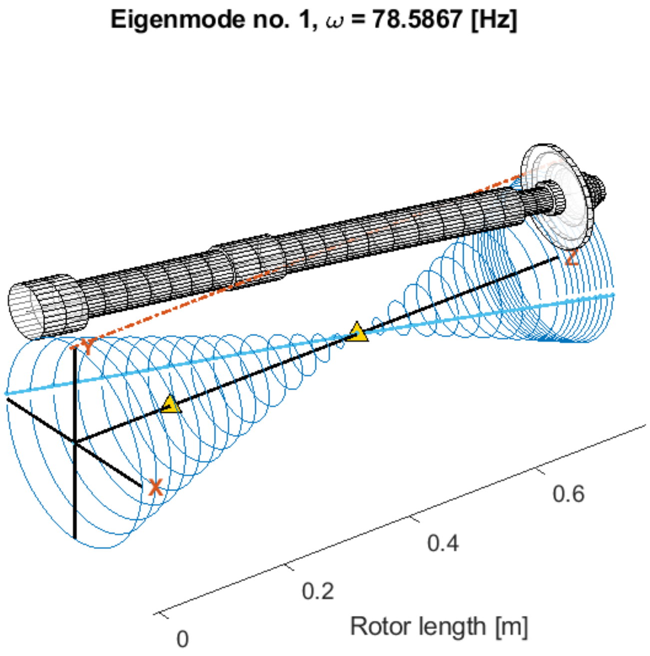

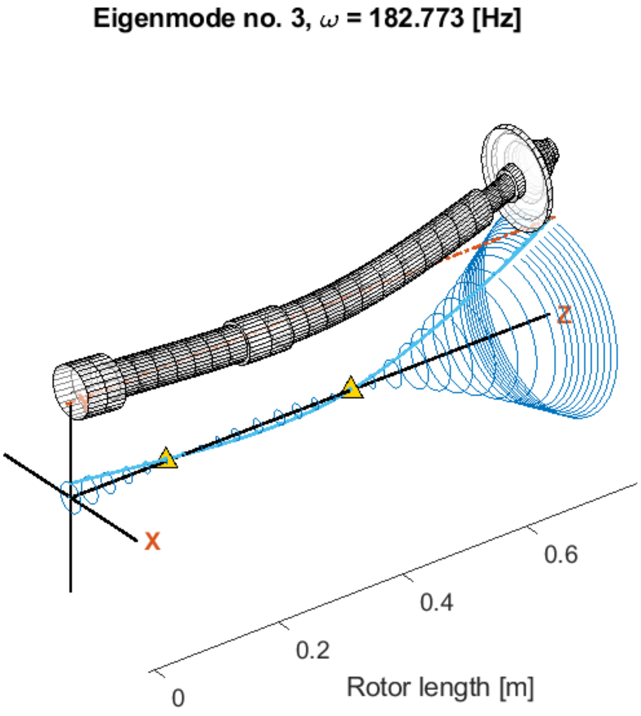

Fig. 6-19 First and third modes for model with SFD

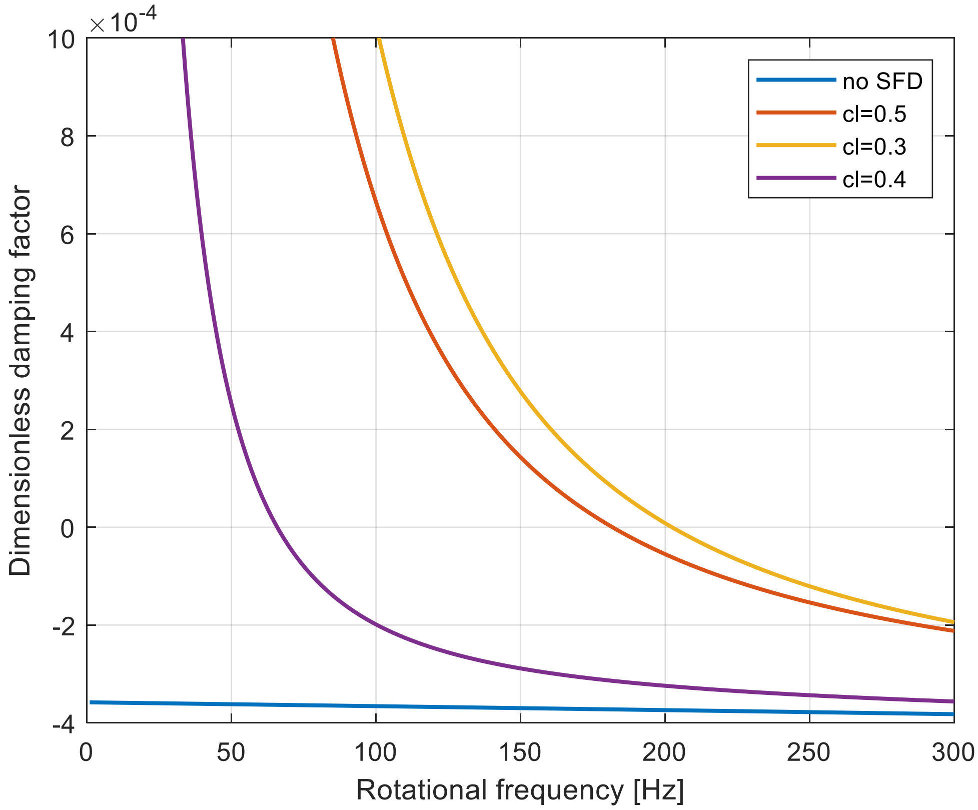

Fig. 6-20 Evolution of dimensionless damping factor for the system without SFD and the system with the three different SFD configurations

Now the damper with $cl = 0.3\,mm$ is tested in a much critical condition for what concerns the instability. The instability factor is set to $k_{seal} = 40000\,N/m$ so to have two eigenvalues with the positive real part. In Fig. 6-21, the evolution of the dimensionless damping factors with and without the damper are shown. In the configuration without the SFD, the eigenvalues with a positive real part are the first and the fifth. On the contrary, in the damped configuration, those eigenvalues have a negative real part. The unstable modes are the third and the seventh. As for the previous case, when the damper is added, the system is stable at low frequencies and becomes unstable when the rotational speed is increased. In this case the system remains stable up to 65 Hz. For higher frequencies the real part of the third eigenvalue has a positive sign.

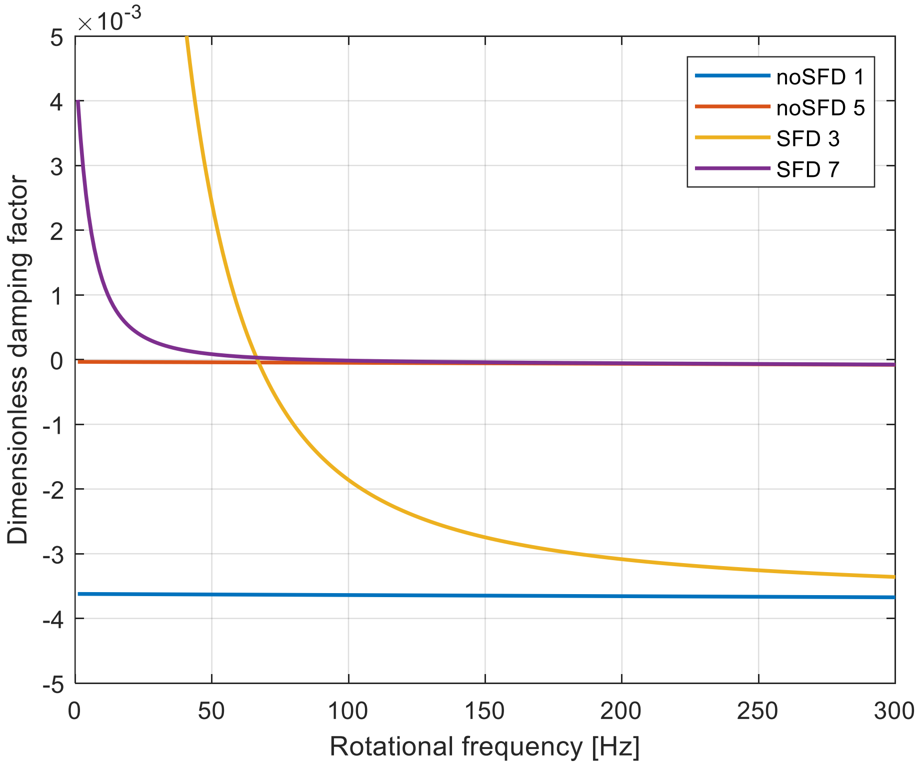

Fig. 6-21 Dimensionless damping factor of mode 1 and 5 for configuration without SFD and mode 3 and 7 for configuration with SFD

As it was reported above, the changement of the number of the unstable modes is determined by the addition of the two degrees of freedom with the cage. In Fig. 6-22, the first and fifth modes of vibration of the system without SFD are shown. In Fig. 6-23, the third and seventh vibration modes for the system with the SFD are shown. It is possible to see that the shapes for both the eigenmodes are the same Thanks to this observation it is possible, once again, to assert that the modes responsible for the instability have the same shapes before and after the addition of the SFD and the supporting cage.

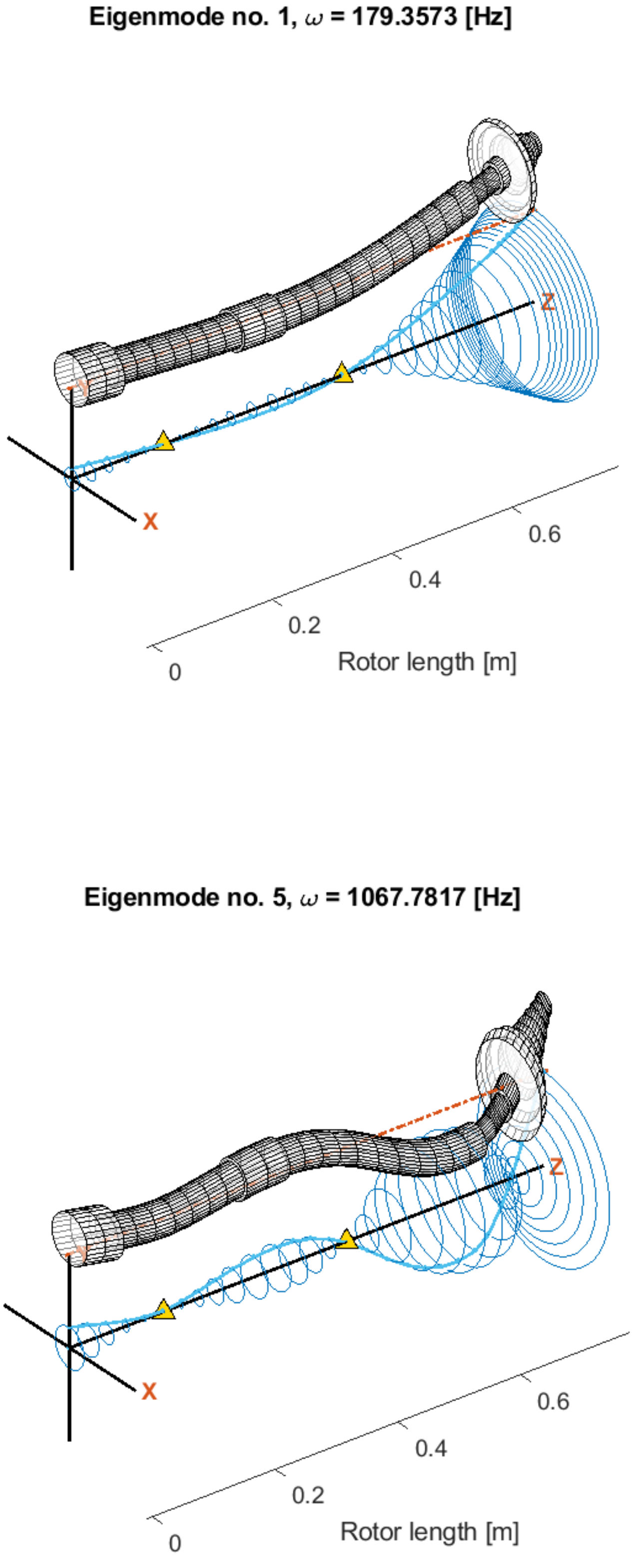

Fig. 6-22 Third and fifth vibrational mode of model without SFD

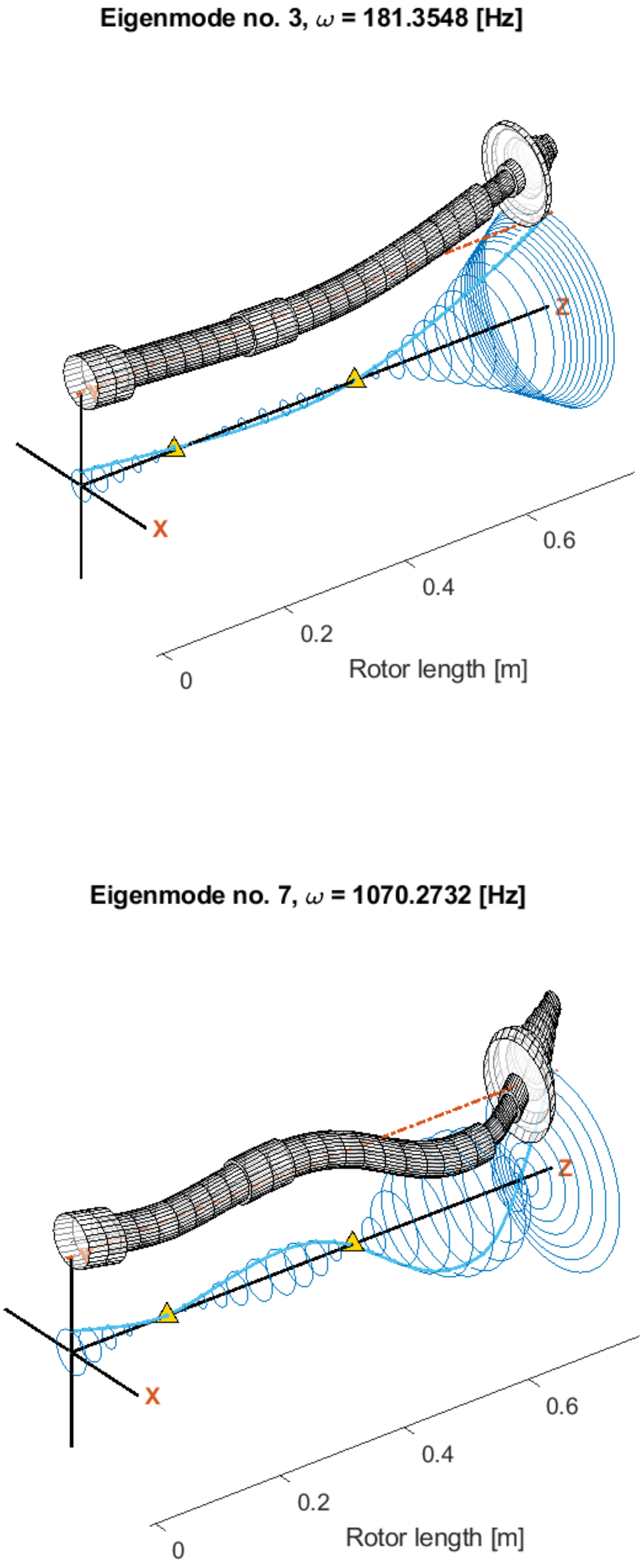

Fig. 6-23 Fifth and seventh vibrational mode of model with SFD

CONCLUSIONS

In this thesis, a model based on a Reynolds-like equation, is built to predict the behavior of squeeze film dampers. A term describing the temporal fluid inertia is added to the classical Reynolds equation. This term is considered fundamental to correctly predict the mass force coefficients developed by the dampers, especially if the clearance is large and feeding or end grooves are present. Different boundary conditions were investigated in order to simulate the feeding and discharge conditions. The system is discretized with a finite-difference approach and after the integration of the pressure field, derived from the equation mentioned above, the forces are obtained. A orbit-based model is then used to calculate the force coefficients.

Different models were tested to treat the vapor cavitation. Both the models, based on the linear complementarity, proved to be effective if the inertial term is left out from the equation. Unfortunately some numerical issues arise when the inertial term is added in the LCP modeling. The second-order derivative is responsible of the impossibility to use these cavitation models. A practical solution is achieved by setting to the cavitation value the pression in the cavitated region.

The air ingestion phenomenon is also modeled. Due to the positive pressure gradient at the axial ends of the damper, air is sucked inside the lands. The result is the formation of a bubbly mixture detrimental to the damping capacity of the SFD. The air volume fraction in the damper is used to calculate the mixture density and viscosity. A static form of the Rayleigh-Plesset equation is adopted to derive the distribution of the air content in the mixture starting from the reference value at the axial ends. This value is easily obtained once the pressure gradient at the open ends and the feeding flow rate are known.

Once the model has proven to be able to take into account all these issues, the effect of the different geometrical configurations, feeding mechanisms and sealing devices have been tested. In general it is possible to say that both force coefficients are increased when:

- the clearance is reduced;
- the damper's lands length is increased;
- the orbit radius and static eccentricity are larger;
- seals are placed at the discharge of the dampers;
- central grooves are added.

In order to simulate the presence of the grooves, their physical depth is substituted with an effective depth.

On the contrary, both force coefficients are reduced when:

- cavitation occurs;
- air ingestion occurs.

In general when the force coefficients grow, the risk of cavitation and the importance of the air ingestion are increased. The effect on the reference air volume fraction is also investigated for all the previous analysis, in order to see which are the most critical conditions.

The effect of the hole feeding system has been also investigated. In general, if vapor cavitation and air ingestion is not present, the force coefficients are constant with the vibration frequency. On the contrary, when the orifice presence is considered, there is a strong variation of the mass coefficient with the frequency.

Finally, the model is tested for the vibration control and the instability correction. In both cases, the addition of the damper to the original model resulted effective in the mitigation of the problem. Simple geometries were considered in this stage and it is not negligible that with a damper optimization, even better results could be achieved. However, the difficulty to tune the damper to its application is also exposed.

The model created is quick and reliable. It is able to simulate different operating conditions and geometries. However, as reported in the previous pages, the bi - dimensionality of the model is a strong limiting factor. It is believed that the key to obtain more precise results stands in the possibility to replicate the behavior of the oil in the feeding region, in the groove's region and at the discharge, especially if seals are applied. In order to do so, CFD or 3-D model based on the bulk-flow equation can represent the solution. However it is fundamental to keep in mind that higher accuracy always means higher computational time. It would be interesting to compare the results obtained from the model developed in this thesis, the results obtained with a three - dimensional model and experimental results for different geometrical configuration. This investigation could show the cases when the high accuracy of the 3-D models is required and when the simpler model can be considered enough. It is assumed that the level of accuracy of the model investigated in this work is enough for the first stage design of SFDs. It is in fact shown that better results are obtained than the ones available from the classical lubrication theory.

The second limiting factor of the model proposed is the impossibility to model the cavitation behavior when the effect of temporal inertia is taken into consideration. Unfortunately the LCP models found in the literature are all derived for oil film bearings applications, where the additional term of temporal inertia is not present. An improvement of the cavitation model would bring the accuracy of the model closer to the experimental results and the other 3-D models.

REFERENCES

[1] F. Y. Zeidan, L. San Andres, and J. M. Vance, "Design and Application of Squeeze Film Dampers in Rotating Machinery," in *Proceedings of the 25th Turbomachinery Symposium*, 1996, pp. 169–188, doi: https://doi.org/10.21423/R1694R.

[2] V. Iacobellis, K. Behadinan, D. Chan, and D. Beamish, "Experimental Investigation of the Effects of Squeeze Film Damper Design on Hoghspeed Rotor System," in *Proceedings of ASME Turbo Expo*, 2020, pp. 1–8.

[3] J. M. Vance, *Rotordynamics of turbomachinery*. 1988.

[4] B. Ertas, A. Delgado, and J. Moore, "Dynamic Characterization of an Integral Squeeze Film Bearing Support Damper for a Supercritical Co<inf>2</inf> Expander," *J. Eng. Gas Turbines Power*, vol. 140, no. 5, 2018, doi: 10.1115/1.4038121.

[5] E. J. Gunter Jr., L. E. Barrett, and P. E. Allaire, "DESIGN AND APPLICATION OF SQUEEZE FILM DAMPERS FOR TURBOMACHINERY STABILIZATION.," pp. 127–141, 1975.

[6] W. J. Chen, M. Rajan, S. D. Rajan, and H. D. Nelson, "OPTIMAL DESIGN OF SQUEEZE FILM DAMPERS FOR FLEXIBLE ROTOR SYSTEMS.," *J. Mech. Transm. Autom. Des.*, vol. 110, no. 2, pp. 166–174, 1988, doi: 10.1115/1.3258922.

[7] L. Della Pietra and G. Adiletta, "The squeeze film damper over four decades of investigations. Part I: Characteristics and operating features," *Shock Vib. Dig.*, vol. 34, no. 1, pp. 3–26, 2002.

[8] L. San Andres, "Squeeze Film Damper: Operation, Models and Theoretical Issues," in *Modern Lubrication Theory*, Texas A&M University, 2012.

[9] H. G. Elrod, "CAVITATION ALGORITHM.," *J. Lubr. Technol.*, vol. 103, no. 3, pp. 350–354, 1981, doi: 10.1115/1.3251669.

[10] M. Giacopini, M. T. Fowell, D. Dini, and A. Strozzi, "A mass-conserving complementarity formulation to study lubricant films in the presence of cavitation," *J. Tribol.*, vol. 132, no. 4, 2010, doi: 10.1115/1.4002215.

[11] L. Bertocchi, D. Dini, M. Giacopini, M. T. Fowell, and A. Baldini, "Fluid film lubrication in the presence of cavitation: A mass-conserving two-dimensional formulation for compressible, piezoviscous and non-Newtonian fluids," *Tribol. Int.*, vol. 67, pp. 61–71, 2013, doi: 10.1016/j.triboint.2013.05.018.

[12] A. Almqvist, J. Fabricius, R. Larsson, and P. Wall, "A new approach for studying cavitation in lubrication," *J. Tribol.*, vol. 136, no. 1, 2014, doi: 10.1115/1.4025875.

[13] L. San Andrés, S. Jeung, S. Den, and G. Savela, "Squeeze Film Dampers: An Experimental Appraisal of Their Dynamic Performance," in *Proceedings of Asia Turbomachinery Pump Symposium*, 2016.

[14] D. S., "Analysis of Force Coefficients and Dynamic Pressures for Short-Length

(L/D=0.2) Open-Ends Squeeze Film Dampers," Texas A&M Universiy, 2015.

[15] L. San Andrés and J. M. Vance, "Effects of fluid inertia and turbulence on the force coefficients for squeeze film dampers," *J. Eng. Gas Turbines Power*, vol. 108, no. 2, pp. 332–339, 1986, doi: 10.1115/1.3239908.

[16] L. A. S. Andres and J. M. Vance, "Effects of fluid inertia on finite-length squeeze-film dampers," *ASLE Trans.*, vol. 30, no. 3, pp. 384–393, 1987, doi: 10.1080/05698198708981771.

[17] S. Hamzehlouia and K. Behdinan, "Squeeze Film Dampers Executing Small Amplitude Circular-Centered Orbits in High-Speed Turbomachinery," *Int. J. Aerosp. Eng.*, vol. 2016, 2016, doi: 10.1155/2016/5127096.

[18] S. Hamzehlouia and K. Behdinan, "A study of lubricant inertia effects for squeeze film dampers incorporated into high-speed turbomachinery," *Lubricants*, vol. 5, no. 4, 2017, doi: 10.3390/lubricants5040043.

[19] T. Fan, S. Hamzehlouia, and K. Behdinan, "The effect of lubricant inertia on fluid cavitation for high-speed squeeze film dampers," *J. Vibroengineering*, vol. 19, no. 8, pp. 6122–6134, 2017, doi: 10.21595/jve.2017.19314.

[20] A. Delgado and L. S. Andrés, "A model for improved prediction of force coefficients in grooved squeeze film dampers and oil seal rings," *J. Tribol.*, vol. 132, no. 3, pp. 1–12, 2010, doi: 10.1115/1.4001459.

[21] F. Rodrigues, F. Thouverez, and L. Jezequel, "Interaction of Squeeze Film Dampers and Hole Feed Systems and Its Influence on the Dynamics of a Jeffcott Rotor.," *Int. J. Rotating Mach.*, vol. 10, 2004, doi: 10.1155/S1023621X0400017X.

[22] L. S. Andres and S.-H. Jeung, "Orbit-Model Force Coefficients for Fluid Film Bearings: A Step beyond Linearization," *J. Eng. Gas Turbines Power*, vol. 138, no. 2, 2016, doi: 10.1115/1.4031237.

[23] L. San Andrés and A. Delgado, "Identification of force coefficients in a squeeze film damper with a mechanical end seal - Centered circular orbit tests," *J. Tribol.*, vol. 129, no. 3, pp. 660–668, 2007, doi: 10.1115/1.2736708.

[24] F. Y. Zeidan and J. M. Vance, "Cavitation regimes in squeeze film dampers and their effect on the pressure distribution," *Tribol. Trans.*, vol. 33, no. 3, pp. 447–453, 1990, doi: 10.1080/10402009008981975.

[25] S. E. Diaz and L. A. San Andrés, "Air entrainment vs. lubricant vaporization in Squeeze film dampers: An experimental assessment of their fundamental differences," in *Proceedings of the ASME Turbo Expo*, 1999, vol. 4, doi: 10.1115/99-GT-187.

[26] S. E. Diaz and L. A. Andres, "Reduction of the dynamic load capacity in a squeeze film damper operating with a bubbly lubricants," *J. Eng. Gas Turbines Power*, vol. 121, no. 4, pp. 703–709, 1999, doi: 10.1115/1.2818530.

[27] L. San Andrés and S. E. Diaz, "Flow visualization and forces from a squeeze film damper operating with natural air entrainment," *J. Tribol.*, vol. 125, no. 2, pp. 325–333, 2003, doi: 10.1115/1.1510878.

[28] G. L. Arauz and L. San Andres, "Effect of a circumferential feeding groove on

the dynamic force response of a short squeeze film damper," *J. Tribol.*, vol. 116, no. 2, pp. 369–377, 1994, doi: 10.1115/1.2927237.

[29] S. E. Diaz, "An engineering model for prediction of forces in SFD's and experimental validation for operation with entrainment," Texas A&M University, 1999.

[30] S. Diaz and L. San Andrés, "A model for squeeze film dampers operating with air entrainment and validation with experiments," *J. Tribol.*, vol. 123, no. 1, pp. 125–133, 2001, doi: 10.1115/1.1330742.

[31] T. H. Méndez, J. E. Torres, M. A. Ciaccia, and S. E. Díaz, "On the numerical prediction of finite length squeeze film dampers performance with free air entrainment," *J. Eng. Gas Turbines Power*, vol. 132, no. 1, 2010, doi: 10.1115/1.2981182.

[32] L. Tao, S. Diaz, L. San Andrés, and K. R. Rajagopal, "Analysis of squeeze film dampers operating with bubbly lubricants," *J. Tribol.*, vol. 122, no. 1, pp. 205–210, 2000, doi: 10.1115/1.555344.

[33] J. Gehannin, M. Arghir, and O. Bonneau, "Evaluation of Rayleigh-Plesset equation based cavitation models for squeeze film dampers," *J. Tribol.*, vol. 131, no. 2, pp. 1–4, 2009, doi: 10.1115/1.3063819.

[34] J. Gehannin, M. Arghir, and O. Bonneau, "Complete squeeze-film damper analysis based on the 'Bulk Flow' equations," *Tribol. Trans.*, vol. 53, no. 1, pp. 84–96, 2010, doi: 10.1080/10402000903226382.

[35] J. Gehannin, M. Arghir, and O. Bonneau, "A Volume of Fluid Method for Air Ingestion in Squeeze Film Dampers," *Tribol. Trans.*, vol. 59, no. 2, pp. 208–218, 2016, doi: 10.1080/10402004.2015.1023409.

[36] S. Hamzehlouia and K. Behdinan, "Thermohydrodynamic Modeling of Squeeze Film Dampers in High-Speed Turbomachinery," *SAE Int. J. Fuels Lubr.*, vol. 11, no. 1, 2018, doi: 10.4271/04-11-01-0006.

[37] C. Xing, M. J. Braun, and H. Li, "A three-dimensional navier-stokes-based numerical model for squeeze-film dampers. Part 1-effects of gaseous cavitation on pressure distribution and damping coefficients without consideration of inertia," *Tribol. Trans.*, vol. 52, no. 5, pp. 680–694, 2009, doi: 10.1080/10402000902913303.

[38] H.-L. Zhou, X. Chen, Y.-Q. Zhang, Y.-T. Ai, and D. Sun, "An analysis on the influence of air ingestion on vibration damping properties of squeeze film dampers," *Tribol. Int.*, vol. 145, 2020, doi: 10.1016/j.triboint.2020.106168.

[39] G. J. Lee, J. Kim, and T. Steen, "Application of Computational Fluid Dynamics Simulation to Squeeze Film Damper Analysis," *J. Eng. Gas Turbines Power*, vol. 139, no. 10, 2017, doi: 10.1115/1.4036511.

[40] A. Almqvist, "A pivoting algorithm solving linear complementarity problems." 2020, [Online]. Available: https://www.mathworks.com/matlabcentral/fileexchange/41485-a-pivoting-algorithm-solving-linear-complementarity-problems.

[41] H. Gholizadeh, R. Burton, and G. Schoenau, "Fluid bulk modulus: A literature

survey," *Int. J. Fluid Power*, vol. 12, no. 3, pp. 5–15, 2011, doi: 10.1080/14399776.2011.10781033.

[42] R. A. Marmol and J. M. Vance, "Squeeze film damper characteristics for gas turbine engines," *J. Mech. Des. Trans. ASME*, vol. 100, no. 1, pp. 139–146, 1978, doi: 10.1115/1.3453878.

[43] J. W. Lund, A. J. Smalley, A. J. Tecza, and J. F. Walton, "Squeeze-film damper technology: part 1 - prediction of finite length damper performance.," 1983, doi: 10.1115/83-gt-247.

[44] S. M. Rohde and H. A. Ezzat, "ON THE DYNAMIC BEHAVIOR OF HYBRID JOURNAL BEARINGS.," *J Lubr Technol Trans ASME*, vol. 98 Ser F, no. 1, pp. 90–94, 1976, doi: 10.1115/1.3452788.

[45] K.-J. Kim and C.-W. Lee, "Dynamic characteristics of sealed squeeze film damper with a central feeding groove," *J. Tribol.*, vol. 127, no. 1, pp. 103–111, 2005, doi: 10.1115/1.1828075.

[46] L. S. Andres, B. Koo, and S.-H. Jeung, "Experimental Force Coefficients for Two Sealed Ends Squeeze Film Dampers (Piston Rings and O-Rings): An Assessment of Their Similarities and Differences," *J. Eng. Gas Turbines Power*, vol. 141, no. 2, 2019, doi: 10.1115/1.4040902.

[47] C. Xing, M. J. Braun, and H. Li, "A three-dimensional Navier-Stokes-based numerical model for squeeze film dampers. Part 2-effects of gaseous cavitation on the behavior of the squeeze film damper," *Tribol. Trans.*, vol. 52, no. 5, pp. 695–705, 2009, doi: 10.1080/10402000902913311.

[48] L. A. San Andres, "LIQUID CAVITATION IN FLUID FILM BEARINGS," in *Modern Lubrication*, 2009.

[49] S. Seshaghiri, "Identification of Force Coefficients in Two Squeeze Film Dampers with a Central Groove," Teas A&M University, 2011.

[50] P. Mahaecha, "Experimental ynamic Forced Performance of a Centrally Grooved, End Sealed Squeeze Film Damper," Texas A&M University, 2011.